CONVERSION OF 3-D NANOSTRUCTURED BIOSILICA TEMPLATES INTO NON-OXIDE REPLICAS

A Dissertation
Presented to
The Academic Faculty

by

Zhihao Bao

In Partial Fulfillment
of the Requirements for the Degree
Doctor of Philosophy in the
School of Materials Science & Engineering

Georgia Institute of Technology
April 2008

CONVERSION OF 3-D NANOSTRUCTURED BIOSILICA TEMPLATES INTO NON-OXIDE MATERIALS

Approved by:

Dr. Kenneth H. Sandhage, Advisor
School of Materials Science & Engineering
Georgia Institute of Technology

Dr. Meilin Liu
School of Materials Science & Engineering
Georgia Institute of Technology

Dr. Christopher J. Summers
School of Materials Science & Engineering
Georgia Institute of Technology

Dr. Angus P. Wilkinson
School of Chemistry & Biochemistry
Georgia Institute of Technology

Dr. Robert F. Speyer
School of Materials Science & Engineering
Georgia Institute of Technology

Date Approved: Jan. 03, 2008

ACKNOWLEDGEMENTS

I would like to express my thanks to my advisor, Professor Kenneth H. Sandhage for his guidance. His patience, hard work and knowledge set an example for me and will continue to influence the rest of my life. I also would like to thank my committee members, Professor Robert F. Speyer, Professor Meilin Liu, Professor Christopher J. Summers and Professor Angus P. Wilkinson for their valuable suggestions and discussion. Many thanks also to my previous and current research group members including Dr. Yunnan Fang, Dr. Gul Ahmad, Dr. Matthew B. Dickerson, Dr. Benjamin C. Church, Dr. Yunsu Zhang, Dr. Ye Cai, Dr. Yajun Liu, Michael R. Weatherspoon, Samuel Shian, Phillip D. Graham, Shawn M. Allen and David W. Lipke. They were always there when I needed help. Thanks also to Dr. Zhitao Kang and Harry W. Abernathy III. Without their joint efforts, some important publications involved in this thesis work wouldn't have been possible.

I would like to express my thanks to Dr. Runrun Duan for his earnest friendship. My deepest thanks also go to my family for their support and encouragement.

TABLE OF CONTENTS

LIST OF TABLES

LIST OF FIGURES

SUMMARY

Diatoms possess characteristics such as abundance, diversity, and high reproductivity, which make their nano-structured frustules (diatom frustules) attractive for a wide range of applications. To overcome the limitation of their silica based frustule composition, diatom frustules have been converted into a variety of materials including silicon, silicon carbide, silver, gold, palladium and carbon in the present study. The compositions and the extent of shape preservation of the replicas are examined and evaluated with different characterization methods such as X-ray diffraction, SEM, TEM and FTIR analyses. These replicas still retained the complex 3D structures and nano-scaled features of the starting diatom frustules. Some properties and possible applications of converted materials are explored and the kinetics and thermodynamics related to the successful replications (conversions) are also studied and discussed:

(1) A low temperature (650 ºC) magnesiothermic reaction was used to convert three dimensional (3-D) nano-structured diatom frustules into microporous nanocrystalline silicon replicas. These silicon replicas possessed a very high surface area (>500 m^2/g) and a large population of micropores (≤2 nm). The oxidized silicon frustule replicas exhibited photoluminescence under UV light. A microsensor fabricated from such a silicon frustule replica exhibited rapid (≤25 s) and sensitive nitric oxide gas detection (1 p.p.m.) with very low applied biased voltage (100 mV). This suggested a possible application in microscale gas sensing. The magnesium vapor partial pressure was the key parameter in controlling the products from the magnesiothermic reaction. Magnesium silicide

is suggested as the source of magnesium gas to avoid the formation of a magnesium silicide product during the magnesiothermic reaction.

(2) Metallic frustule replicas (*e.g.*, Ag, Au, Pd) were obtained by immersing the microporous nanocrystalline silicon replicas in electroless plating solutions. Silicon carbide frustule replicas were synthesized with two steps. In the first step, the silicon frustule replicas were coated with carbon, either by resin coating or by pyrolysis of methane at 950 ºC. The coated carbon reacted with the silicon at 1200 ºC to form the silicon carbide frustule replicas.

(3) A chlorine reaction process was used to convert the silicon carbide frustule replicas into carbon frustule replicas. This process also introduced micropores into the frustule replicas and, thus, the carbon frustules replicas possessed pores with sizes in various scales, which is important for catalysis. The carbon frustule replicas possessed high surface areas (*e.g.,* 1368 m^2/g) and micropore volumes (*e.g.,* 0.386 cm^3/g). Using a gas deposition method, Pt nanoparticles were successfully loaded into the nanopores of carbon frutule replicas, for possible catalytic application of carbon frustule replicas. The kinetics of the chlorine reaction process were also studied. Because the thickness of the formed carbon layer changed linearly with the reaction time but not the location, the rate-limiting step for the chlorine reaction process was found to be the reaction at the interface between the product carbon layer and the unreacted silicon carbide layer. The minimum time required for complete silicon removal from a silicon carbide frustule replica was also estimated, on the basis of the kinetic data from planar silicon carbide specimens.

Considering the frustule diversity of extant diatom species and ongoing research to develop genetically-modified diatom frustules, diatoms (frustules) with precisely-controlled structures may be fabricated or cultured in the not-too-distant future. These structures may be converted into desired non-oxide compositions for specific applications through the synthetic chemical methods demonstrated in this dissertation. The control over 3-D microscale shape, nanoscale features, and chemistry afforded by such a process combining biology and synthetic chemistry should open the door to a wide variety of low-cost, high-performance electronic, optical, and chemical devices.

CHAPTER 1: INTRODUCTION

1.1 Diatoms

Nature provides spectacular examples of microscopic structures with complex 3D shapes. These structures are not only intricate but also functional. For example, the labyrinthian calcitic skeleton of a brittlestar includes a regular array of microlenses, which are designed to minimize spherical aberration and to focus light onto a nerve bundle[1]. Multicolored butterfly wing scales posses photonic crystal structures[2]. The nacre of abalone shells possesses a laminated structure comprised of organic (<10 nm) and inorganic (<0.5 μm) phases with impressive mechanical properties[3]. These structures are the result of hundreds of thousands of years or more of evolution, and may be superior to many synthetic designs. Among these natural biogenic structure-forming organisms, diatoms are particularly attractive because of their abundance, diverse morphologies, and high growth rates. Diatoms are microscopic, single-celled algae that possess rigid cell walls (frustules) composed of amorphous silica. They are found in abundance in a wide variety of aquatic environments (*e.g.*, arctic and equatorial; marine and freshwater). For example, diatoms are estimated to contribute up to 45% of the total oceanic primary biomass production[4]. There are currently estimated to be over 100,000 different diatom species[5, 6]. Depending on the diatom species and the culturing conditions (*e.g.*, salinity[7]), these frustules can display a wide range of different morphologies. A collection of SEM images of diatom frustules, which demonstrates the diversity of diatom frustule morphologies, is shown in Fig.1.1. The maximum dimensions of such frustules can range from less than 1 μm to larger than 100 μm, whereas the regular features on the frustule wall possess dimensions of tens to hundreds of nm[5, 6]. Because of the diversity of

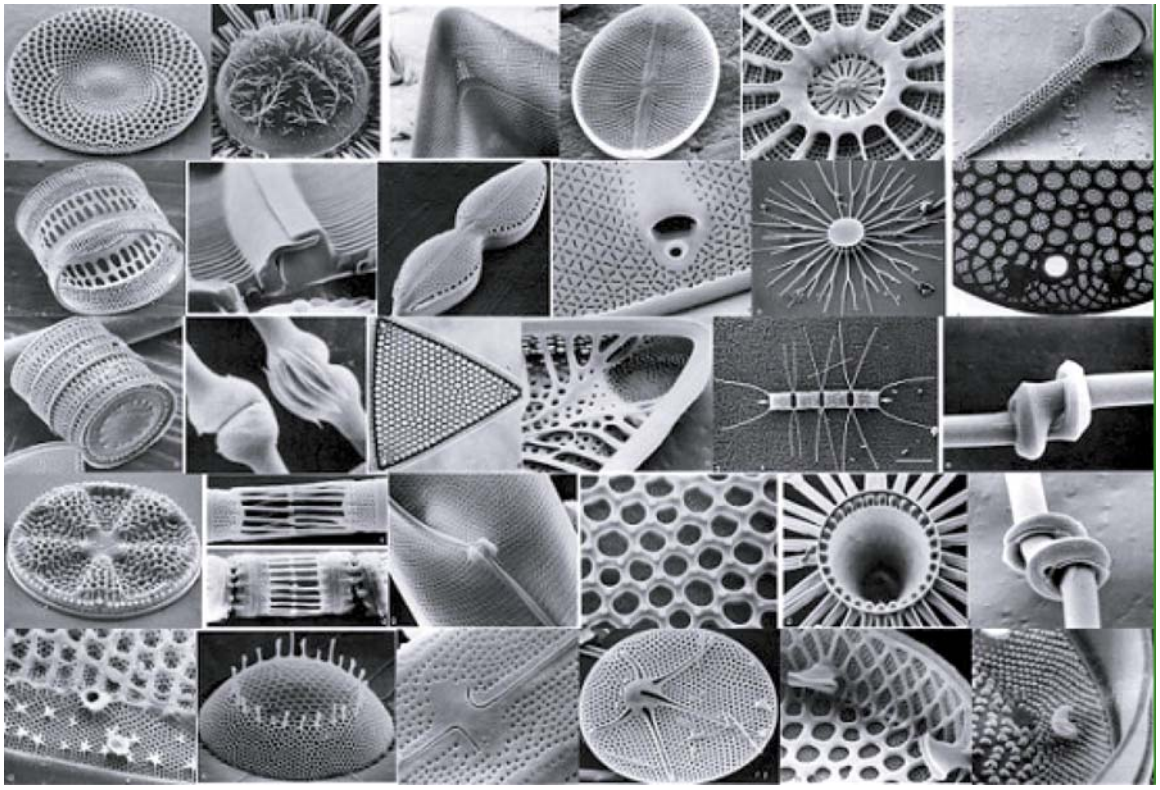

Figure 1.1: Secondary electron images of silica frustules of various diatom species. (F. E. Round *et. al.*, *The Diatoms: biology & morphology of the genera,* Cambridge University Press, 1990)

morphologies of diatom frustules, it is possible to find specific frustules with structures attractive for potential applications in nanotechnology[8]. Once specific diatom species are identified for a given application, they can be cultured on a large scale. Under the same growth conditions, for a given species, the descendant diatoms possess frustules that are precise reproductions of the shape of the parent diatom frustule[6, 9]. Diatom reproduction can occur as often as eight times per day[9], so that enormous numbers of descendant diatoms with similar shapes can be generated in a relatively short period of time. For example, with sustained culturing, a single pilot-scale facility with 45 vertical bubble column photobioreactors can generate over 700 kg (dry weight) of diatom biomass per year[10].

Diatom frustules are used for a range of applications, including filtration, absorbents, fillers, insulation, and cement manufacture[11]. However, research on advanced applications of diatom frustules in fields such as nanotechnology and optics is still underway. For example, diatom frustules can be used as templates for gold nanoparticles and as masks for lithography[12, 13]. Some diatom frustules even have attractive optical properties due to their highly symmetric structure. For example, frustules of *Coscinodiscus wailesii* are natural 2D micro photonic crystals with a pseudo-band gap[14]. Fig.1.2 shows a top view of a *Coscinodiscus wailesii* frustule (provided by Dr. Gul Ahmad), which possesses pores with 6-fold symmetry. Finite element analyses (FEA) indicate that the replacement of silica (n=1.4) in the *Coscinodiscus wailesii* frsutule with titanium oxide (n=2.4) would yield a complete 2-D band gap[14]. This example also demonstrated a disadvantage of silica (modest optical index of refraction) as the composition of diatom frustules. Indeed, siliceous diatom frustules are not suitable for

many device applications[8]. Though germanium oxide can also be incorporated at a low concentration into the siliceous structure of diatoms by including a source of germanium in the culturing media, its trace amount of incorporation cannot appreciably change the range of properties exhibited by diatom frustules[15].

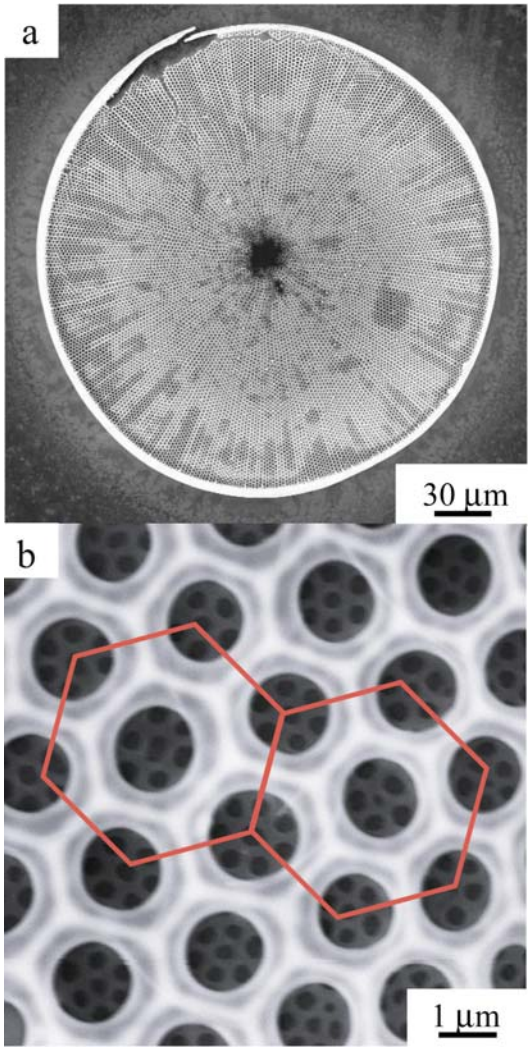

Figure 1.2: a, Low magnification secondary electron image (SE) of a *Coscinodiscus wailesii* frustule (Top view). B, High-magnification SE image of the frustule, revealing a pore structure with hexagonal symmetry. (The sample was prepared by Dr. Gul Ahmad.)

1.2 BaSIC process

To overcome the chemical limitation of diatom frustules and, at the same time retain the useful shapes of diatom frustules, a novel process called **BaSIC (Bioclastic and Shape-preserving Inorganic Conversion)** has recently been developed to convert biosilica micropreforms into new ceramic compositions with retention of shapes and fine features[16]. For example, Mg vapor generated at 950 °C was reacted with diatom frustules to form MgO-bearing structures with identical morphology as that of the starting diatom frustues[17]. And gaseous halides (*e.g.,* TiF_4 and $ZrCl_4$) were used to convert diatom frustules into TiO_2 and ZrO_2 frustule replicas[18,19]. A variety of materials synthesized and synthetic chemical methods used, in the BaSIC process are summarized in Table 1.1[17, 19-24]. Compared to traditional micromachining methods based on 2D, layer-by-layer techniques (*e.g.,* photolithography, chemical etching, and ion-beam etching)[25], the BaSIC method is a direct 3-D microfabrication process. More importantly, because of abundance, diversity, and high throughput of biosilica micropreforms, the BaSIC process may open the door to a wide variety of low-cost, high performance optical, electronic, and chemical devices. In addition to the biosilica micropreforms from nature, there are many types of synthetic silica-based templates such as SBA-15, opals, and woodpile structures[26-28]. The shape preservation and synthetic chemical methods used in BaSIC may also be applicable to these templates. As summarized in Table 1.1, the previous successfully-synthesized materials were all oxides. Because of the obvious differences in the properties (*e. g.*, thermal, electronic, and chemical properties) between oxides and non-oxides, it is worthwhile to investigate the syntheses of non-oxide materials with specific 3-D shapes.

Table 1.1: Methods used and materials synthesized in BaSIC process[17, 19-24].

Method	Material
Gas displacement reaction	MgO, TiO_2
Conformal coating	Polymer, ZrO_2, $BaTiO_3$
Combination of metathetic reaction and hydrothermal reaction	$BaTiO_3$, $SrTiO_3$
Combination of conformal coating and Solid-state chemical reaction	Zn_2SiO_4

Recent research in this thesis has demonstrated that the BaSIC process can be used to generate non-oxide diatom frustule replicas (*e.g.,* Si, SiC, and C). 3-D assemblies comprised of Si, SiC, or C have a wide variety of potential applications in optoelectronics, displays, photovoltaics, gas sensors, bone implants, reinforcing materials and catalyst supports[29-32]. In this dissertation, the kinetics and thermodynamics related to the conversion of silica-based diatom frustules into different non-oxide replicas were studied and discussed. The properties and possible applications of some converted materials were also evaluated.

CHAPTER 2: POROUS SILICON CONVERSION

To obtain silicon from silica, the carbothermal process requires the use of temperatures well above the silicon melting point (≥2000°C)[33]. Because liquid silicon and gaseous silicon monoxide are present in this high temperature process, it is impossible to maintain the shapes of starting solid silica reactants. Though electrochemical reduction of silica in molten salts (*e.g.,* $CaCl_2$) can generate solid silicon at a lower temperature (≤850°C), the heterogeneous growth of silicon grains during such electrochemical reduction makes it impossible to retain the microscale morphology of the starting silica reactants[34-36]. Magnesium gas has been used to reduce silica into silicon at a much lower temperature (~600 °C), however, the retention of the 3-D shapes of the starting silica reactants had not been reported[37].

Porous silicon can possess a structure with a large surface to volume ratio[38, 39]. There are usually two common methods to fabricate porous silicon from a silicon wafer. One is anodisation, in which a silicon wafer is anodically oxidized under a constant current in an aqueous or ethanolic solution with high concentration of HF[38, 39]. The other intrinsically easier, though less frequently-employed approach is stain etching, in which a silicon wafer was etched with a mixture of HF, nitric acid and water[40]. Porous silicon can possess attractive electronic, optic, biological properties for a wide range of applications[30, 31, 41-43]. For example, porous silicon can be used as the negative electrode for rechargeable lithium batteries[42]. It is used as a stable platform for reversible and inexpensive detection of several gases such as CO, NO_x, SO_2 and NH_3[31, 41]. Hydroxyapatite can form on porous silicon, implying the possible bone implantibility of the material[30]. Porous silicon may also find application as an optical waveguide[43]. During

the fabrication of porous silicon, high quality silicon wafers and high concentration HF solutions were used in both the anodization etching and the stain etching processes. These two processes are not particularly environmentally friendly. It also proved to be difficult to produce free-standing 3-D porous silicon micro-structures through the anodization etching process[44]. A low temperature (650 °C) magnesiothermic reduction process for converting three-dimensional nanostructured bio-silica micro-assemblies into microporous nanocrystalline silicon replicas is demonstrated in this thesis.

2.1 Experimental design and methods

A secondary electron image of an *Aulacoseira* diatom frustule is shown in Fig. 2.1. The frustule was lined with rows of fine pores (10^2 nm in diameter) running along the cylinder length, and also contained narrow channels between intercalating fingerlike extensions. *Aulacoseira* diatom frustules were utilized as the reactive templates in most of the experiments. 0.3 grams (0.005 moles) of diatom frustules were spread evenly onto a steel boat (3.5 inches long and 1 inch wide). The boat was sealed in a crimped 6-inch steel tube along with 0.3 grams (0.0125 moles) of Mg granules. The detailed configuration is shown in Fig. 2.2. The tube was then placed in a furnace preheated to 650˚C, and held there for 2.5 hours. After the tube was removed from the furnace and cut open, three regions with different colors were clearly seen in the powder bed. The region located nearest the magnesium gas source was blue in color. A black region and then a brown region were observed with increasing distance from the magnesium gas source. X-ray diffraction (XRD) analyses indicated that each region contained magnesia (magnesium oxide). The black and brown regions also contained silicon as a secondary product phase, whereas the blue region contained magnesium silicide. In the brown region, residual, un-

reacted silica (in the form of cristobalite) was also detected. The powder in the black region was collected and immersed in a 1 M HCl solution (molar $HCl:H_2O:EtOH$ ratio 0.66:4.72:8.88) for 4 hours at room temperature to selectively dissolve the magnesia. The specimens were then immersed in a HF solution (molar $HF:H_2O:EtOH$ ratio 1.05:1.11:6.45) for 20 min to ensure that any oxide formed due to exposure to the aqueous HCl treatment was removed. The HCl immersion, the subsequent HF treatment, and drying were conducted in a glove box filled with purified argon gas, which was supplied from an ultra high-purity tank (99.999% purity) and further purified with an oxygen gettering system. The oxygen partial pressure in this glove box was maintained at below 0.1 p.p.m. and monitored by an oxygen sensor.

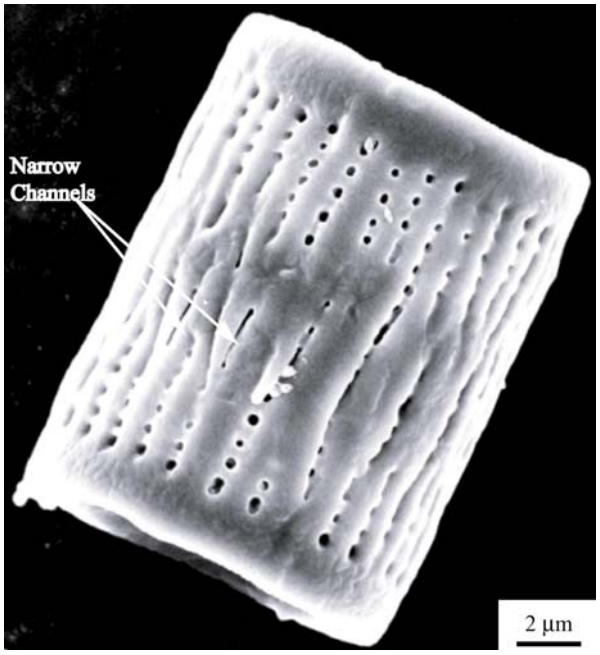

Figure 2.1: Secondary electron image of an *Aulacoseira* diatom frustule.

.

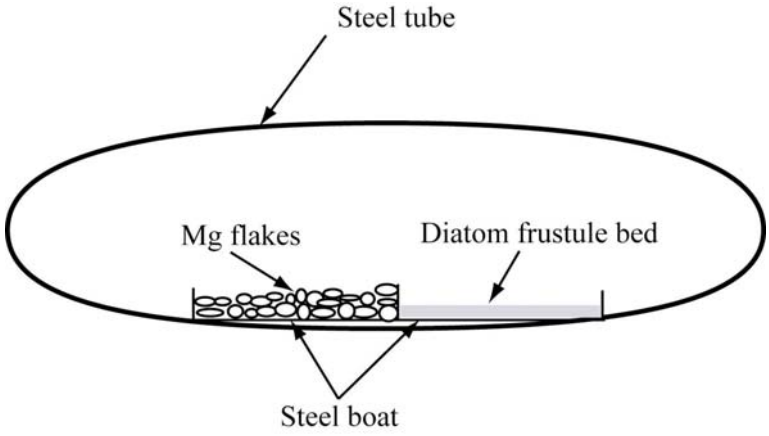

Figure 2.2: Configuration for a magnesiothermic reaction.

2.2 Characterization

2.2.1 X-ray diffraction (XRD), SEM and TEM characterization

The XRD patterns of the powder samples from three regions with different colors are shown in Fig. 2.3a-c. The blue, black, and brown regions of the reaction products were comprised largely of magnesia and magnesium silicide, magnesia and silicon, and silicon, magnesium and silica, respectively. In the black region, silica diatom frustules were converted into MgO/Si-bearing replicas by the following magnesiothermic reaction:

$$2Mg(g)+SiO_2(s)\rightarrow 2MgO(s)+Si(s) \quad (2.1)$$

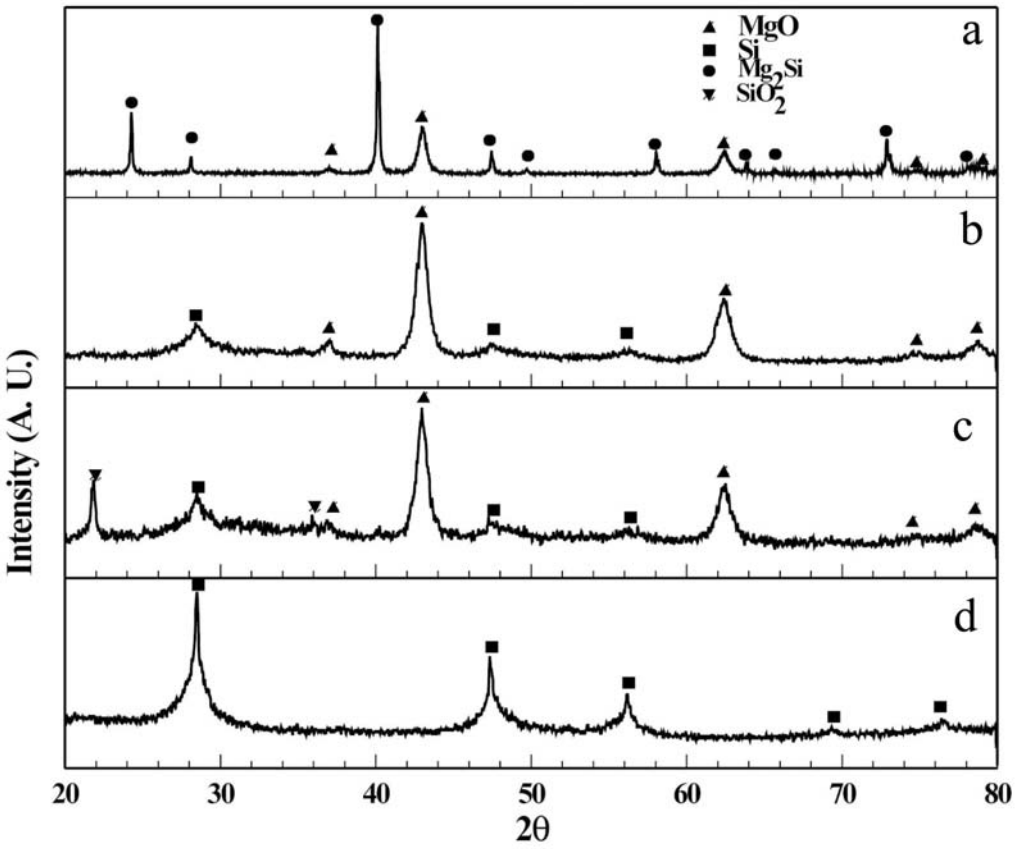

Figure 2.3: X-ray diffraction (XRD) patterns of *Aulacoseira* diatom frustules, after exposure to magnesium gas at 650 ºC for 2.5 hrs, obtained from the (a) blue region, (b) black region, and (c) brown region of the reaction products. (d) X-ray diffraction pattern of powder in the black region after immersion in a 1 M HCl solution for 4 hours.

The secondary electron (SE) image of the MgO/Si composite (Fig. 2.4a) generated by chemical reaction (2.1) retained the three-dimensional (3D) cylindrical morphology and nanoscale features (rows of fine pores, narrow channels) of the *Aulacoseira* frustule. The reacted specimen was composed of silicon and magnesia, according to XRD analysis shown in Fig. 2.3b. The MgO/Si composite replicas were then immersed in a 1M HCl solution for 4 hour. XRD (Fig. 2.3d) and energy dispersive X-ray (Fig. 2.4d) analyses of the specimen after the immersion indicated that this treatment completely removed the magnesia in the composite. The resulting silicon-based product, as shown in Fig. 2.4b, retained the 3D morphology and nanoscale features of the *Aulacoseira* frustule. Though XRD analysis indicated the existence of only a crystallized silicon phase, the energy dispersive X-ray pattern in Fig. 2.4d contained a modest oxygen peak. Such an oxygen peak was associated with amorphous silicon oxide formed when the silicon was exposed to the water-rich hydrochloric solution. The replicas were then immersed in an ethanol-based hydrofluoric acid (HF) solution for 20 min. The absence of an oxygen peak in the energy dispersive X-ray pattern in Fig. 2.4e indicated that the amorphous silicon oxide had been completely and selectively dissolved by this HF treatment. Transmission electron images of cross-sections of a silicon frustule replica are shown in Fig. 2.5 (provided by Dr. Ye Cai). Though some of the silicon crystals located in the outer surfaces of the silicon replicas were relatively large (~30 nm; Fig. 2.5b), the silicon crystals present within the wall of the converted frustules were much finer. Scherrer analysis of the XRD pattern in Fig. 2.3d yielded an average silicon crystallite size of 13±2 nm. A corresponding selected area electron diffraction pattern is shown in Fig. 2.5e.

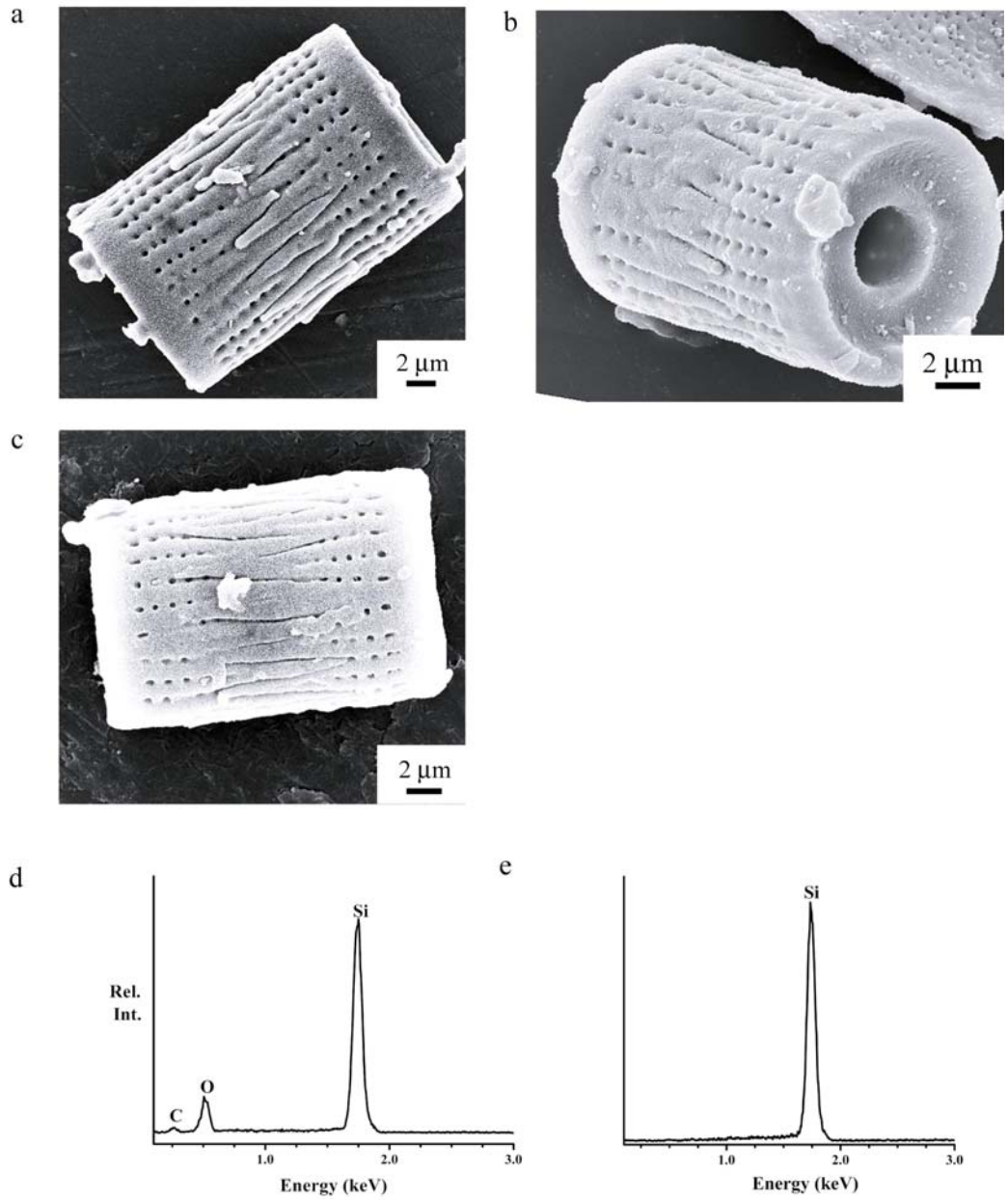

Figure 2.4: a, Secondary electron image of a MgO/Si composite replica after reaction of an *Aulacoseira* frustule with Mg(g) at 650 °C for 2.5 h. b, Secondary electron image of a silicon-bearing replica produced by selective dissolution of magnesia from a MgO/Si replica in an HCl solution. c, Secondary electron image of a silicon replica after the HCl treatment and an additional treatment in a HF solution. d, e, Energy dispersive X-ray analyses obtained from silicon frustule replicas of the type shown in b and c, respectively. (Published in *Nature*, 446, 172- 174, 2007.)

Consistent with XRD and EDS analyses, electron diffraction analysis indicated the presence of silicon as the only crystalline phase throughout the replica cross section. The high-resolution transmission electron image, shown in Fig. 2.5c, and the associated Fourier-filtered version of this image, shown in Fig. 2.5d, both revealed lattice fringe images of adjacent silicon nanocrystals. The continuation of the lattice fringe patterns from these adjacent grains up to the grain boundary indicated that this grain boundary was free of any amorphous phase. Grain boundaries between other adjacent silicon nanocrystals were also found to be free of any amorphous phase. These results proved that the porous silicon frustule replicas consisted of interconnected silicon. Weatherspoon *et. al*[45], used a sodium hydroxide aqueous solution to selectively dissolved the silicon component in a MgO/Si composite frustule replica and obtained a freestanding magnesia frustule replica, which also preserved the starting frustule morphology. Therefore a MgO/Si frustule replica should consist of co-continuous, interpenetrating silicon and magnesia phases. This intertwined structure inhibited the coarsening of both phases, owing to reduced mass transport within the same phase due to less grain-to-grain contact area for each phase. The mild 650 ^{o}C heat treatment also suppressed the formation of the volatile gas species (*e.g.,* Si(g) and SiO(g)). These two factors made it possible to preserve the fine features in porous silicon frustule replicas after selective removal of magnesia. The secondary electron images of *Melosira Nummuloides* diatom frustules (provided by Dr. Gul Ahmad) before and after the magnesiothermic reaction and subsequent immersion in HCl solution are attached in Appendix A. Features as fine as tens of nanometers in size in the starting diatom frustules were well preserved in the silicon frustule replicas.

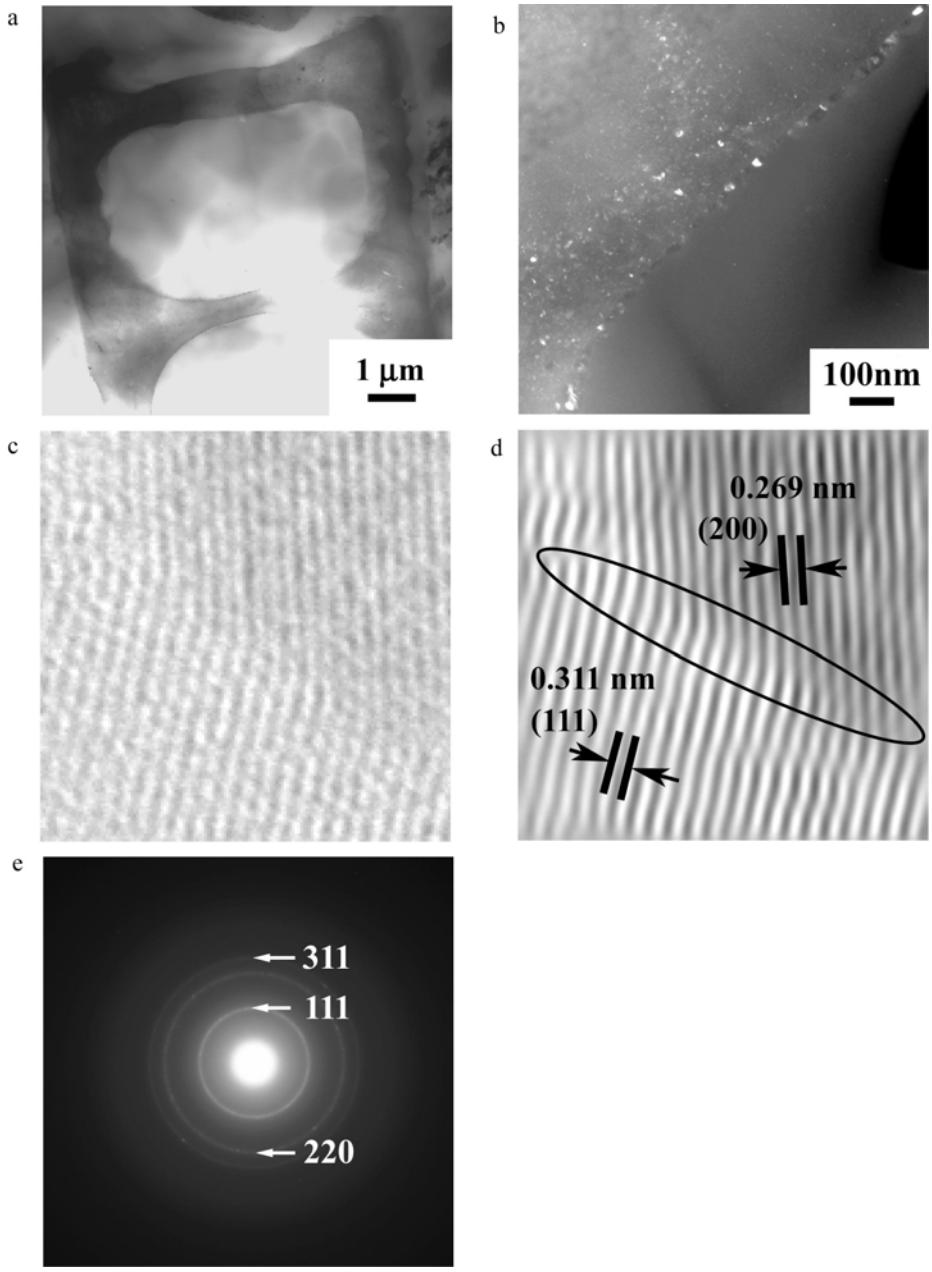

Figure 2.5: a and b, Low magnification bright field and higher-magnification dark field transmission electron images, respectively, of an ion-milled cross-section from a silicon frustule replica. c, High-resolution transmission electron image of adjacent silicon nanocrystals. d, The same image in c after Fourier filtering. e. Selected area electron pattern obtained from the silicon frustule replica. (Provided by Dr. Ye Cai and published in *Nature*, 446, 172- 174, 2007.)

2.2.2 XPS characterization

To confirm that the entire replicas were composed of only silicon after immersion in HCl and HF solutions, X-ray photoelectron spectroscopic (XPS) analysis was conducted. XPS spectra were obtained with a Kratos Axis-165 instrument (Kratos Analytical, Manchester, UK) using monochromatic Al Kα radiation. After HCl immersion and HF washing, the resulting silicon frustule replicas were allowed to dry in an argon-filled glove box. The dried frustule replicas were then pressed onto a 0.25-mm-thick indium foil (99.99% purity) and sealed in plastic bags in the glove box. The indium foil was used to eliminate the influence of charge build-up. The specimens were transferred into the XPS instrument under an argon atmosphere. The sealed bags were then placed inside a glove bag that was sealed around the evacuable antechamber of the XPS. After the glove bag was purged with ultrahigh-purity (99.999%) argon, the specimens were removed from the plastic bags and placed inside the antechamber. The antechamber was then evacuated for XPS analyses. Milling of the specimens within the XPS system was conducted with Ar ions. XPS analyses were calibrated with respect to the carbon 1s excitation (285.0 eV). The milling rate was estimated to be 1 nm/min, based on experiments with Si wafers. The spectra were collected from an as-synthesized frustule replica, and the replica after 2, 4, 6 and 8 minutes of Ar^+ ion etching. The XPS analyses (provided by Michael Bestor in University of Alabama) are shown in Fig. 2.6. A single peak located around 99.7 eV was detected from the replicas after different milling times. The 99.7 eV peak is associated with Si 2*p* excitation from elemental silicon[46, 47]. The XPS depth profiling and previous energy dispersive X-ray analyses (Fig. 2.4e) both confirmed the presence of only silicon in these frustule replicas.

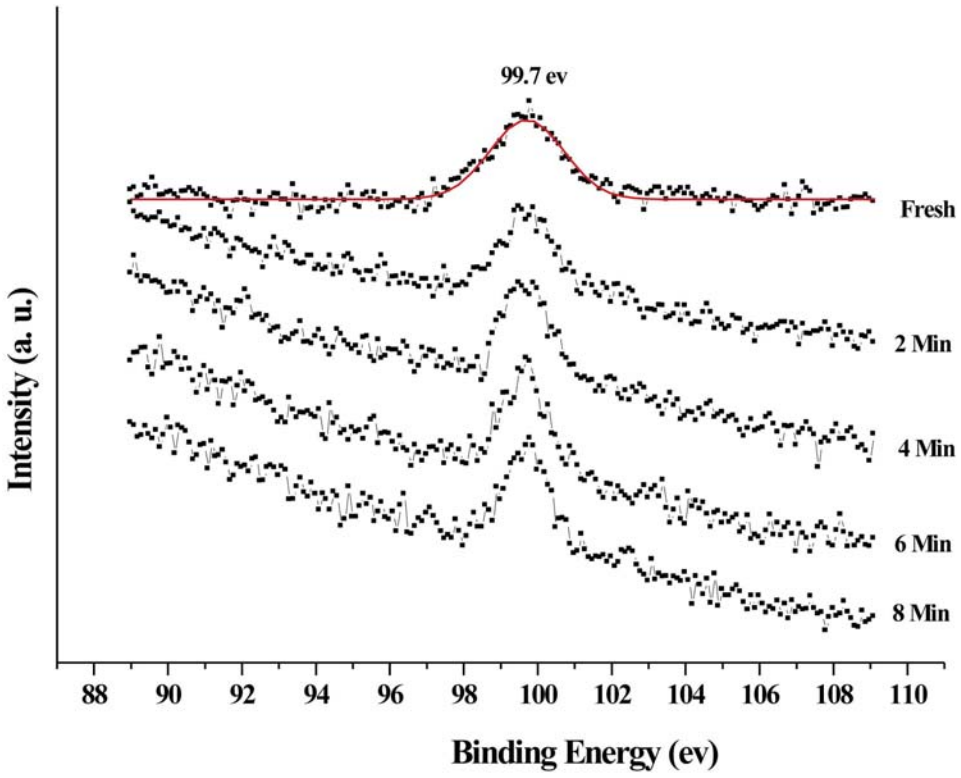

Figure 2.6: X-ray photoelectron spectroscopic (XPS) analyses (Si 2*p* core level spectra) of silicon replicas of *Aulacoseira* frustules (Provided by M. Bestor and published in *Nature*, 446, 172- 174, 2007).

2.2.3 BET and porosity characterization

The surface area and pore size distribution determine much of the adsorptive properties of a material, and therefore is of importance in application areas such as sensing, biofiltration, and energy storage. Table 2.1 reveals characteristic ranges of pore size established by International Union of Pure and Applied Chemistry (IUPAC)[48].

Table 2.1: IUPAC classification of pore size[48]

Pore width (nm)	Type of pore
≤ 2	Micro
2-50	Meso
>50	Macro

The products of magnesiothermic reaction (2.1) consist of one mole of silicon with two moles of magnesia, which corresponds to 34.9 vol.% silicon and 65.1 vol.% magnesia. The interconnection of both phases in the MgO/Si frustule replicas enabled complete dissolution of the magnesia to yield highly porous silicon frustule replicas. To evaluate the surface area and pore volume/sizes of diatom frustules and their corresponding replicas, gas adsorption analyses were conducted by Dr. Benjamin C. Church with an Autoabsorb-1 (Quantachrome, FL, USA), using nitrogen as the adsorbate at 77K. Fig. 2.7a-c reveals the nitrogen isothermal adsorption and desorption curves for the starting silica frustules, MgO/Si composite replicas and porous silicon replicas at 77K, respectively. Fig. 2.7a and Fig. 2.7b are typical type-II curves[49], indicating the absence of mesopores inside the starting silica frustules or the MgO/Si composite

replicas. However, a hysteresis loop appeared in the adsorption and desorption curves for porous silicon frustules replicas, which indicated the presence of mesopores. BET (Brunauer–Emmett–Teller) analyses indicated that the specific surface areas (SSA) of the starting silica frustules and of the MgO/Si composite replicas were only 1.65 m^2/g and 1.56 m^2/g, respectively. After magnesia removal, however, the specific surface area increased to 541 m^2/g. This value is higher than the BET specific surface area (143~364 m^2/g) from the porous silicon samples formed on heavily doped p-type substrates[50, 51]. BJH (Barrett–Joyner–Halenda) analyses of the nitrogen desorption curves (Fig. 2.7d) indicated that, unlike the starting frustules or MgO/Si replicas, the silicon replicas possessed a significant population of micropores; that is, pores ≤2 nm in diameter, comprised 30% of the cumulative volume occupied by all pores ≤125 nm in diameter.

To obtained higher surface area, the starting diatom frustules were exposed to the surfactant, hexadecyltrimethylammonium bromide (CTAB), in a sodium hydroxide-bearing solution to induce dissolution/reprecipitation of the silica. Fowler, *et al.* have used this approach to introduce mesoporous silica into, and thereby increase the surface area, of diatom frustules while retaining shapes[21, 52, 53]. In this treatment, silica-based diatom frustules, sodium hydroxide, CTAB, and water (molar ratio, 1:0.25:0.1:20) were mixed together to form a slurry. This mixture was then sealed in a 50 ml stainless steel container, which was heated to 112 ºC and held at this temperature for 72 hours. The frustules were then filtered from the slurry, washed and dried. The detailed procedure was described elsewhere[21]. After this process, the specific surface area of the silica frustules increased from 1.6 m^2/g to 70~ 120 m^2/g[21]. The BET specific surface area and porosity of porous silicon replicas from CTAB treated diatom frustules were also

examined. Fig 2.8a reveals the N_2 isothermal adsorption/desorption curves and the cumulative pore size distribution of such porous silicon frustule replicas at 77K. BET analysis yielded a specific surface area of 1323 m^2/g. The volumes of micropore and mesopores were also dramatically increased.

These 3-D freestanding silicon frustule replicas with high surface areas may be ideal for the realization of a high performance lithium battery. Silicon can alloy with lithium up to 4.4 Li per Si, allowing for an extremely large theoretical specific capacity of 4200 mAh/g[54, 55]. Porous silicon is an attractive material for lithium battery application because of its relatively high reactivity with lithium at room temperature. However, only part of the available active surface area in the deep-channeled porous silicon has been utilized owing to limited penetration of electrolyte into the structure due to a strong capillary effect[42]. The thin frustule wall thickness (<1 μm for *Aulacoseira* diatoms) and open structures of the silicon frustule replicas would provide easy access for liquid electrolyte and a high surface area for reaction, which could result in lithium ion batteries with high power density and energy density.

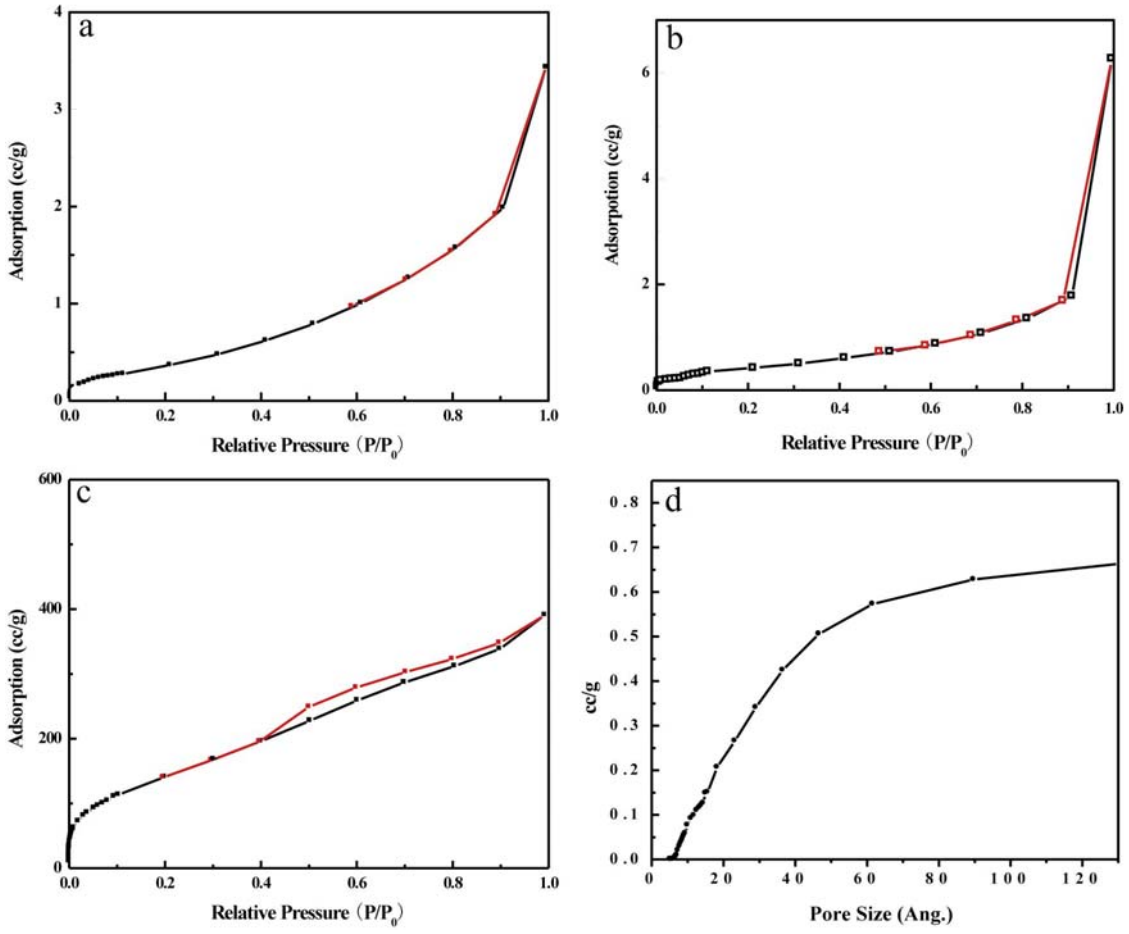

Figure 2.7: BET surface area analyses and BJH cumulative pore size distribution analyses of starting diatom frustules and converted frustule replicas. Nitrogen isothermal adsorsportion/desorption curves of: a) starting frustules, b) MgO/Si composite frustule replicas, and c) porous silicon replicas at 77K. d) Cumulative pore size distribution of porous silicon frustule replicas (black: adsorption curve; red: desorption curve. Data was colleted by Dr. Beniamin C. Church).

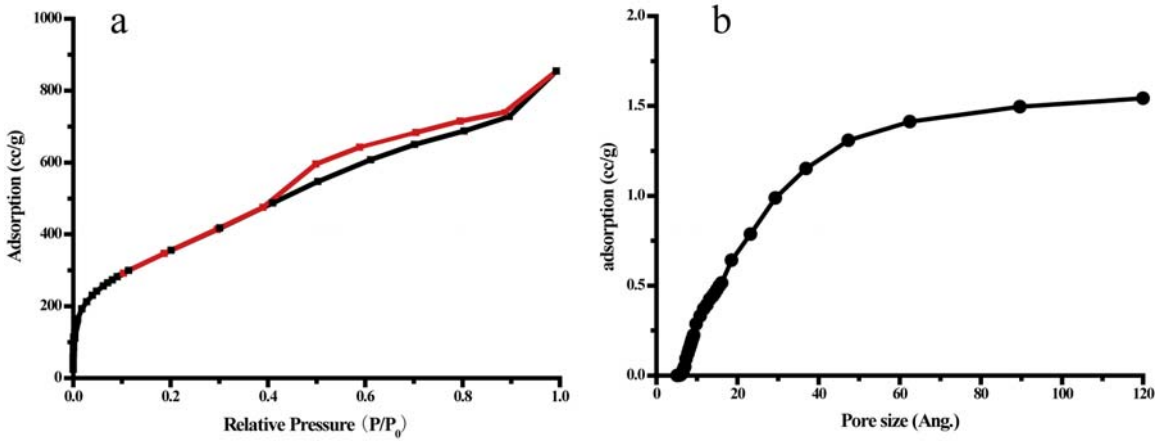

Figure 2.8: a, Nitrogen isothermal adsorption/desorption curves at 77K; b, Cumulative pore size distribution, of silicon frustule replicas obtained by magnesiothermic conversion of CTAB-treated diatom frustules (black: adsorption curve; red: desorption curve).

2.3 Thermodynamics of the magnesiothermic reaction

Extensive magnesium silicide formation occurred during the magnesiothermic reaction. It was necessary to evaluate the thermodynamics of the magnesiothermic reaction in order to understand how to inhibit the formation of magnesium silicide and thereby increase the silicon yield.

When magnesium gas reacts with silica, two consecutive reactions can happen. One reaction results in the liberation of silicon from silica, as shown in the magnesiothermic reaction (2.1). Magnesium gas can also react with the liberated silicon to form Mg_2Si, as shown in reaction (2.2).

$$2Mg(g)+Si(s)\rightarrow Mg_2Si(s) \qquad (2.2)$$

Reaction (2.2) is consistent with the Mg-Si phase diagram (Fig. 2.9), which shows that Mg and Si can react to form the line compound Mg_2Si. In the present experiments, magnesium silicide formed even if the reactant molar ratio was less than the stoichiometric value ($2Mg:1SiO_2$) for reaction (2.1). The rate of magnesium silicide formation was apparently sufficiently fast that this compound could form before reaction (2.1) was completed.

Based on the thermodynamic data[56], curves of the magnesium equilibrium vapor pressure at different temperatures for the reaction (2.1), the reaction (2.2), and for the evaporation of magnesium were calculated and are shown in Fig. 2.10. From 200-1300 ºC, the magnesium vapor pressures from a magnesium source are higher than the equilibrium vapor pressure required for the formation of magnesium silicide. Hence, the formation of magnesium silicide will be difficult to avoid if pure magnesium is used as the magnesium gas source. An illustration of the hypothesized Mg vapor partial pressure versus distance from the Mg source is shown in Fig. 2.11. Near the magnesium source (area III), silicon was displaced from silica first and thereafter converted into Mg_2Si, because the local partial pressure of magnesium vapor was higher than the equilibrium magnesium vapor pressure required for the formation of Mg_2Si. In the middle region of the product zone (area II), the local magnesium vapor pressure apparently dropped to such a level that silicon could be liberated from the silica but magnesium silicide could not form. The far end of the product zone (area I) contained un-reacted silica either because the reaction time was not long enough for the diffusion of Mg vapor to this area at the given temperature, or because the magnesium gas couldn't penetrate the powder bed thoroughly before the magnesium source was totally consumed. Above analysis also

revealed that the diffusion of Mg vapor was one of the rate limiting steps for the Magnesiothermic reaction process. Fig. 2.10 also shows that the equilibrium magnesium vapor pressure generated from magnesium silicide was high enough to drive reaction (2.1) to the right. Hence, it is possible to use magnesium silicide as a magnesium gas source without introducing further magnesium silicide as a byproduct of the magnesiothermic reaction. This concept was first confirmed by Haluska *et. al.,* for the first time[57].

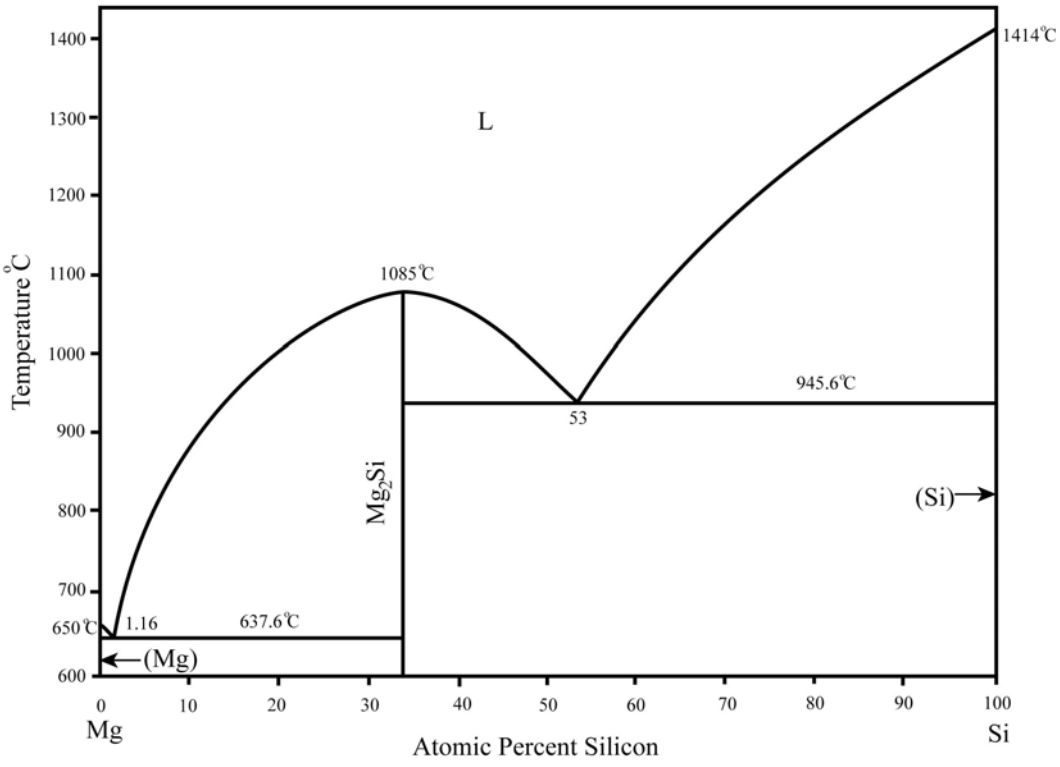

Figure 2.9: Phase diagram of the Mg-Si system[58].

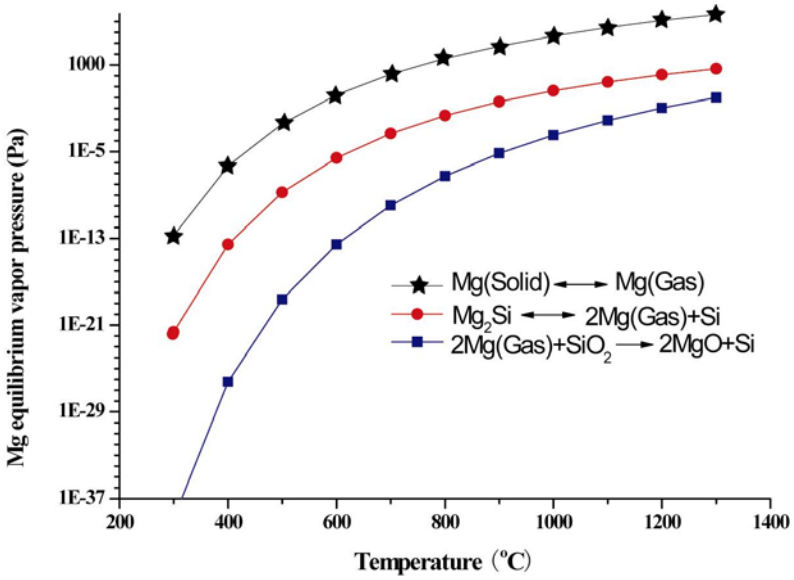

Figure 2.10: Calculated equilibrium magnesium vapor partial pressures associated with reactions (2.1), (2.2), and for magnesium evaporation from condensed (s, l) magnesium.

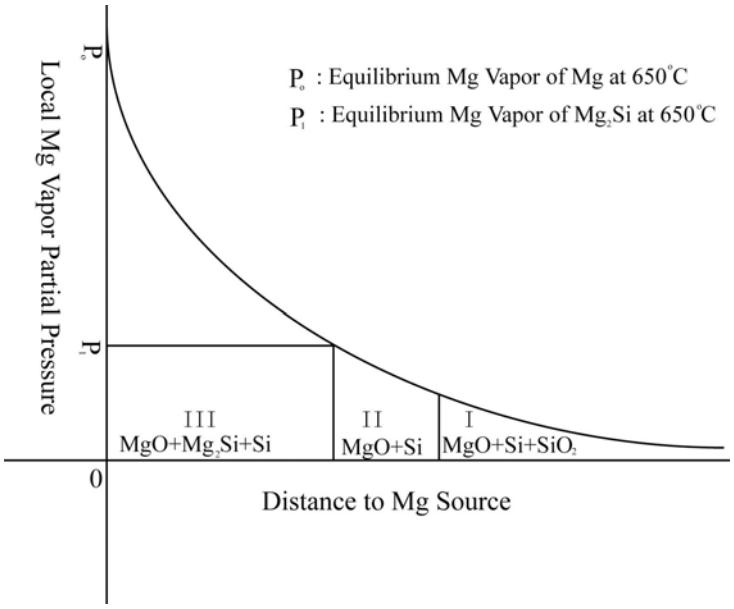

Figure 2.11: Illustration of the apparent spatial distribution of magnesium vapor within the steel ampoules, with the corresponding phase region at a typical moment during the reaction. A mixture of MgO, Si and SiO_2 formed in the region I. A mixture of MgO and Si formed in the region II. A mixture of MgO, Mg_2Si, and Si formed in region III.

2.4 Properties and Applications

2.4.1 Photoluminescence of porous silicon frustule replicas

Photoluminescence (PL) measurements were conducted with a Spex 1000M Spectrometer using an argon laser, with an emission wavelength of 275 nm (ultraviolet) and a power of 5 mW, as the excitation source. The laser was focused to a spot of ~1 mm in diameter on the sample. The measurements were performed at room temperature and recorded with a GaAs photomultiplier tube with a cut-off wavelength of 920 nm. As synthesized porous silicon frustules replicas did not exhibit obvious photoluminescence. A modified protocol was used to further reduce the average size of the crystals in the silicon replicas. The MgO/Si composite replicas were immersed in an aqueous solution of 1.1 M hydrogen peroxide (H_2O_2) and 2.2 M ammonium hydroxide (NH_4OH) at 70 °C for 0.5 h, in order to partially oxidize the silicon grains (particularly the relatively coarse grains on the external replica surfaces). The MgO component was retained during this treatment so as to prevent the inner, relatively fine Si grains from being oxidized. The oxidized composite was then immersed in HCl and HF solutions to selectively dissolve the magnesia and silica formed by this additional process, respectively. Fig. 2.12 reveals the X-ray diffraction patterns for the as-synthesized silicon frustule replicas (red line) and the silicon frustule replicas treated with the H_2O_2/NH_4OH protocol (black line), respectively. According to Scherrer analysis of this XRD data, the average grain sizes were 13±2 nm and 8±1 nm, respectively, which was consistent with the removal of large silicon grains on the external surface of the porous silicon frustule replicas by the H_2O_2/NH_4OH treatment. However, the silicon frustule replicas still did not exhibit

photoluminescence. Several authors have reported the photoluminescence of microporous silicon in ultraviolet light, particularly after partial oxidation in water[59, 60].

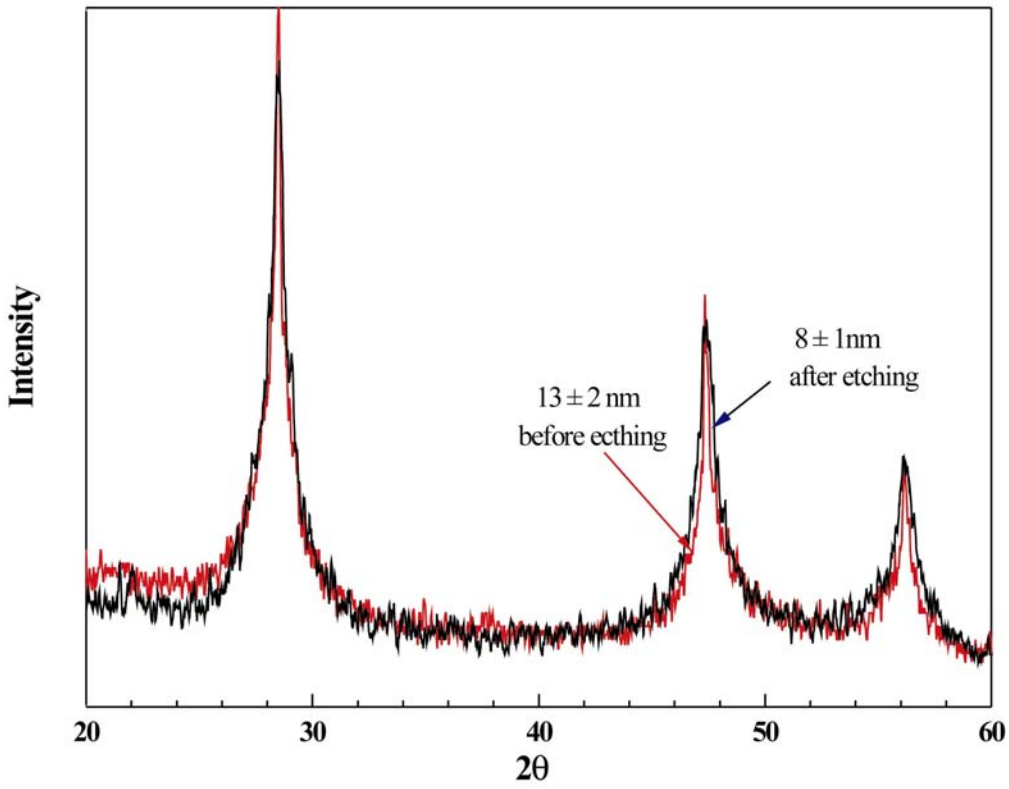

Figure: 2.12 X-ray diffraction patterns obtained from starting silicon frustule replicas (red line) and replicas treated with an additional H_2O_2/NH_4OH protocol (black line).

To evaluate such oxidation-induced photoluminescence, the silicon frustule replicas were partially oxidized by immersion in water at room temperature for 40 days. The photoluminescence of the 3-D silicon frustule replicas was dramatically enhanced after such partial oxidation (Fig. 2.13a, by Dr. Zhitao Kang). A Zeiss Axiovert 200 microscope with a fluorescence excitation of 450-490 nm was used to obtain a fluorescence image of photoluminescent silicon frustule replicas, which is shown in Fig. 2.14 (by Dr. Matthew B. Dickson).

Fourier transform infrared (FTIR) spectroscopic analyses were recorded using a Bruker Equinox 55 spectrometer with a liquid N_2-cooled MCT detector, to examine the surface oxidation of silicon frustules replicas after water immersion. The measurements were made in diffuse reflectance mode using a Praying Mantis DRIFTS attachment from Harrick Scientific. Both the spectrometer and DRIFTS attachment were continuously purged with N_2 gas to minimize the background signal from CO_2 and H_2O in atmosphere. The spectra obtained were averages of 128 scans recorded at 4 cm^{-1} resolution. The spectra, measured from samples consisting of 10 vol.% silicon frustule replicas mixed with KBr powder, were referenced to a background of pure KBr powder. Fig. 2.15 reveals FTIR spectra (provided by Harry W. Abernathy) obtained from as-synthesized silicon frustule replicas and the silicon frustules replicas after 40 days of water immersion. The peaks located at 2090 and 2100 cm^{-1} from as-synthesized silicon frustule replicas are associated with Si-H_x vibrations[61, 62]. The obtained peaks located at 2254 and 3741 cm^{-1} from the oxidized silicon frustule replicas are associated with ν(-O_ySi-H_x), and ν(SiO-H) modes of vibration, respectively[63, 64]. Some researchers have correlated visible photoluminescence with this surface specie –O_ySi-H_x[64]. In any event, the FTIR measurements confirmed that the silicon frustules replicas were partially oxidized after 40 days of water immersion.

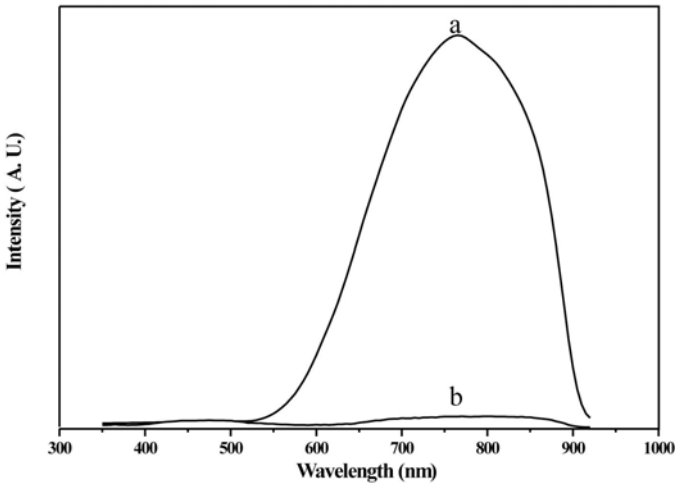

Figure 2.13: a, PL of silicon frustule replicas after partial oxidation in water for 40 days. B, PL spectra of as synthesized silicon frustule replicas. (Published in *Nature*, 446, 172-174, 2007. Data was collected by Dr. Zhitao Kang)

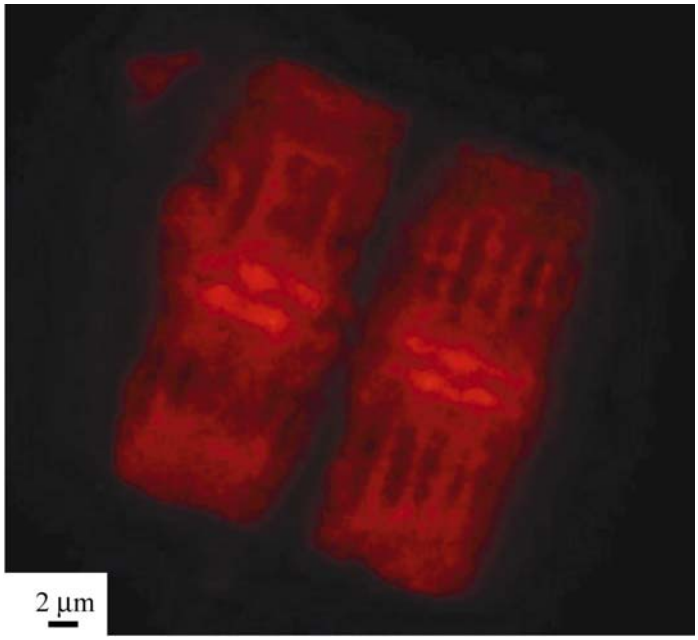

Figure 2.14: A fluorescence microscope image of photoluminescent (PL) silicon frustule replicas (provided by Dr. Matthew B. Dickerson and published in *Nature*, 446, 172- 174, 2007).

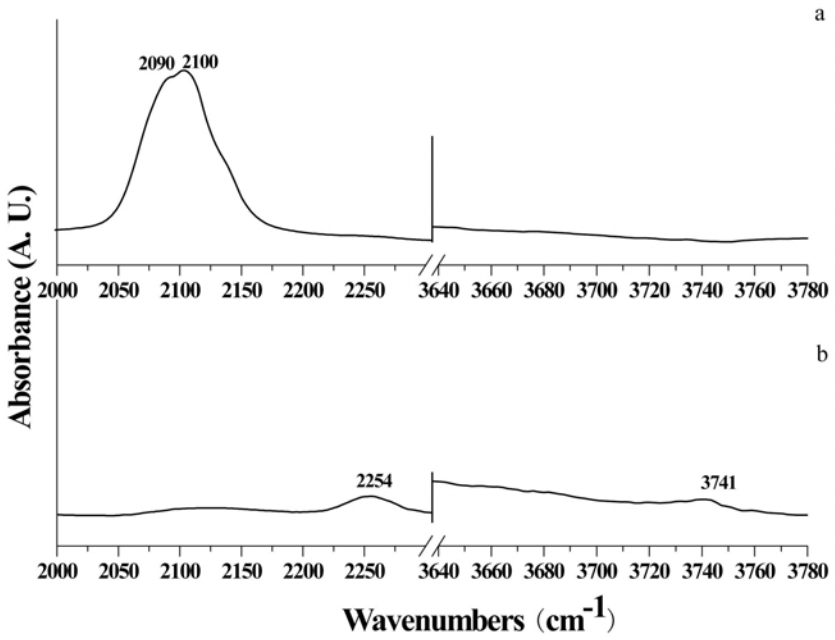

Figure 2.15: a, Fourier Transform Infrared (FTIR) spectrographic analysis of silicon replicas of *Aulacoseira* frustules. Peaks located at 2090 and 2100 cm^{-1} are associated with Si-H_x vibration. b, FTIR spectra obtained after immersion of the silicon frustule replicas in water for 40 days at room temperature. Peaks located at 2254 and 3741 cm^{-1} are associated with $\nu(-O_ySi-H_x)$, and ν(SiO-H) modes of vibration, respectively. (Published in *Nature*, 446, 172- 174, 2007. Data was collected by Harry W. Abernathy)

2.4.2 Possible application of single silicon frustule in gas sensing

Porous silicon has been used in sensors to detect various gas species[31]. BET analyses have indicated that silicon frustule replicas generated by magnesiothermic reaction at 650 ºC possessed a much higher specific surface area, than for the porous silicon produced by anodisation etching[51]. This high specific surface area, which is attributed to the open structure inherited from the diatom frustules, may make silicon frustule replicas attractive for sensitive and rapid gas detection. To evaluate this possibility, a gas sensor prototype (Fig. 2.16a, by Dr. Sehoo Yoo) was fabricated to evaluate gas sensing performance. A single silicon frustule (*Aulacoseira*) replica was placed on a silicon nitride substrate, and platinum electrodes were then deposited to both ends of the replica by focused ion beam deposition from a platinum source (Nova Nanolab 200, FEI Company, USA). The other end of the platinum electrode was connected to gold pads, which were deposited on the silicon nitride substrate. A potentiostat (Gamry Instruments, PA, USA) was used to apply a small bias voltage (100 mV at 100 Hz) across the silicon frustule sensor. The current passing through the sensor was monitored during switching of the sample gas from pure argon to argon containing different concentrations of NO(g) at 300 ^{o}C. The impedance of the silicon frustule sensor increased dramatically upon exposure to low (p.p.m.) concentrations of NO(g) (Fig. 2.16b, by Samuel Shian). It was consistent with the result from P-type porous silicon gas sensor[31]. Fig. 2.17 showed the inductively coupled plasma (ICP) analysis (conducted by Mr. Gene Weeks in University of Georgia with ICP-MS, Wellesley, MA) of the silicon frustule replicas. Most of the impurities were Mg, Al, Na, and Fe elements, which were P-type dopants. Furthermore, changes in NO(g) concentration as low as 1 p.p.m. could be detected. The response (rise) and recovery

(decay) times of this sensor were about 6 seconds and 25 seconds, respectively. Compared to sensors based on the planar porous silicon, this sensor fabricated from a 3D porous silicon frustule replica showed a faster response and needed a lower bias voltage. Such a combination of rapid (≤25 s) and sensitive (1 p. p. m.) detection of NO(g) from a microscale 3D silicon sensor operating with a bias voltage of only 100 mV (instead of several volts) had not previously been achieved. Although the packaging and long-term stable performance of such a sensor will require further development, the high sensitivity and rapid response rate of the silicon frustule replica demonstrate the benefits of such an open, porous, high-surface-area 3D structure. At the same time, the result from this sensor test confirmed that the porous silicon frustule replicas consisted of the interconnected silicon.

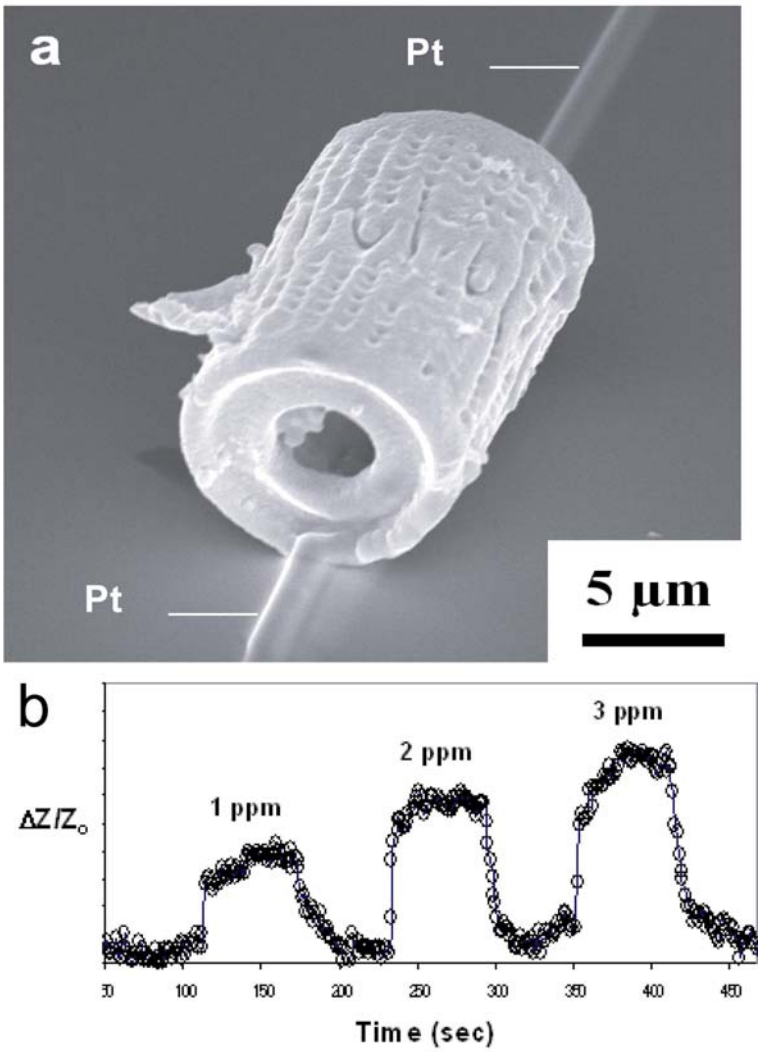

Figure 2.16: a, Gas sensor based on a silicon frustule replica. a, Secondary electron image of an electroded microporous silicon frustule replica (by Dr. Sehoo, Yoo). b, Electrical response of this single silicon frustule sensor to NO(g). ΔZ is the impedance change upon exposure to NO(g), and Z_0 is the sensor impedance in pure flowing argon (by Samuel Shian). (Published in *Nature*, 446, 172- 174, 2007.)

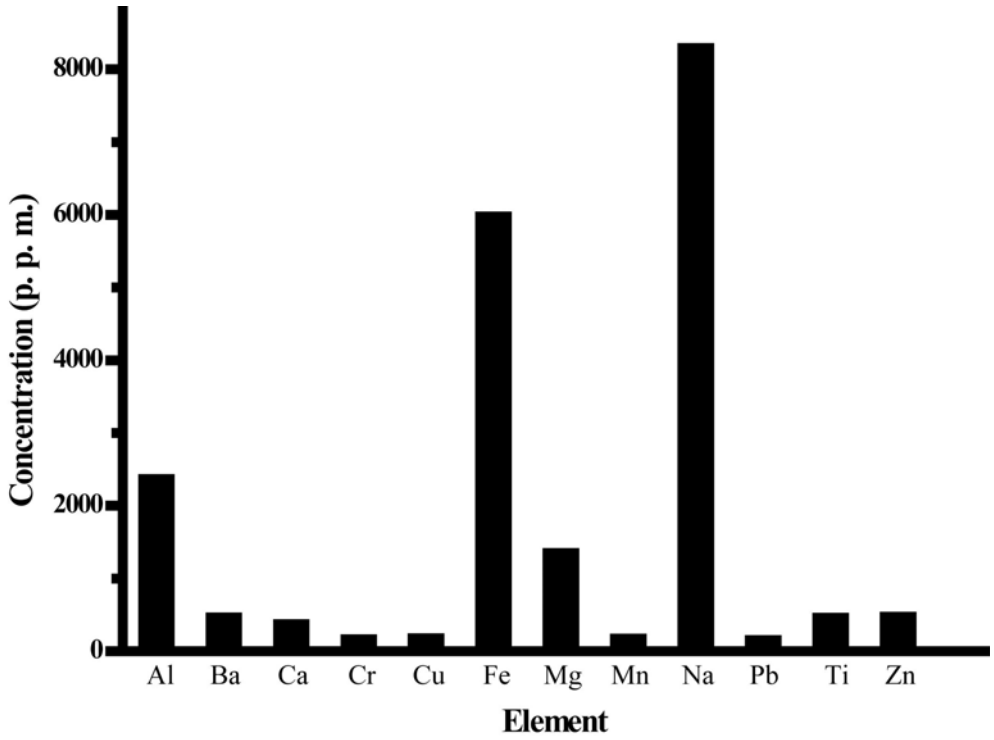

Figure 2.17: ICP analysis of silicon frustule replicas (the concentration of silicon was set to be one).

2.5 Conversion of synthetic silica templates

2.5.1 Experimental design and details

In the previous paragraphs, the conversion of biosilica performs, diatom frustules, into silicon frustule replicas using the magnesiothermic reaction, together with the immersion in acidic solutions has been demonstrated. However the magnesium powder could not be used as the magnesium vapor source for the conversion of small amounts of synthetic silica templates. As indicated above, the magnesium vapor pressure generated directly from magnesium powder was so high that when magnesium silicide would form upon reaction with silica. The Mg_2Si-rich structures would be destroyed during the etching in the hydrochloric acid solution. There were two possible ways to avoid the formation of

magnesium silicide. One approach was to place the small synthetic silica templates in area II illustrated in Fig. 2.11. The other was to use magnesium silicide as the magnesium source. The magnesium gas pressure generated from the magnesium silicide was so low that little or no magnesium silicide would be generated from the synthetic silica templates, but was high enough to allow for the magnesiothermic reaction. Hence, magnesium silicide was chosen as the magnesium vapor source for reaction with small synthetic silica templates. One such synthetic silica template was a silica-based opal (from Dr. Simon Hall, University of Bristol, UK). This template was chosen because: (1) the opal exhibited attractive optical properties and (2) the structure of the opal was very delicate and it was easy to evaluate the extent of shape and feature preservation. Because the magnesium partial pressure from magnesium silicide was relatively low, the distance between magnesium silicide and the opal sample had to be relatively short. In these experiments, the opal was placed on one end of a steel boat and magnesium silicide (Alfa Aesar, 99.5% purity) was placed on the other end. The molar ratio of Mg_2Si to SiO_2 was around 10:1. The distance between magnesium silicide and the opal was fixed to 1 cm. Also, the magnesium consumption caused by reaction with the air sealed in the ampoule could be significant: air sealed in the 6-inch long ampoule with 1-inch diameter could consume magnesium up to around 225 mg. Hence, the steel boat, with magnesium silicide powder and the opal, was sealed in a steel ampoule in a glove box, filled with purified argon. This ampoule was then placed into a tube furnace. The furnace was heated to 850 ºC, and held at this temperature for 2.5 h. After the furnace was cooled, the ampoule was removed and cut open. The reacted opal was subsequently immersed in a 3 M HCl solution (molar $HCl:H_2O:EtOH$ ratio 1.98:4.72:8.88) for 3 hours at room

temperature to selectively dissolve the magnesia. The converted opal was washed with anhydrous alcohol and dried, all within the argon atmosphere glove box.

2.5.2 Characterization

Fig 2.18 reveals the secondary electron images of a silica-based opal, and the opal after the magnesiothermic reaction and immersion in a hydrochloric acid solution, respectively. The starting opal was composed of silica spheres with a diameter of 240±7 nm (The diameter measurement was based on the SEM images and the average diameter was calculated from the measured diameters of 20 randomly selected spheres. See Appendix C for SEM calibration). After the conversion, the average diameter decreased to 213±2 nm. Such a ~10% irreversible shrinkage has been observed during drying of the porous silicon[65]. However, the overall close-packed structure was still retained after conversion. Energy dispersive X-ray analyses of the opal before and after conversion into porous silicon are shown in Fig. 2.19. The silica opal was converted into porous silicon opal with some residual silica. Reflectivity spectra were acquired with a custom microreflectivity system (Nanophotonics Lab, Georgia Institute of Technology). The spot size was 100 μm and the spectra range of 450 nm-2200 nm was explored using a tungsten-halogen lamp and a combination of silicon (Thorlabs), indium gallium arsenide (Thorlabs), and lead sulfide (Electro-optical Systems, Inc) detectors. An optical chopper (Edmund Optics) and a lock-in amplifier (Princeton Applied Research) were used for signal acquisition. The microreflectivity spectra of a silica opal and a porous silicon opal replica are shown in Fig. 2.20. The wavelengths of maximum reflection were 506 nm and 634 nm for silica and porous silicon opals, respectively.

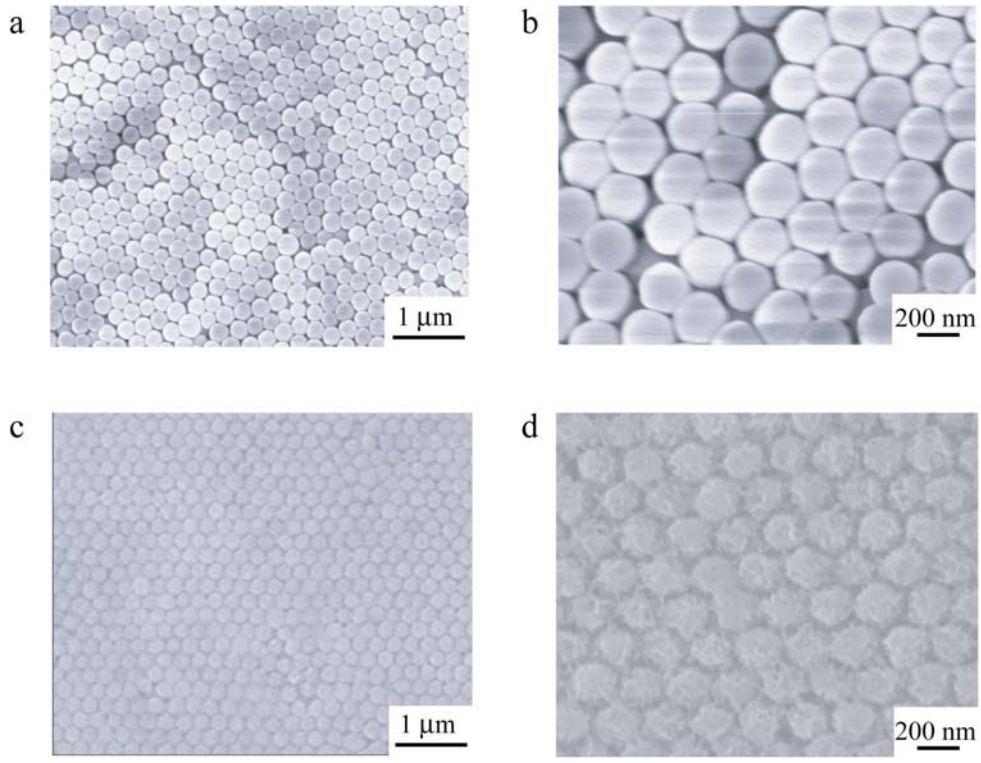

Figure 2.18: a and b, Low magnification and high magnification secondary electron images of a silica opal, respectively. c and d, Low magnification and high magnification secondary electron images of a porous silicon opal, respectively.

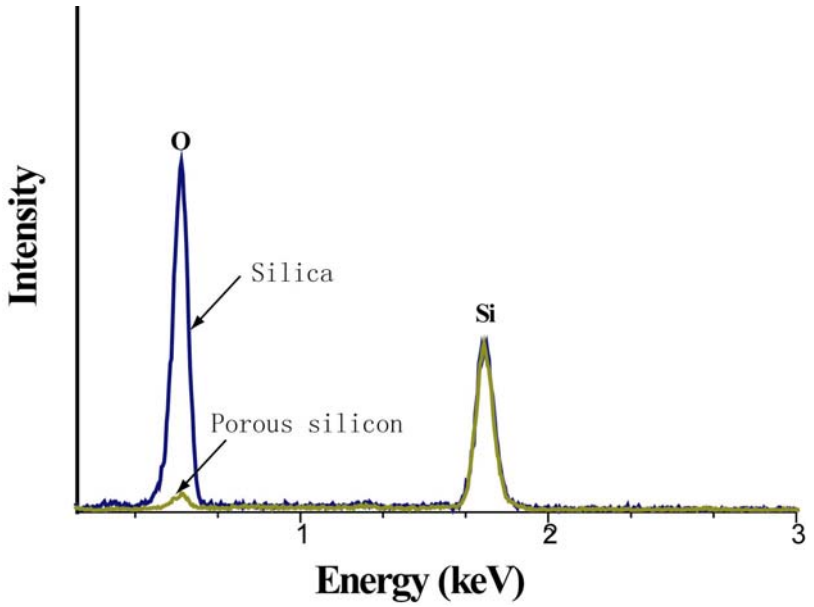

Figure 2.19: Energy dispersive X-ray analyses of a silica opal and the porous silicon opal replica.

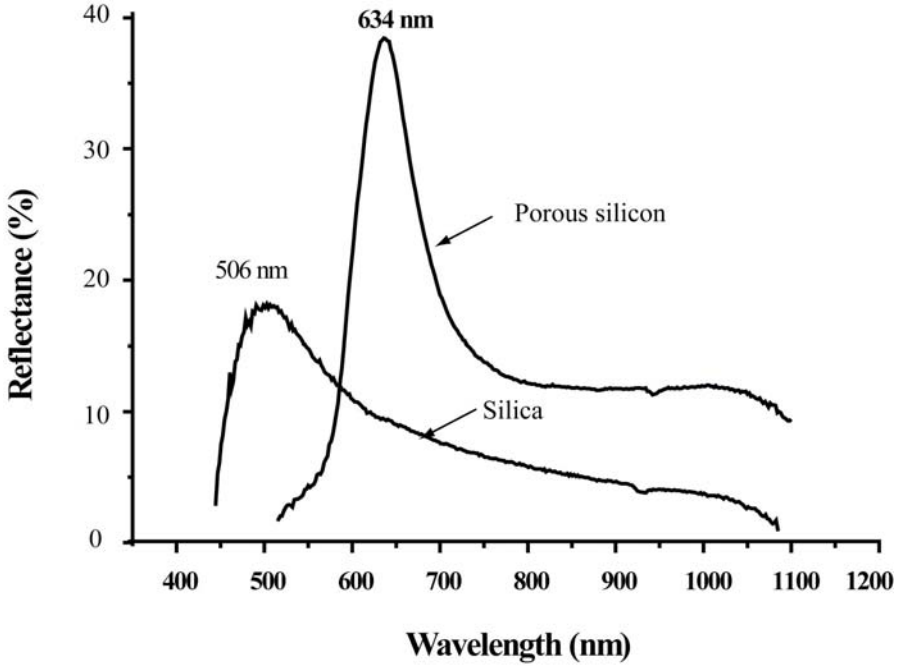

Figure 2.20: Microreflectivity of a silica opal and a porous silicon opal replica, respectively.

2.5.3 Discussion

The wavelength of maximum reflection (λ_{max}) from (111) planes in an fcc opal has been calculated by the derivative equation of Bragg's law:

$$\lambda = 1.633 d \sqrt{n_{ave}^2 - n_{air}^2 \sin^2 \theta} \quad (2.3)$$

$$n_{ave} = f n_{materials} + (1 - f) n_{air} \quad (2.4)$$

where λ is the wavelength of maximum reflection, d is the diameter of the spheres in the opal (obtained from the measurement on SEM image), n_{ave} is the average refractive index of the material and θ is the angle of the direction of incident light with respect to the normal of the (111) plane (θ=0 for the (111) plane). Fig. 2.21 reveals the refractive index of a porous silicon layer (p-doped, 0.01 Ω cm) with 65% porosity as functions of light energy and wavelength[66]. In the wavelength range of 450-1000 nm, the refractive index changed from 2.2-1.7. So the average refractive index could be assumed to be 2.0. For a fcc structure, a solid filling volume ratio of 0.74 was assumed. The parameters used in the λ_{max} calculation, and the expected and measured wavelengths of maximum reflection are summarized in Table 2.2. The measured wavelengths were close to the expected wavelengths, which provided additional evidence that the structure was largely converted into porous silicon.

Table 2.2: Comparison of calculated and measured wavelengths of maximum reflection from silica and porous silicon opals.

	N	*d* (nm)	*f*	n_{ave}	Expected λ_{max} (nm)	Measured λ_{max} (nm)
Silica opal	1.45	240±7	0.74	1.33	522±15	506
Porous silicon opal	2	213±2	0.74	1.74	605±6	634

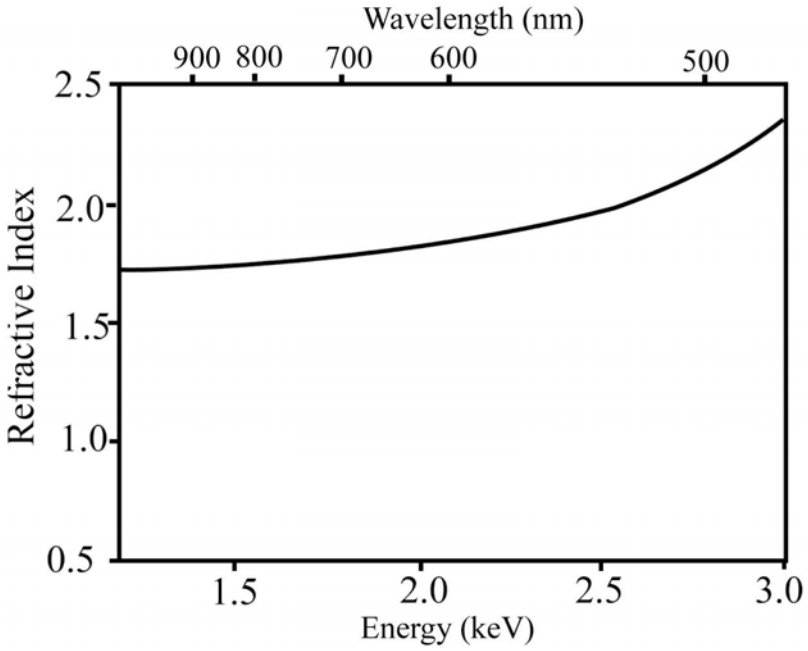

Figure 2.21: Refractive indices of a porous silicon layer (p-doped, 0.01 Ω cm) with 65% porosity[66].

2.6 Summary

Diatom frustules, biologically derived silica-based templates, were successfully converted into silicon replicas through magnesiothermic reaction along with HCl etching and HF etching. XRD, SEM, TEM and XPS analyses were used to characterize these silicon structures. The interconnected silicon structures retained the complex 3D morphologies and fine (nano) features of diatom frustules. These silicon replicas possessed a very high specific surface area (>500 m^2/g) and large populations of micropores (≤2 nm). A prototype microsensor fabricated from such a silicon frustule replica demonstrated rapid (≤25 s) and sensitive nitric oxide gas detection (1 p.p.m.) using a very low applied bias voltage of 100 mV. Partially-oxidized silicon frustule replicas also exhibited photoluminescence under UV light. This process combining biology and synthetic chemistry can be used to fabricate materials with complex 3-D shapes and compositions. Because of the abundance of biologically-derived materials, may enable a variety of low cost, high performance electronic, optical and chemical devices.

With the use of magnesium silicide as the magnesium gas source, intricate synthetic silica opals were successfully converted into porous silicon replicas, which demonstrates that this process can also be applied to synthetic silica templates.

CHAPTER 3: METALLIC CONVERSION

Porous noble metals have potential application in catalysis[67, 68], biosensor technology[69], biofiltration[70], and electrochemistry[71]. Nanoporous metals have been prepared by a dealloying process, which involves the selective dissolution of a specific metal element from a multiphased alloy[72]. Porous noble metals with controlled shapes have also been fabricated through template synthesis[73-75]. Such templates have included dextran paste, polyacrylamide beads, and echinoid skeletal structures[73-75]. Here self-supporting, nanostructured, 3-D, porous, noble metal hierarchical structures have been prepared by the electroless deposition method, using diatom frustules as sacrificial templates.

3.1 Experimental design and details

Because of their abundance and diversity, diatom frustules have attracted recent attention as templates for the formation of metallic nanostructured materials[12, 76]. However, the uniform deposition of a metal on and inside the complex 3-D structure of a diatom frustule by line-of-sight physical or chemical vapor deposition is difficult. Wet chemical processes (*e. g.,* electrodeposition, electroless deposition) are effective means of depositing some metals (*e. g.*, Ag, Pd, Au and Ni) on complex conductive structures[77, 78]. The direct electrodeposition of such metals onto 3-D silica templates is complicated by the insulating character of silica. In Chapter 2, the conversion of silica-based diatom frustules into silicon-based structures with precise shape retention using a magnesiothermic method (together with immersion in an HCl solution) was demonstrated[79]. Because the porous silicon structures possessed much higher electronic conductivities than silica, it was possible to utilize electrodeposition.

Silver was deposited onto/into the porous silicon frustule replicas by immersing 100 mg of the porous silicon frustule replicas in 200 ml of a silver electroless plating solution preheated to 90 ºC for 1 minute. After removal from the solution by filtration and washing with de-ionied water, the Ag-coated replicas were immersed in a 20 wt% NaOH solution at 60 ºC for 3 hours to remove the underlying silicon templates. For synthesis of gold and palladium frustule replicas, 100 mg of silicon replicas were immersed in 350 ml of palladium and 150 ml of gold electroless solution at 60 ºC for 1 minute, respectively. The Ag and Au electroless solutions were obtained from Transene Inc. (Danvers, MA). The compositions of the Ag, Au, Pd electroless-plating solutions are listed in Table 3.1, 3.2, 3.3. Two different types of silicon frustule replicas were used in the present research. One type of silicon frustule replicas (labeled as 650 ºC silicon frustule replicas) was obtained by reacting magnesium gas with diatom frustules at 650 ºC for 2.5 hrs, followed by the immersion in a 1 M HCl solution for 4 hours. The other type of silicon frustule replicas (labeled as 900 ºC silicon frustule replicas) was obtained by reacting magnesium gas with diatom frustules at 900 ºC for 1.5 hrs and subsequent immersion in a 1 M HCl solution for 4 hours.

Table 3.1: The composition of silver electroless solution (*Transene Inc*., Electroless Silver Solution)

Component	wt%
Silver Cyanide	<1
Potassium Cyanide	<1
Sodium Hypophosphite	1-5
Distilled Water	>93

Table 3.2: The composition of gold electroless solution ((*Transene Inc*., Bright Electroless Gold Solution)

Component	wt%
Potassium Gold Cyanide	<1
Citric Acid	1-5
Ethylenediamine Tetracetic Acid, Tetrasodium salt	1-5
Ammonia Hydroxide	1-5
Distilled Water	>84

Table 3.3: The composition of palladium electroless solution[80]

Component	Concentration
$PdCl_2$	2g/l
$Na_2EDTA{\cdot}2H_2O$	40.1g/l
NH_3(28%)	198ml/l
N_2H_4	5.6ml/l
PH	10-10.4

3.2 Characterization

Fig. 3.1 reveals the secondary electron images of 650 ºC and 900 ºC silicon frustule replicas, respectively. For both reaction temperatures, the silicon frustule replicas retained the shape of the silica diatom frustules. However, the 650 ºC silicon frustule replicas were composed of much smaller crystallites than the 900 ºC replicas. The Scherrer analyses of the XRD patterns (Fig. 3.2) revealed that the average crystallite sizes were 13 nm and 304 nm for the 650 ºC and 950 ºC silicon frustule replicas, respectively. Other parameters related to the silicon frustule replicas are summarized in Table 3.4. The 650 ˚C silicon frustule replicas possessed substantially higher specific surface area and more mesopore volume than the 900ºC silicon frustule replicas. Fig. 3.3 shows the EDS analyses of the 650 ºC and 950 ºC silicon frustule replicas, respectively. The resulting silver product (Fig. 3.4) generated from the 650 ºC silicon frutule replicas retained the three-dimensional (3D) cylindrical morphology and nanoscale features inherited from the starting *Aulacoseira* diatom frustules. The secondary electron (SE) image of a silver replica after ion milling (Fig. 3.4b) reveals the surface morphology of the frustule wall. A higher magnification SE image (Fig. 3.4c) shows that the product was porous and composed of silver nanoparticles with a size around 25 nm. On the contrary, the final Ag product (Fig. 3.5a) generated from the 900 ºC silicon frustule replicas did not retain the frustule morphology. This product was also composed of much larger silver particles (~200 nm) (Fig. 3.4b). The energy dispersive X-ray pattern (Fig. 3.4d) and X-ray diffraction pattern (Fig. 3.6a) both confirmed that the final products were solely composed of silver. The average grain sizes were estimated to be 14 nm and 42 nm from Scherrer analyses of the XRD patterns for these two samples, respectively.

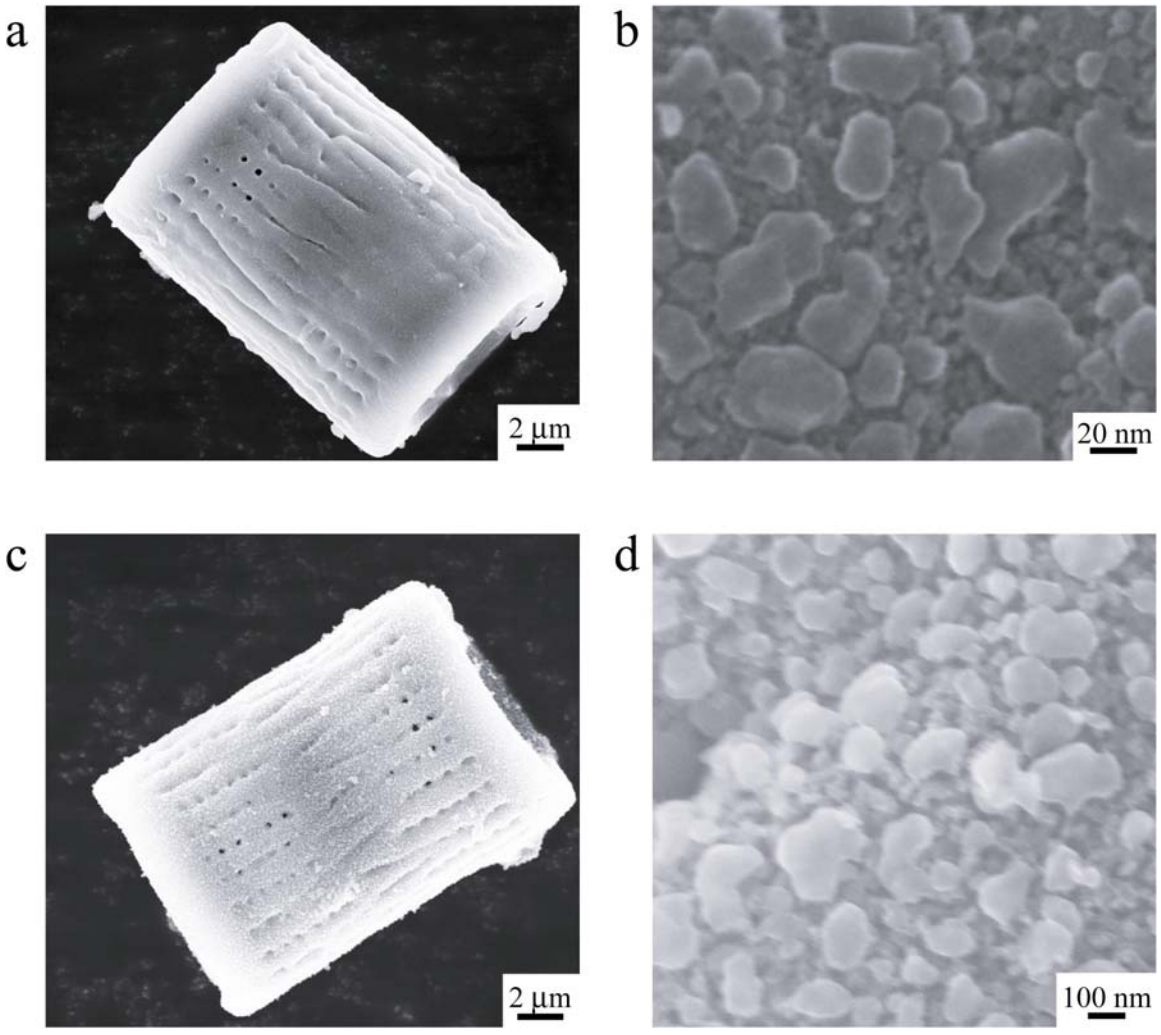

Figure 3.1:a and b, Low magnification and high magnification SE images, respectively, of a silicon frustule replica synthesized by reaction at 650 ºC for 2.5 hours. c and d, Low magnification and high magnification SE images, respectively, of a silicon frustule replica synthesized at by reaction at 900 ºC for 1.5 hours.

Table 3.4: Comparison between 650 ºC silicon replicas and 900 ºC silicon replicas.

Processing Temperature/Time	Average grain size (nm)	BET surface area (m^2/g)	Porosity (cc/g) (diameter < 50 nm)
650 ºC/2.5 h	13	541	0.52
900 ºC/1.5 h	304	53	0.03

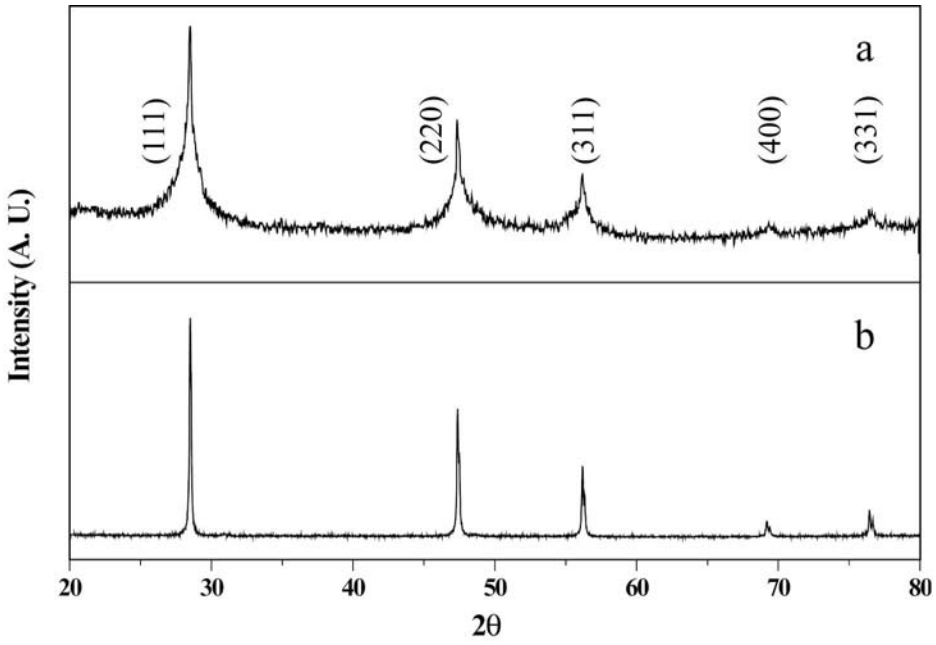

Figure 3.2: a and b, XRD patterns of silicon frustule replicas synthesized by magnesiothermic reaction at 650 ºC/2.5 h and 900 ºC/1.5 h and then immersion in 1 M HCl solution at room temperature for 4 hours, respectively.

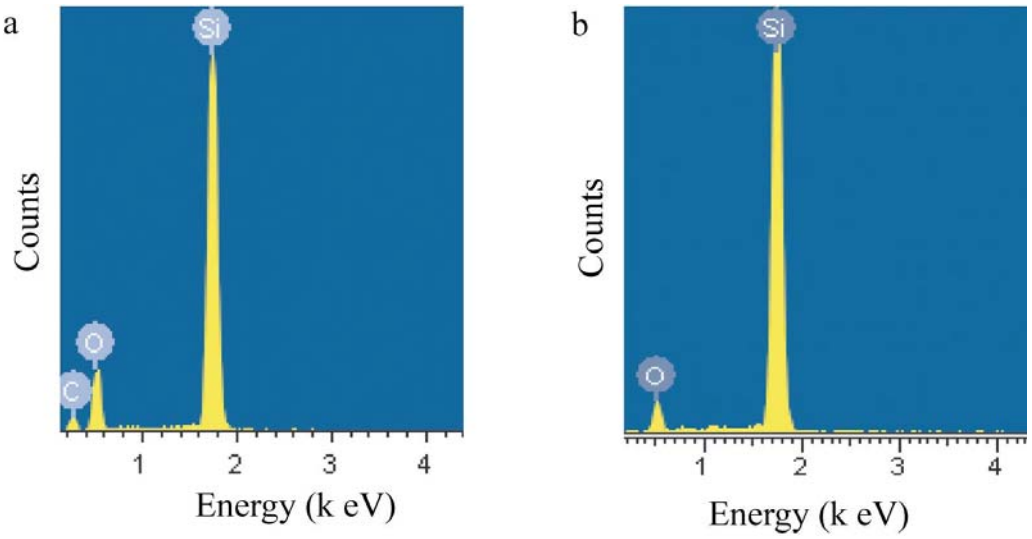

Figure 3.3: a and b, EDS analyses of silicon frustule replicas synthesized by magnesiothermic reaction at 650 ºC/2.5 h and 900 ºC/1.5 h and then immersion in 1 M HCl solution at room temperature for 4 hours, respectively.

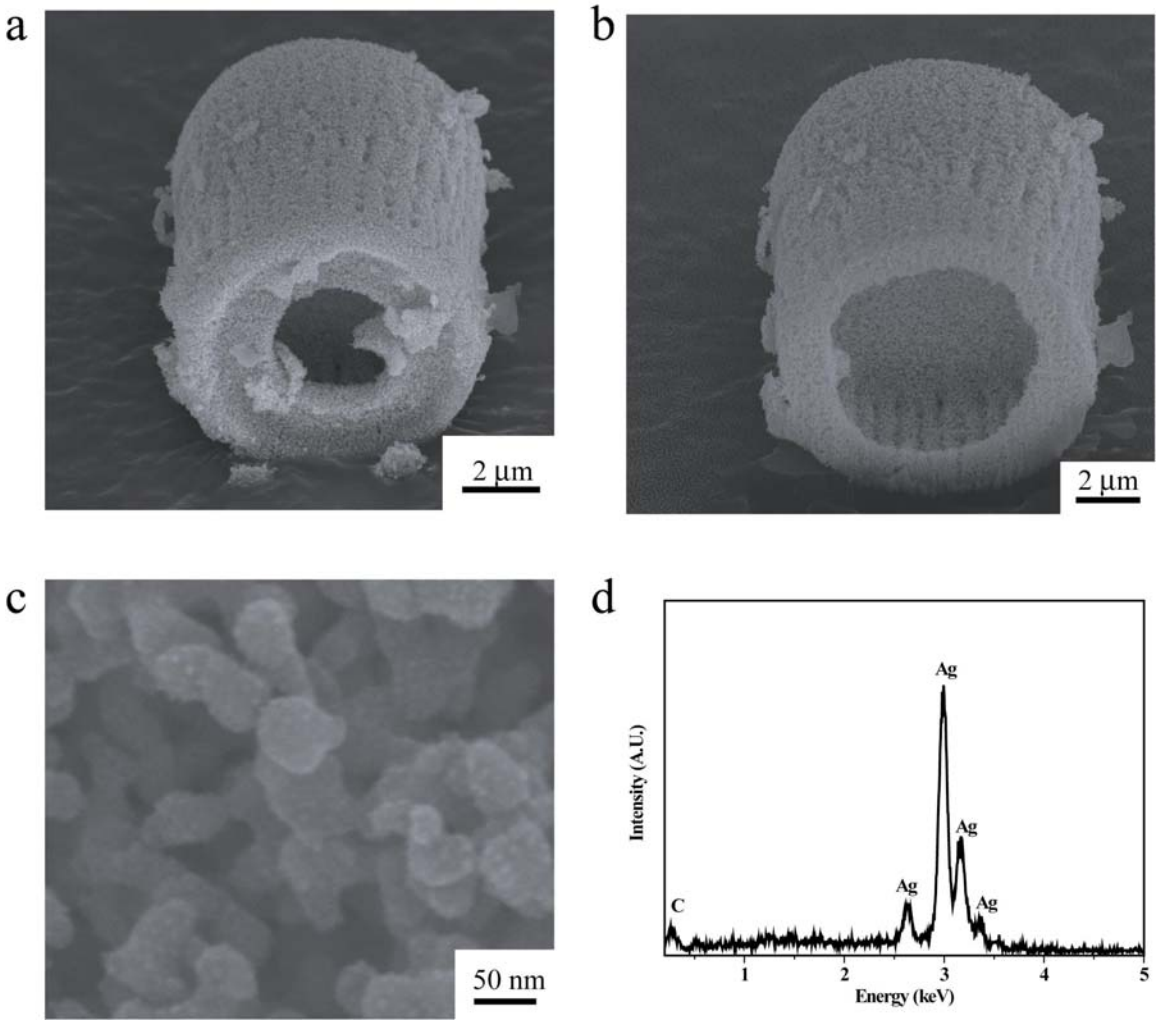

Figure: 3.4 a, Secondary electron image of a silver frustule replica generated from a silicon frustule replica synthesized at 650 ºC/2.5h. b, Secondary electron image of an ion beam milled cross-section of the silver replica in a, revealing the inner wall morphology of the silver diatom replica. c, High resolution secondary electron image of the silver particles comprising the silver frustule replica in a. d, Energy dispersive X-ray analysis obtained from the silver frustule replica shown in a. (Figure 3.4a-c were provided by Dr. Sehoo Yoo)

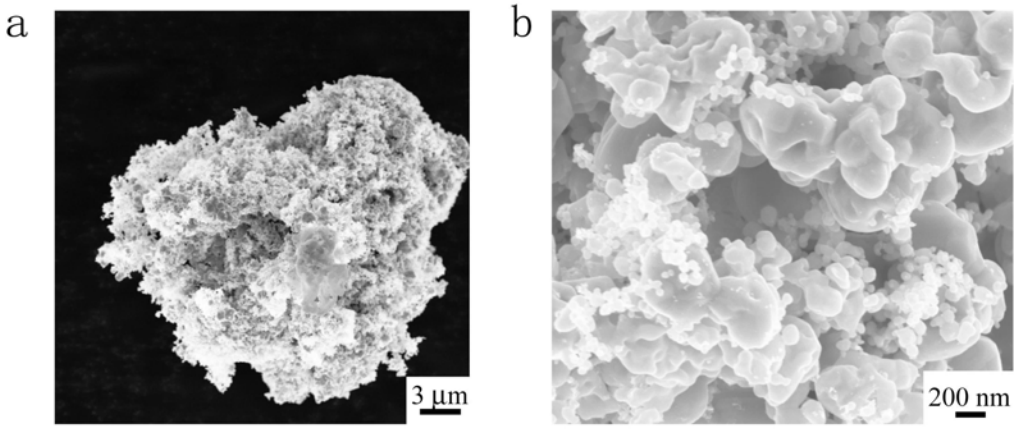

Figure 3.5: a, Secondary electron image of the silver sample generated from silicon frustules replicas synthesized at 900 ºC/1.5 h. b, High resolution secondary electron image of the silver particles comprising the silver sample in a.

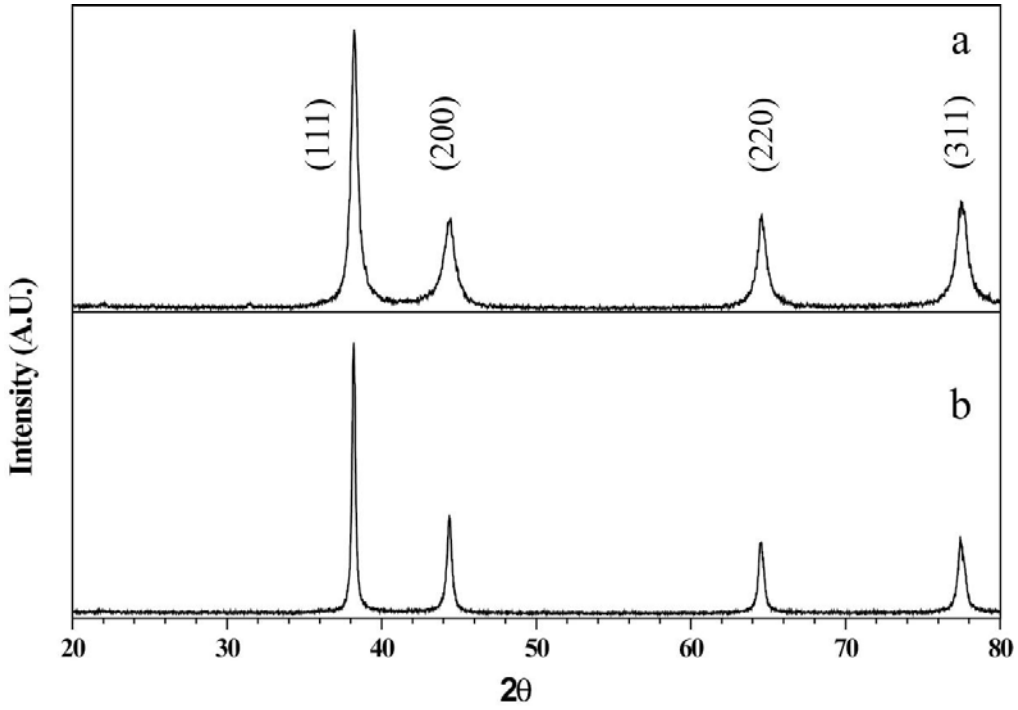

Figure 3.6: a and b, XRD patterns obtained from silver samples using silicon frustule replicas synthesized at 650°C/2.5h and 900°C/1.5h as templates, respectively.

As for the case for silver plating, the palladium and gold frustule (Fig. 3.7 and Fig 3.8) replicas were also successfully fabricated only with the 650 ºC/2.5 h silicon frustule replicas as the starting templates. The average crystallites of Au and Pd sizes were 50 nm and 43 nm obtained from Scherrer analyses of the XRD patterns (Fig. 3.9), respectively. The specific surface areas calculated from BET plots (Fig. 3.10) were 22.77 m^2/g, 10.06 m^2/g and 13.33 m^2/g for silver, gold, and palladium frustule replicas, respectively.

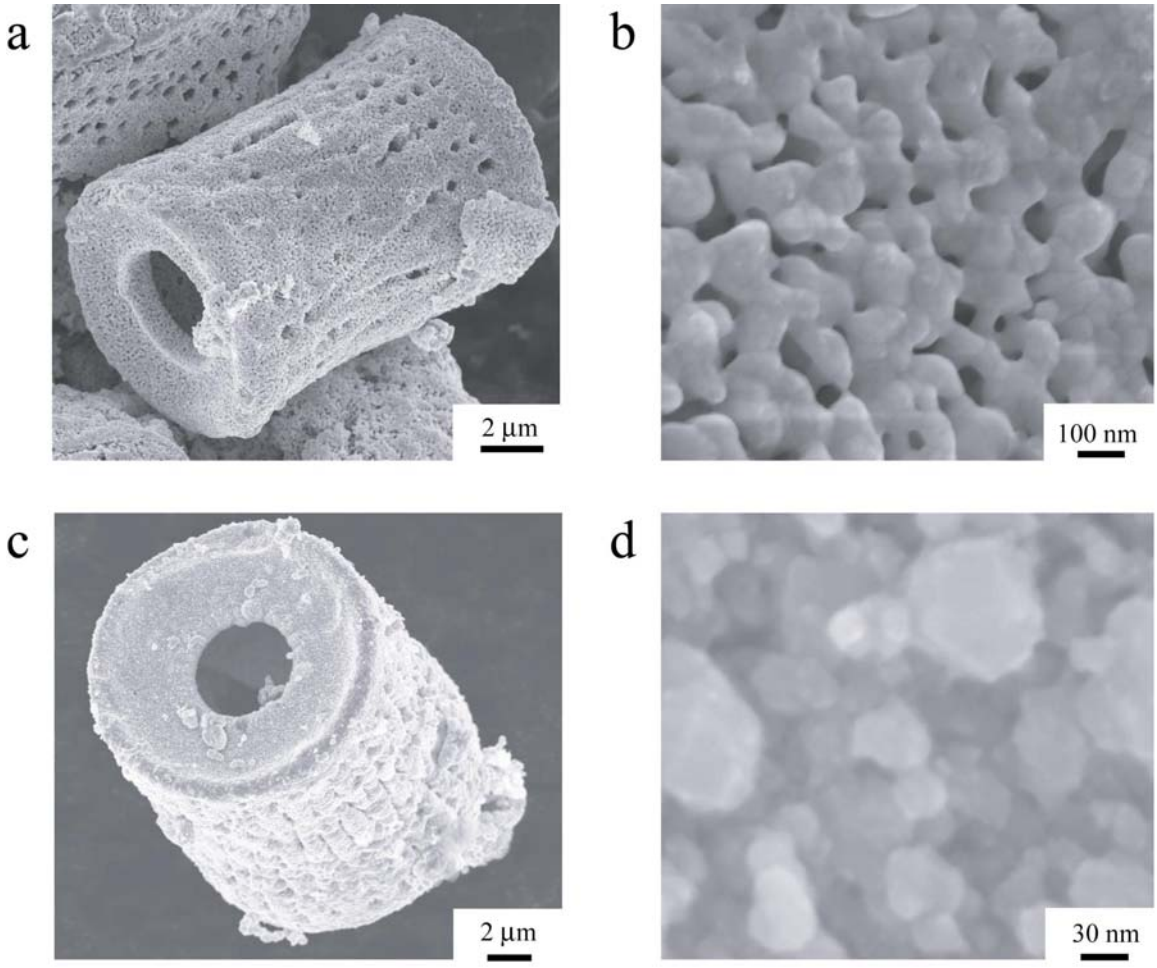

Figure 3.7: a, Secondary electron image of a gold frustule replica. b, High resolution secondary electron image of adjacent gold nano particles which comprised the gold frustule replica in a. c, Secondary electron image of a palladium diatom replica. d, High resolution secondary electron image of palladium nano particles, which comprised the palladium frustule replica in c.

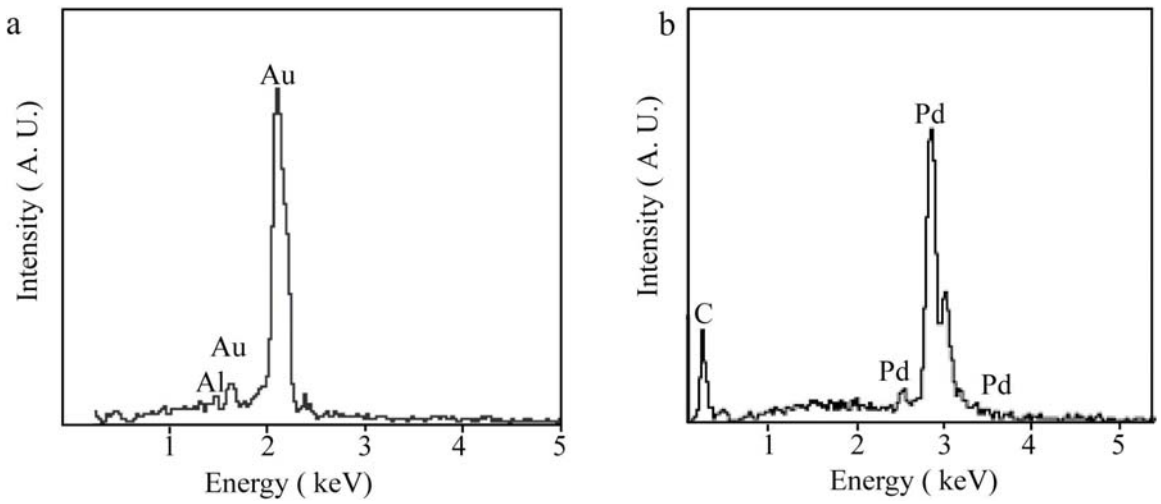

Figure 3.8: a, Energy dispersive X-ray analysis of a Au frustule replica. b, Engergy dispersive X-ray analysis of a Pd frustule replica.

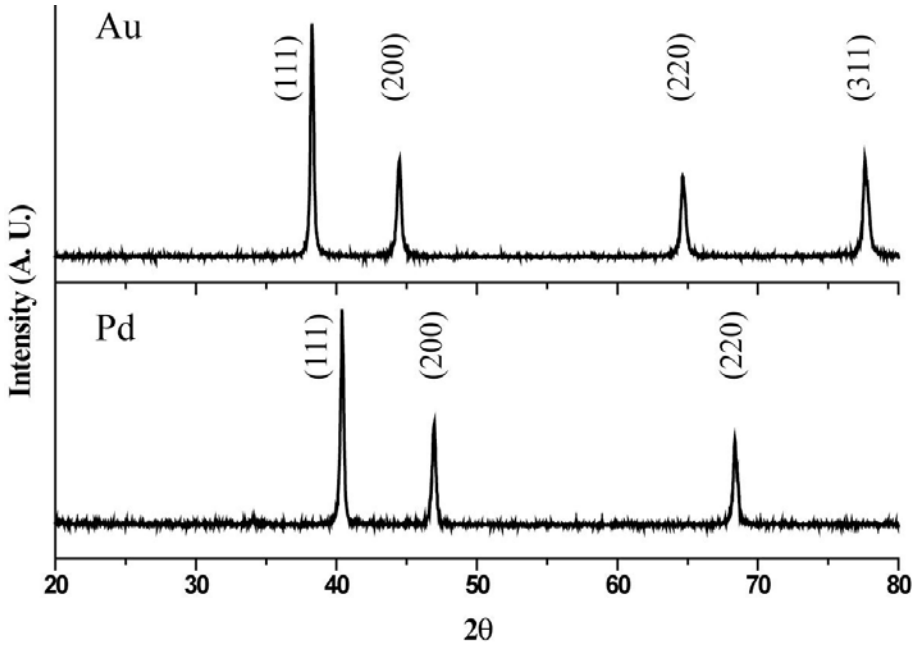

Figure 3.9: X-ray diffraction patterns of Au frustule replicas and Pd frustule replicas, respectively.

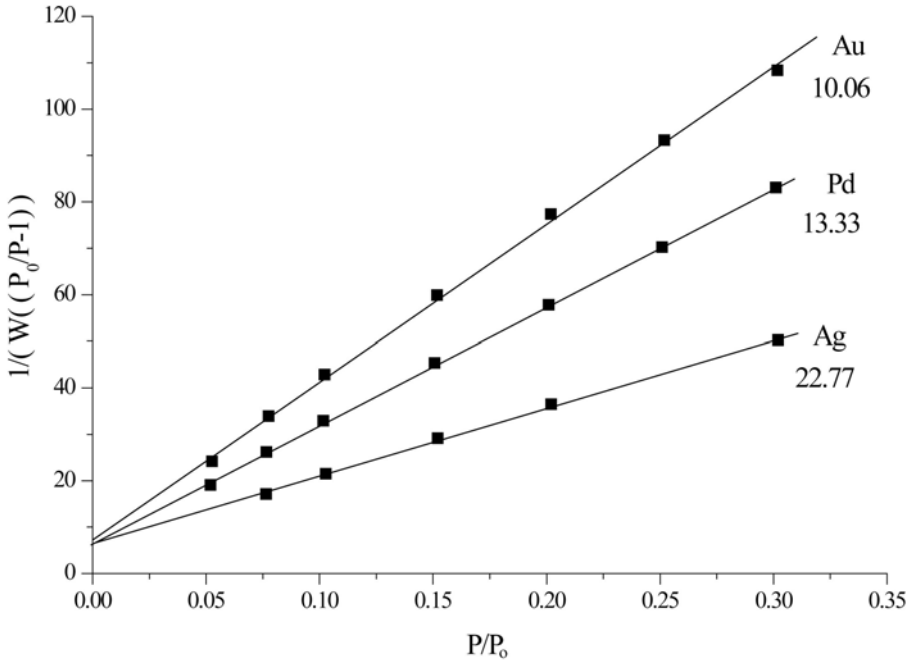

Figure 3.10: BET plots for silver, gold, and palladium frustules replicas, respectively.

3.3 Discussion

Some researchers have studied the metal deposition onto porous silicon via immersion plating from aqueous and nonaqueous solutions. These authors suggested that the following reactions occurred during the process such deposition[78, 81]:

$$Si+2H_2O \rightarrow SiO_2+4H^+ +4e^- \quad (3.1)$$

$$SiH_x+2H_2O \rightarrow SiO_2+(4+x)H^+ +(4+x)e^- \quad (3.2)$$

The oxidized layer formed on the silicon particles may act as insulator and hinder the further reaction by reaction (3.1) or (3.2). For this reason, electroplating solutions with a reducing agent were used in all of these experiments. The difference in the deposition behavior for the 900 ºC/1.5 h and 650 ºC/2.5 h silicon frustule replicas related to the difference in morphology (surface area, pore size) and grain size of these silicon templates. These factors would affect the reactivity of different porous silicon samples. Because 650 ºC silicon frustules replica had a higher surface area and smaller crystallize size, there were more defects such as kinks, grain boundary and steps in the sample[77, 78]. These defects could be potential nucleation sites. The silver particles nucleated at these sites and grew until the reaction finished. Therefore, the average crystallite size in the silver samples generated from the 650 ºC/2.5 h silicon frustule replicas was much smaller than the one from 900 ºC/1.5 h silicon frustule replicas. The grown silver nano particles connected each other to form a metal replica and retained the shape inherited from the diatoms. While the metal source was consumed at fewer nucleation sites to form bigger silver particles on 900 ºC/1.5 h silicon frustule replicas, thus causing the loss of original shape.

3.4 Summary

Metallic diatom frustule replicas (silver, gold, and palladium) with intricate and well-controlled 3D morphologies have been synthesized. In this process, the diatom frustules were first converted into porous silicon frustule replicas. Electroplating was then used to deposit metals onto such porous silicon frustule replicas. Porous silicon frustule replicas with high surface areas synthesized at low temperatures (*e.g.,* 650 ºC/2.5 h) were essential for the successful metal replication. The final freestanding metallic frustule

replicas were obtained by etching the underlying silicon away in a 20 wt% sodium hydroxide aqueous solution at 60 ºC for 3 hours. The BET surface areas were 22.77 m^2/g, 10.06 m^2/g and 13.31 m^2/g for silver, gold and palladium replicas, respectively.

CHAPTER 4: SILICON CARBIDE CONVERSION

Silicon carbide is a widely used material with many attractive properties that include excellent oxidation resistance, high thermal conductivity, high hardness and strength[82, 83]. Porous silicon carbide may also be used in blue light emitting diodes[84] and substrates for epitaxial film growth[85]. Silicon carbide structures with complex, and reproducible 3D shapes have been synthesized in this work, starting from the silica-based diatom frustules.

4.1 Experimental design and details

Though the carbothermal reduction method can be used to directly convert silica into silicon carbide, the shape of silica micropreform reactants would not be retained because intermediate gas phases (SiO, Si) are involved in this process[86, 87]. As a result, the reduction reaction wouldn't be able to compete on surface of the frustules or within the frustules. The reduction product wouldn't retain the shape of microreactant. To achieve shape-preserved SiC frustule replicas, the silica-based diatom frustules were first converted into porous silicon frustule replicas in this work (as described in Chapter 2). The silicon frustule replicas were then coated, and allowed to react with carbon.

4.1.1 Liquid coating method

The silicon frustule replicas were stirred in an acetone solution containing 15-25% (volume) phenolic resin (SP-6877, Schenectady International, N. Y.) for 30 minutes. The frustules were then filtered from the solution and the acetone was allowed to evaporate from the frustules. The dried specimens were placed in a tube furnace, heated to 1100-1200 °C at a rate of 300 °C/hr, and held at that temperature for 5-12 hrs. The resulting black powder was immersed in a 10 wt% sodium hydroxide aqueous solution at 60 °C for 3 hrs to remove the residual unreacted silicon.

4.1.2 Gas deposition method

600 mg of porous silicon frustule replicas were placed in an alumina boat (2.25-inch long, 1.5-inch wide and 0.25-inch high), which was then positioned in a 3-inch diameter mullite tube furnace. The tube was purged with argon (99.999% purity) at room temperature for 2 hours, and then heated at 300 ˚C/hr to 950 ˚C. At this temperature, a gas mixture of 10 vol%CH_4/90 vol%Ar was passed at a rate of 120 sccm through the tube for 2.5 hours. The tube was then purged with Argon for another 0.5 hr. The furnace temperature was then raised at 200 ˚C/hr to 1200 ˚C and held for 12 hours.

4.2 Characterization

4.2.1 Characterization of silicon carbide frustule replicas generated from the liquid coating method

Fig. 4.1a-c reveals the X-ray diffraction patterns obtained from the samples coated using different concentrations of resin, and fired at different temperatures for different times. All of these specimens were comprised of mixtures of silicon carbide and silicon. When silicon frustule replicas were coated using an acetone solution with 15 vol% resin, the product mixture contained more silicon carbide after firing at 1200 ºC for 12 hours than after firing at 1100 ºC for 5 hours. This was attributed to less reaction between carbon paralyzed from the resin and silicon at a lower temperature for a shorter time. When an acetone solution with a higher concentration of resin was used, the content of silicon carbide in the mixture was increased, presumably because more carbon was deposited on the surface of silicon frustule replicas after acetone evaporation. Fig. 4.1d shows the X-ray diffraction pattern of the mixture after heating at 1200 ºC for 12 hours and immersion in a 10 wt% sodium hydroxide aqueous solution for 3 hours. Only silicon carbide was

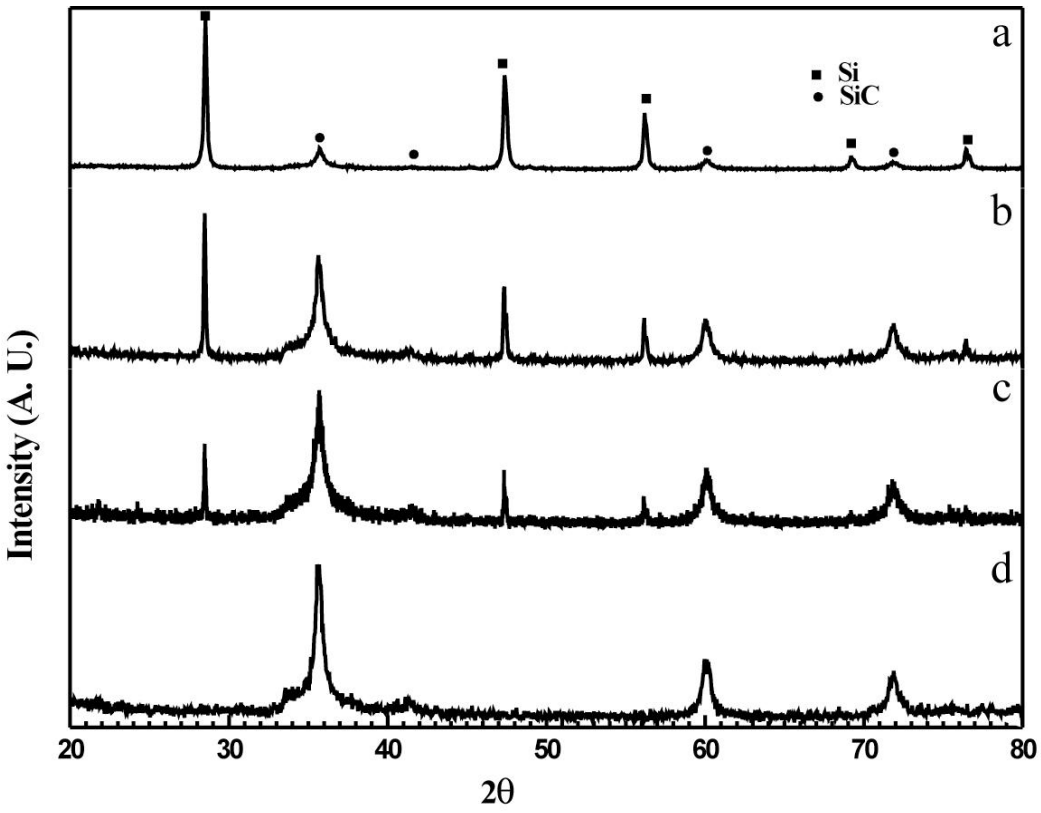

Figure 4.1: XRD patterns obtained from a, silicon frustule replicas (900 °C/1.5 h) coated in an acetone solution with 15 vol% resin and heated to 1100 °C and held for 5 hrs. b, silicon frustule replicas (900 °C/1.5 h) coated in an acetone solution with 15 vol% resin and heated to 1200 °C and held for 12 hrs. c, silicon frustule replicas (900 °C/1.5 h) coated in an acetone solution with 25 vol % resin and heated up to 1200 °C and held for 12 hrs. d, An sample in c after immersion in a 10 wt% sodium hydroxide aqueous solution at 60 °C for 3 hrs.

detected after this NaOH treatment. A secondary electron image of the sample after the NaOH treatment is shown in Fig. 4.2a. The frustule shape was well retained. Energy dispersive X-ray analysis (Fig. 4.2b) reveals the carbon peak together with silicon peak (gold peak from a sputtered coating, oxygen peak from some oxidation of silicon carbide sample in air, and aluminum peak from the aluminum sample holder). Fig. 4.3a-b reveals bright field transmission electron images from ion-milled cross sections of the silicon carbide replicas after the NaOH treatment. Rows of pores and a circular hole inherited from the starting diatom frustules can be seen. A high resolution transmission electron image (by Dr. Ye Cai), shown in Fig. 4.3c, reveals the lattice fringes of adjacent silicon carbide nanoparticles. No other phase was detected at internal grain boundaries, which indicated that the silicon carbide nanoparticles were interconnected to form 3D continuous structures. Consistent with the XRD patterns and energy dispersive X-ray analyses, the electron diffraction pattern (Fig. 4.3d) only exhibited diffraction spots consistent with silicon carbide.

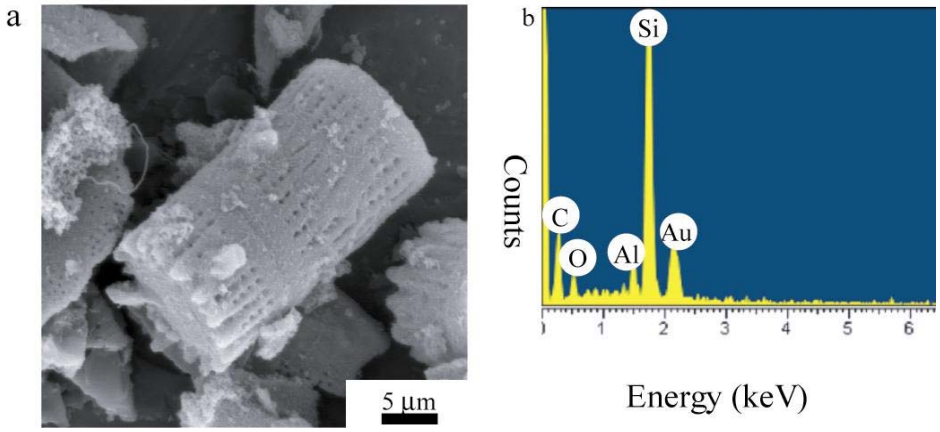

Figure 4.2: a, Secondary electron image of a silicon carbide frustule replica generated by the liquid coating method. b, Energy dispersive X-ray analysis of the silicon carbide replica.

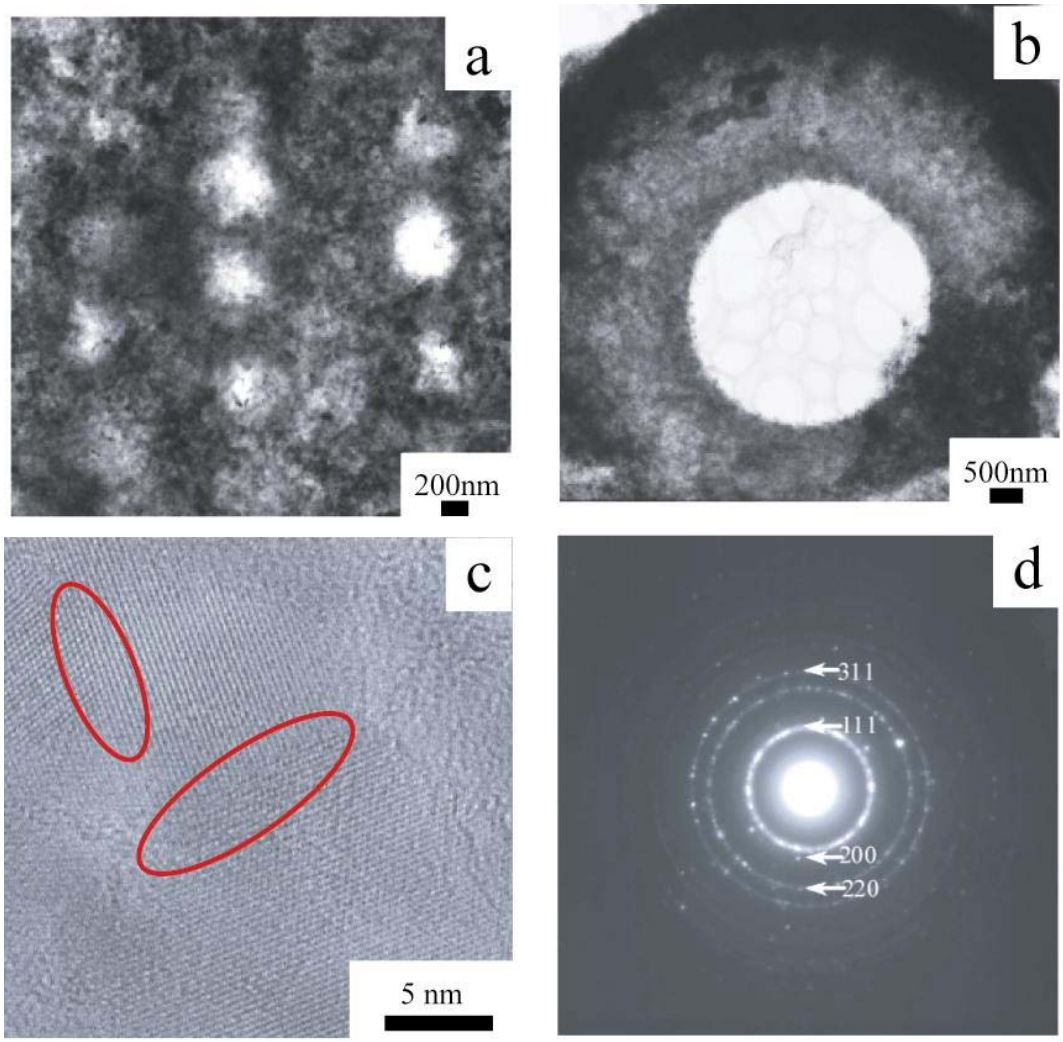

Figure 4.3: a and b, Bright field transmission electron images of ion-milled cross-sections of silicon carbide frustule replicas, respectively. c, High magnification transmission electron image of adjacent silicon carbide nanoparticles. d, Selected area electron diffraction pattern from silicon carbide frustule replicas (Provided by Dr. Ye Cai).

4.2.2 Characterization of silicon carbide frustule replicas generated from gas deposition method

Fig. 4.4a reveals a secondary electron image of a silicon carbide frustule replica. The overall cylindrical shape and nanoscale pores were preserved. The secondary electron image of a silicon carbide replica after ion milling (Fig. 4.4b) reveals that the thickness of the frustule wall was around 2 μm. The corresponding energy dispersive X-ray analyses (Fig. 4.4c) confirmed that the frustule replicas were composed largely of silicon and carbon, along with some oxygen, which was believed to have formed by oxidation in air. XRD analyses (Fig. 4.5b) confirmed that the final product contained SiC. Scherrer analyses yielded an average crystallite size of 10 nm. A dark-field transmission electron image of a cross-section is shown in Fig. 4.6. The nanocrystallite structure of the converted silicon carbide frustule replica is evident in Fig. 4.6. Electron diffraction analysis of this specimen (the inset in Fig. 4.6) yielded the diffraction spots consistent with the only silicon carbide phase, which was in agreement with the X-ray diffraction analysis (Fig. 4.5b). The thermal stability of the SiC frustule replicas was also studied by thermogravimetric analysis (TGA). Fig 4.7 shows the TGA curve of SiC frustule replicas that were heated at 10 °C/min to 650˚C and held for 2 hours in air. The 2.0 wt% weight loss was attributed to the combustion of un-reacted carbon. From this value, the molar ratio of carbon to silicon in the silicon carbide frustule replicas by this gas deposition method was calculated to be 1.07:1.00.

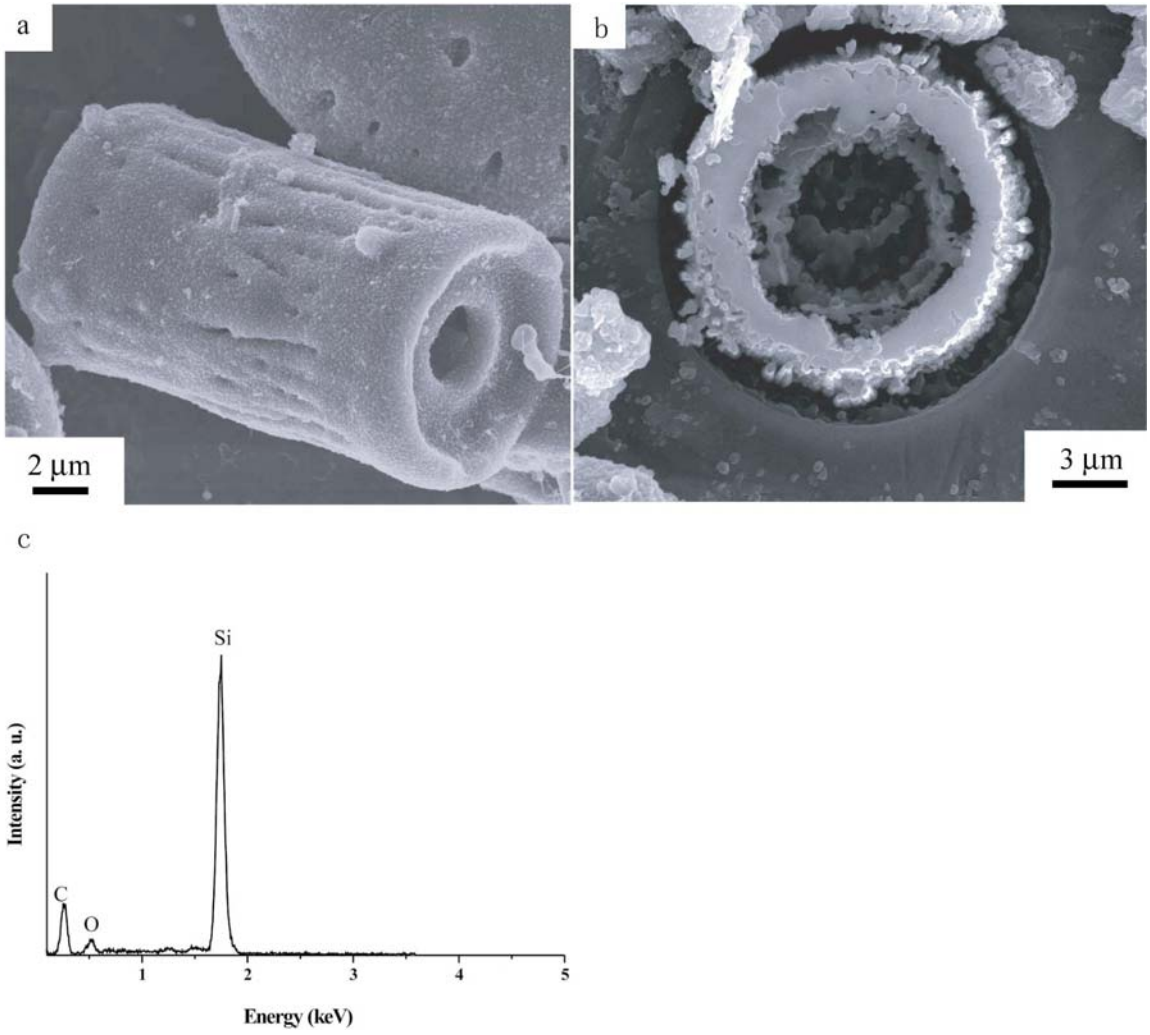

Figure 4.4: a, Secondary electron image of a silicon carbide frustule replica generated by the gas deposition method. b, Secondary electron image of an ion beam milled cross-section of a silicon carbide replica. c, Energy dispersive X-ray analysis obtained from a silicon carbide replica of the type shown in a.

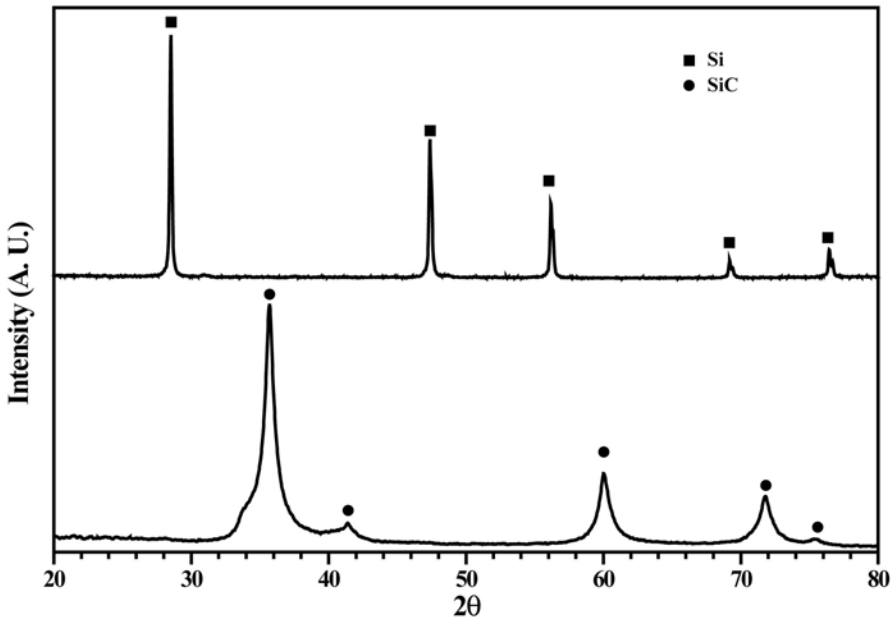

Figure 4.5: a, XRD pattern of the porous silicon frustule replicas that were synthesized from magnesiothermic reaction at 900 ºC/1.5 h and etching in 1 M HCl solution for 4 hours. b, XRD pattern of silicon carbide frustule replicas generated by the gas deposition method.

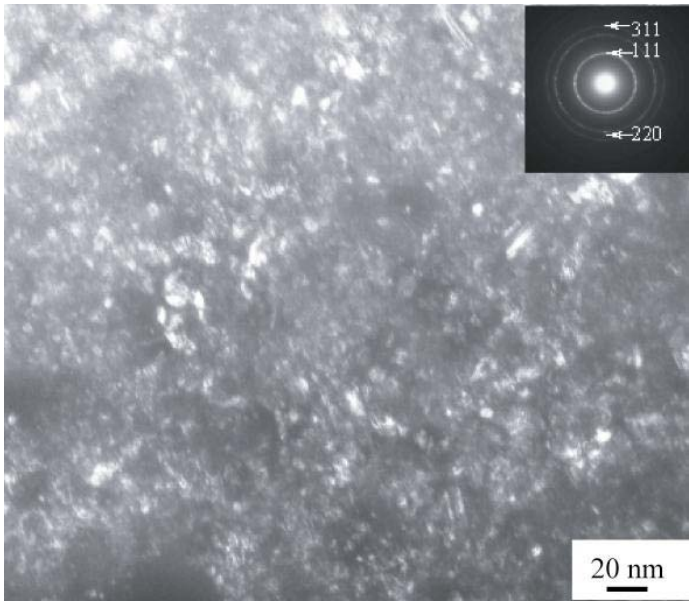

Figure 4.6: Dark field transmission electron image of an ion milled cross-section from a silicon carbide replica generated by the gas deposition method. The electron diffraction pattern is shown in the inset.

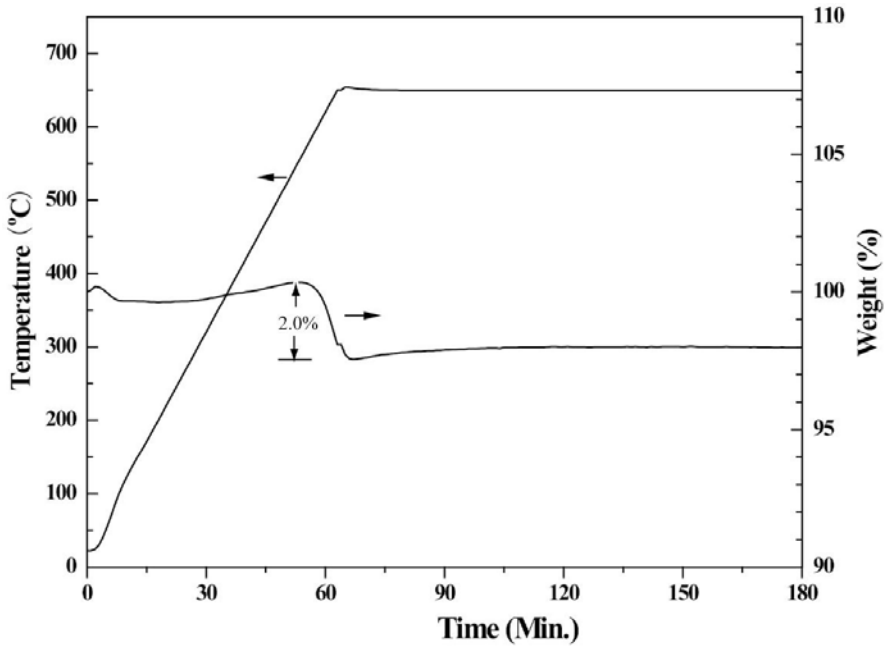

Figure 4.7: Thermogravimetric analysis of the silicon carbide diatom frustule replicas in air. The silicon carbide sample was held in an alumina crucible with 8-mm outside diameter and 6-mm inside diameter, forming ~5-mm deep powder bed.

4.3 Discussion

Considering that the reaction was incomplete via the liquid coating method. Only the silicon carbide frustules synthesized through the gas deposition method will be discussed here. Though the pyrolysis of methane is a very complex process[88], carbon and hydrogen are the major products under a pressure of 20-500 mm Hg in the temperature range of 800 ˚C to 1000 ˚C[89], which was also confirmed from the thermodynamic calculations. Fig. 4.8 shows the gas composition under different temperatures at 1 atmosphere with a starting material of 1 mole CH_4. Fig. 4.8 indicates that it is possible for methane to decompose at temperatures as low as 800 ^{o}C. Fig. 4.9 shows the weight gain of a silicon sample (900 ºC/1.5h) in 10% CH_4/90% Ar at ≤950 ºC (heating rate: 10 °C/min).

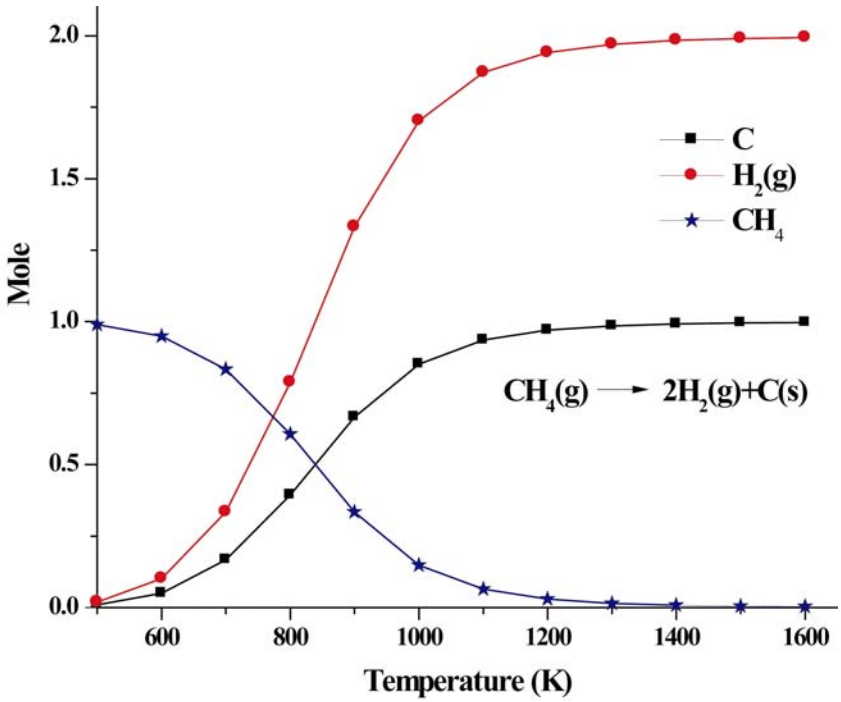

Figure 4.8: Thermodynamic equilibrium compositions for the system $CH_4(g) \rightarrow C(s) + 2H_2(g)$ (the starting material: 1 mole CH_4, calculation based on the data [90])

The silicon frustule replicas exhibited significant weight gain commencing at around 880 ºC, which indicated that carbon was being deposited on the silicon sample. The basic apparent reactions involved in the formation of the SiC diatom replicas are given as follows:

$CH_4(g) \rightarrow C(s) + 2H_2(g)$ (4.1)

$C(s) + Si(s) \rightarrow SiC(s)$ (4.2)

Reaction (4.1) is the pyrolysis of methane at ≥ 880 °C. The carbon was coated on the silicon diatom replica through the apparent chemical vapor deposition reaction. The

deposited carbon reacted with silicon to form silicon carbide, following the reaction (4.2). Because the latter reaction was conducted at 1200 ^{o}C, well below (melting point of the silicon 1410 ^{o}C), the shapes and nano-features were still well retained.

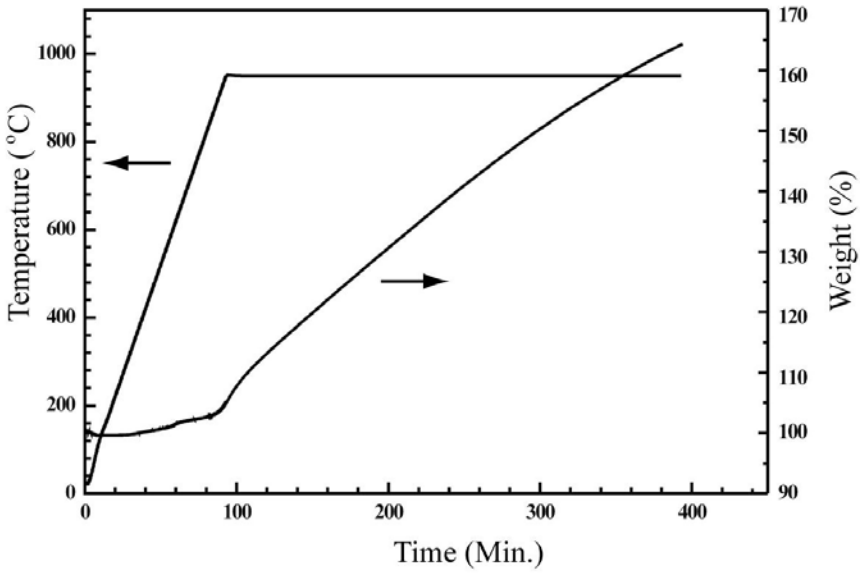

Figure 4.9: Thermogravimetric analysis of a silicon frustule replica (900 ºC/1.5 h) sample in 10% CH_4/90% Ar flowing at 20 ml/min. The silicon sample was held in an alumina crucible with 8-mm outside diameter and 6-mm inside diameter, forming ~5-mm deep powder bed.

4.4 Summary

Silica-based diatom frustules were first converted into the porous silicon frustules replicas via magnesiothermic reaction (900 ºC/1.5 h). Thermodynamic analyses indicated that methane could pyrolyze at a temperature as low as 800 ˚C. Carbon was successfully deposited on the surface of porous silicon frustule replicas via pyrolysis of methane at 950 ˚C. Carbon could also be deposited on the surface of porous silicon frustule replicas by coating them with resin and subsequent pyrolysis of the coated resion. The deposited carbon reacted with silicon to form silicon carbide at 1200 ˚C. The silicon carbide replicas retained the 3-D shapes and features of the original diatom frustules.

CHAPTER 5: POROUS CARBON CONVERSION

Porous carbon materials are utilized or are under active development for catalysis[91-93], fuel cells[94], and hydrogen storage applications[95]. Traditional methods for producing porous carbon via pyrolysis of precursors, such as coconut shells, phenolic resins and textile fibers, do not allow for precise control of the pore size distribution (PSD) over a wide size range[96, 97]. Template techniques have been used to synthesize mesoporous carbon with controllable pores in the range of 2 to 4 nm[93]. Recently, carbide-derived carbons (CDCs) generated from a chlorine reaction have attracted attention because such CDCs exhibit unique characteristics such as narrow pore size distribution (1~2 nm), high open pore volume (~80%), large specific surface area (up to ~2000 m^2/g), and moderate synthesis cost[95]. Chlorine reacts selectively with the silicon in silicon carbide by the reaction:

$$SiC(s)+2Cl_2(g)\rightarrow SiCl_4(g)+C(s) \qquad (5.1)$$

so as to convert the SiC into porous carbon[98]. Other carbides such as titanium carbide, boron carbide, and zirconium carbide have also been converted into porous carbon by such a chlorine reaction[95, 99].

5.1 Kinetics of the chlorine reaction process

The kinetics of the chlorine reaction process were studied to determine the minimum time needed for completing the carbon formation process. Previous studies on the kinetics of the reaction (5.1) were not self-consistent, due to different experimental configurations[100, 101]. In addition, the reaction kinetics for product layer thicknesses less than 3 μm have

not yet been studied. The wall thicknesses of diatom frustules (A*ulacoseira*) tend to fall in this <3 μm range. In this work the kinetic mechanism for the conversion of SiC plates into C via chlorine reaction will first be explained. The use of this reaction to convert SiC diatom replicas into carbon replicas will then be described.

5.1.1 Fundamental kinetic analyses of the reaction of chlorine with silicon carbide

When a Cl_2/Ar gas mixture passes over a flat silicon carbide plate, a laminar flow of gas will be established (Fig. 5.1) for flow rates (*i. e.,* for Reynolds numbers less than 2000[102]). The Reynolds number is defined as[103]:

$$\mathrm{Re} = \frac{\rho \upsilon}{\mu} L \tag{5.2}$$

where ρ is the gas density, υ is the gas velocity, μ is the gas viscosity and L is a characteristic length. The thickness of the momentum boundary layer for the laminar flow[104] can be described by:

$$\delta = 4.6\left(\frac{\nu L}{\upsilon_\infty}\right)^{1/2} \tag{5.3}$$

$$\nu = \frac{\mu}{\rho} \tag{5.4}$$

where L is the horizontal distance from the leading edge of the plate and, υ_∞ is the bulk velocity of gas. When the diffusion boundary layer is assumed to be thinner than the momentum boundary layer, the thickness of the diffusion boundary layer is given by[105]:

$$\delta_c = Sc^{-(1/3)}\delta \tag{5.5}$$

where Sc is the Schmidt number, defined as ν / D, where D is the diffusion coefficient of the relevant gas species. The shrinking core model[106] may be used to describe the kinetic behavior of the chlorine reaction process on the silicon carbide plate. There are three potential rate-limiting steps to be considered: i) mass transport through a diffusion boundary layer in the gas phase, ii) chemical reaction at the carbon/silicon carbide interface, and iii) diffusion through the carbon product layer.

If mass transport through a gaseous boundary layer is rate determining, then the reaction rate should be proportional to the mass flux through the boundary layer as described by Fick's first law:

$$J = -D(\frac{\partial c}{\partial y})\Big|_{y=0} \tag{5.6}$$

where c is the chlorine gas concentration in the boundary layer, and y is the vertical distance from the horizontal silicon carbide surface. From Fig. 5.2, and equation (5.3) and (5.5), the following equation was deduced.

$$(\frac{\partial c}{\partial y})_{y=0} = 0.217(c_\infty - c_0)(\upsilon_\infty / \nu L)^{1/2}(Sc)^{1/3} \tag{5.7}$$

where c_∞ is the bulk gas concentration, and c_0 is the gas concentration at the sample surface.

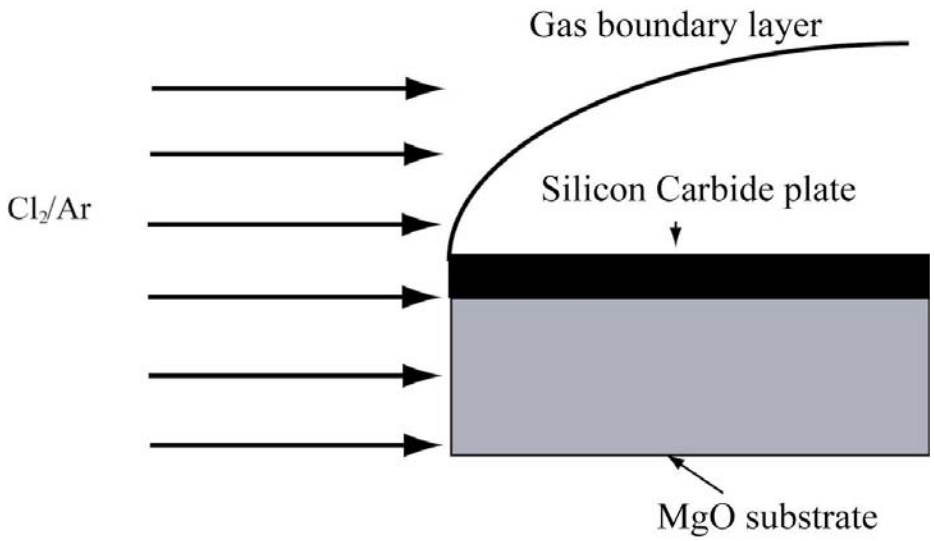

Figure 5.1: Illustration of gas boundary layer, which is developed when a laminar gas flows over a flat plate.

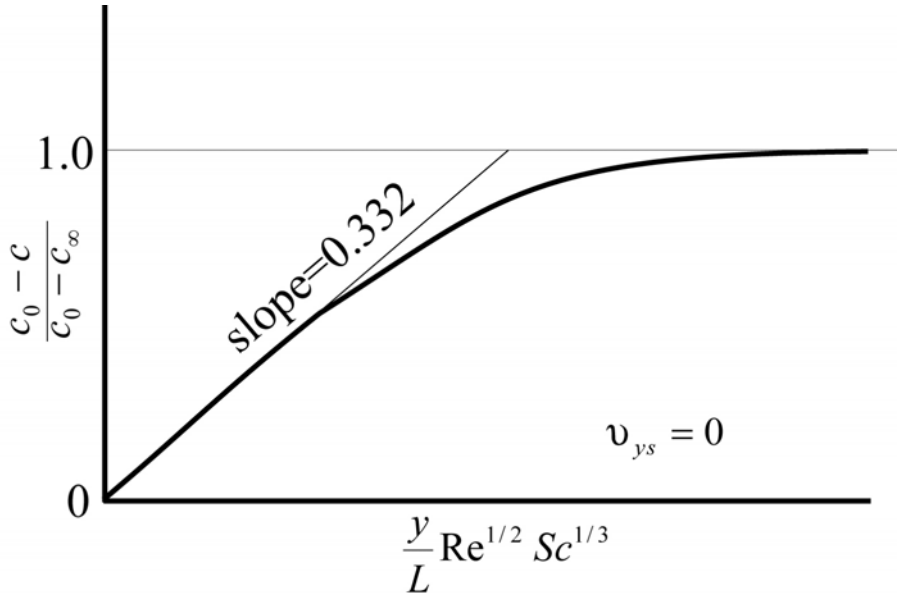

Figure 5.2: Concentration variation for laminar flow over a flat plate[105].

Combining the equations (5.6) and (5.7) yields:

$$J = -0.217D(C_\infty - C_0)(\upsilon_\infty / \nu L)^{1/2}(Sc)^{1/3} \tag{5.8}$$

The corresponding silicon carbide consumption rate with time may then be described by

$$X = 0.217DV_m(C_\infty - C_0)(\upsilon_\infty / \nu L)^{1/2}(Sc)^{1/3}t \tag{5.9}$$

This equation, for diffusion control through a gas boundary layer, indicates that the extent of conversion should vary linearly with time and bulk gas concentration, parabolically with bulk gas velocity, and inverse parabolically with the distance from the leading edge.

If a chemical reaction at the planar silicon carbide/carbon interface is the rate-controlling step for the chlorine reaction process, then the extent of the reaction should follow the following kinetic law[106]:

$$X = k(C_\infty)^n V_m t \tag{5.10}$$

where k is the reaction constant, C_∞ is the concentration of the reactant gas in the surrounding atmosphere and V_m is the molar volume of silicon carbide. Under chemical reaction control, the extent of the reaction is linear with time, and should not depend on distance from the leading edge or on the bulk gas flow rate.

If the diffusion through the carbon product layer is the rate-controlling step, then the extent of reaction is described by[106]:

$$X = z\sqrt{2K_P t} \tag{5.11}$$

where K_P is the parabolic rate constant and z is the molar volume ratio of the solid carbide reactant to the carbon product layer. If diffusion through the product layer is the rate-limiting step, then the extent of reaction should follow a parabolic law with time. The reaction should also be independent of the bulk gas flow rate.

5.1.2 Experimental methods for chlorine reaction kinetics

Solid CVD grown β phase SiC wafers (Valley Design Corp., CA, USA) were used in the present research. The surface roughness value (the height of the irregularities), density, and resistivity of the silicon carbide wafer were 50 Å, 3.21 g/cm^3 (~100% theoretical density) and 10000 Ω·cm, respectively. The wafers were 11/16" long, 3/16" wide and 0.016-0.017" thick. A given silicon carbide was mounted flat on a MgO substrate. The MgO substrate with the SiC wafer was then put in a 1.0-inch diameter quartz tube furnace. The quartz tube was purged with Ar (99.999% purity) for 2 hours at room temperature, and then heated to an intended temperature, at which a 97.5%Ar/2.5%Cl_2 gas mixture was passed through for a fixed time at a flow rate of 500 sccm. The gas was then switched to pure argon and the furnace was cooled to room temperature. The treated sample was removed from the furnace and fractured. To make sure that the Ar/Cl_2 flow as laminar, Reynolds numbers (Appendix D) under different conditions were calculated. These numbers were well below 2000. A computer simulation was also used to model a momentum boundary layer (Appendix D). This simulation indicated that there was velocity variation within at least 0.5 mm from the leading edge of the silicon carbide plate.

5.1.3 Experimental results for chlorine reaction kinetics

The fracture surface was examined with a secondary electron microscope equipped with a backscattered electron detector. Fig. 5.3 reveals SEM and backscattered electron images from a representative fracture section. The product thickness measured from SEM image and backscattering image were 587±11 nm and 603±12 nm, respectively (10 measurements for each data point). Fig. 5.4 shows the SEM images of the fracture section near the leading edge from the specimen treated at 900 °C for 1 hour. The thickness of carbon layer from the chlorine reaction process did not significantly change with distance from the leading edge (Figure 5.5).

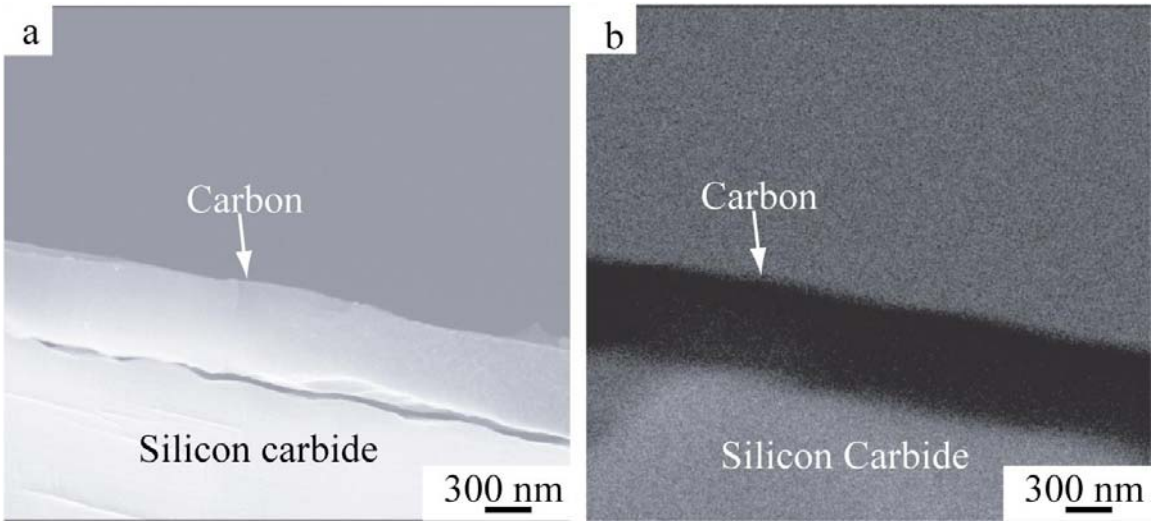

Figure 5.3: a, SEM image and b, Backscattered electron image of a fracture section of a silicon carbide specimen exposed at 900 ºC for 30 minutes to a 97.5% Ar/2.5% Cl_2 mixture with a flow rate of 500 sccm.

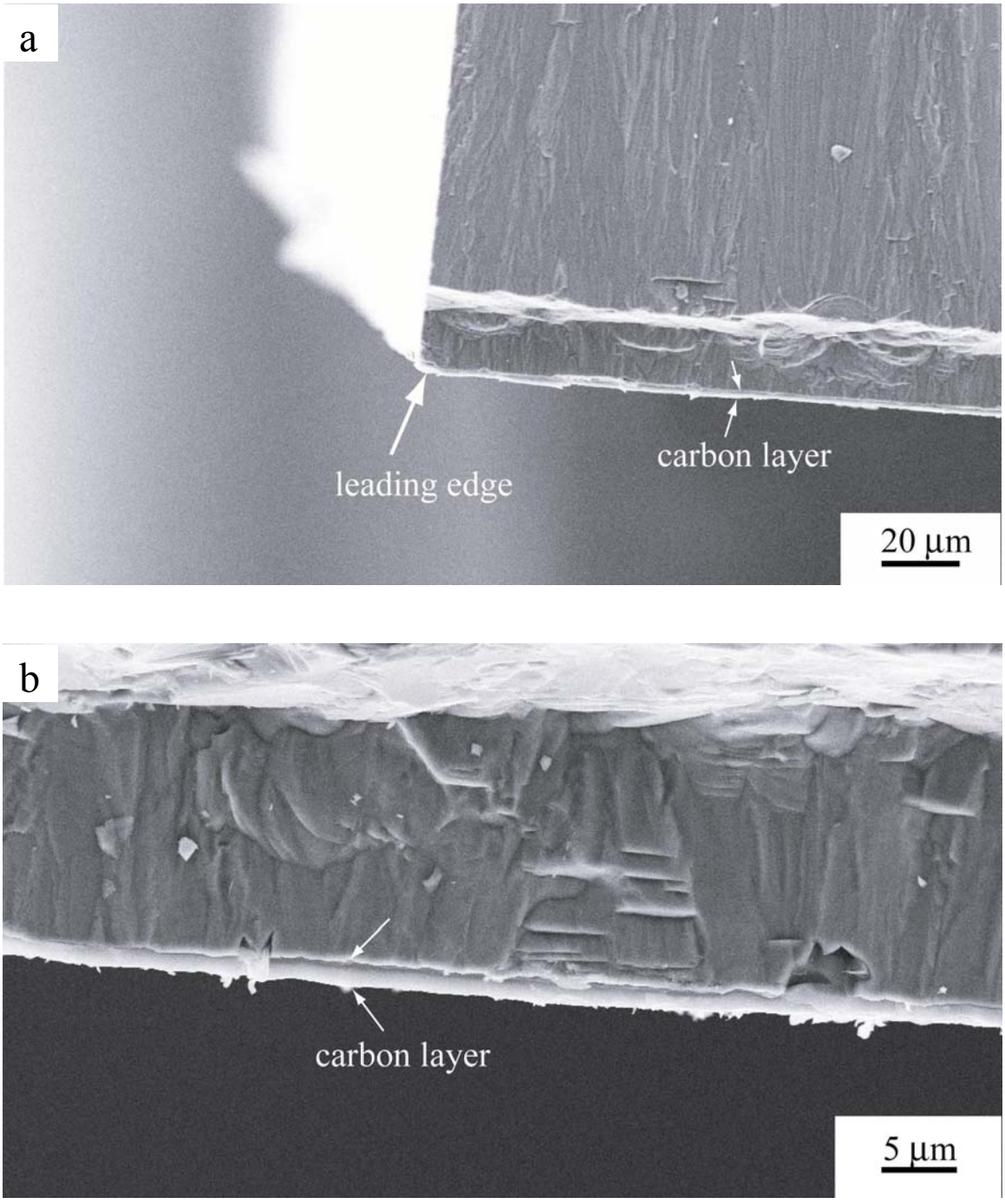

Figure 5.4: SEM image of a fracture section from a silicon carbide specimen exposed at 900 ˚C for 1 h to a 97.5%Ar/2.5%Cl_2 gas mixture at a flow rate of 500 sccm. a, low magnification. b, high magnification.

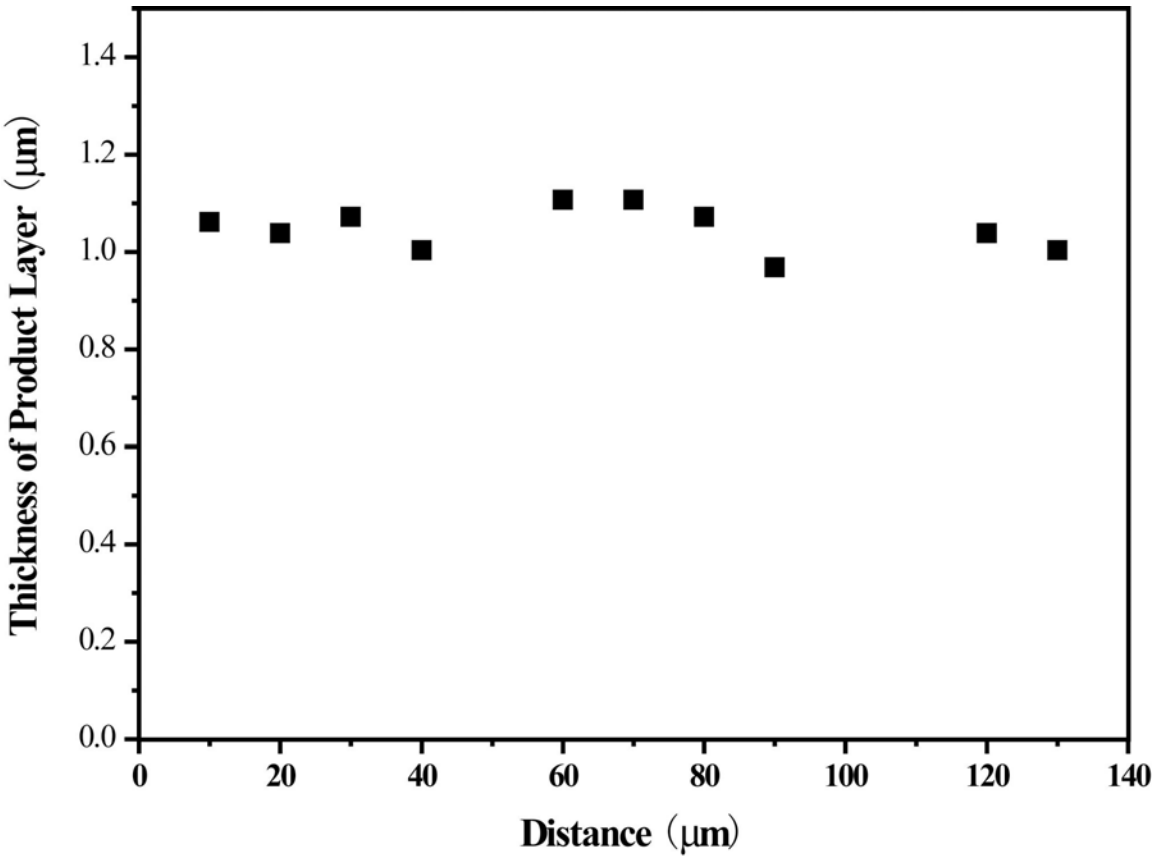

Figure 5.5: Thickness versus the distance for the leading edge of a silicon carbide plate exposed at 900 ˚C for 1 h to a 97.5%Ar/2.5%Cl_2 gas mixture at a flow rate of 500 sccm.

The carrier-gas flow rate was also varied in the range of 250 to 750 sccm , but there was no significant change in the thickness of product layer with the same reaction time (Table 5.1). These two observations indicated that gas transport through a gas boundary layer wasn't rate controlling the overall the chlorine reaction process process. The carbon product thickness was measured at 10 different locations for each sample. The average thickness values were then plotted as a function of reaction time.

Table 5.1: Carbon product layer thickness at different flow rates at 850 ºC for 3 h in 97.5%Ar/2.5%Cl_2

Flow rates (sccm)	250	500	750
Thickness (nm)	789±18	772±13	796±12

Fig. 5.6 shows the change of in the thickness of carbon layers versus reaction time, upon exposure to 97.5%Ar/2.5%Cl_2 gas at 800˚C, 850˚C and 900˚C at 500 sccm, respectively. For all three reaction temperatures, the thickness of the product carbon layer increased linearly with reaction time, as per the following equation.

$$d = kt \tag{5.12}$$

where d is thickness of the product layer, k is the linear rate constant and t is time. With the least squares fitting, the rate constant, k, were determined to be 0.056, 0.257 and 1.176 μm/h for 800 ˚C, 850 ˚C and 900 ˚C, respectively. The R^2 parameters were 0.9942, 0.9995 and 0.9980, for 800˚C, 850˚C and 900˚C respectively. The linear rate constant at different temperatures could be fitted to an Arrhenius type equation:

$$k = k_0 e^{-E_a / RT} \tag{5.13}$$

where E_a is the activation energy, k_0 is a constant, and T is temperature The logarithm of linear rate constant is plotted against inverse temperature in Fig. 5.7. From the plot, the activation energy is calculated to be 318 kJ/mole.

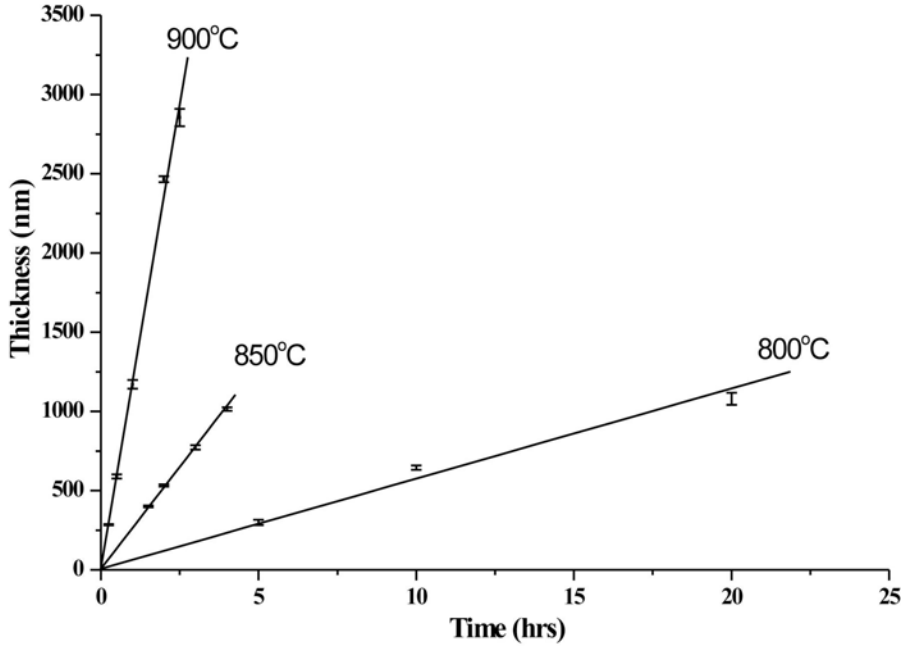

Figure 5.6: Time versus the thickness of product carbon layers grew in 97.5%Ar-2.5%Cl_2 at 800˚C, 850˚C and 900˚C at 500 sccm.

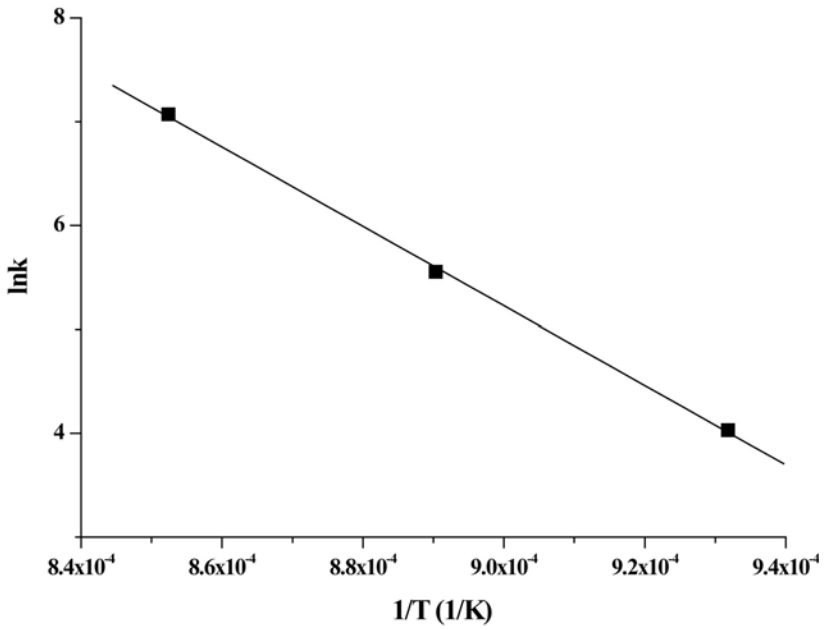

Figure 5.7: The logarithm of linear rate constant versus inverse temperature.

Above kinetic data were used to estimate the minimum reaction time to convert silicon carbide replicas into carbon sample. The wall thickness of the silicon carbide *Aulacoseira* replicas was around 2 μm. At 900 ºC, when a silicon carbide frustule replica was exposed to 97.5% Ar/2.5% Cl_2 at 500 sccm, the chlorine reaction process should complete within one hour, which was confirmed by the absence of silicon peak from energy dispersive X-ray analyses of the reaction product (Fig. 5.8). Later, 30 min. also was found to be sufficient for completing the chlorine reaction process on the SiC *Aulacoseira* replicas, which may be due to the porous structure of SiC *Aulacoseira* replicas.

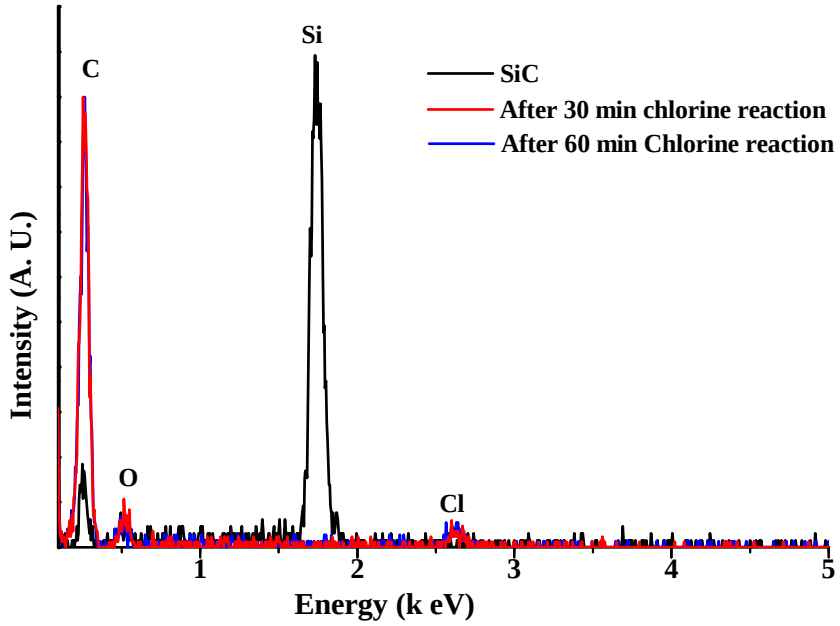

Figure 5.8: Energy dispersive X-ray analyses of silicon carbide *Aulacoseira* frustule replicas and the samples generated by exposing SiC replicas to 97.5% Ar/2.5% Cl_2 at 500 sccm at 900 ºC for 30 min. and 60 min., respectively (Chlorine peak was from the adsorbed chlorine gas in carbon product).

5.1.4 Conclusions on kinetics of the chlorine reaction process

The chlorine reaction process followed linear kinetics in the temperature range of 800-900 ºC at a rate of 500 sccm with the product thickness of less than 3 μm. The extent of reaction was independent of the gas flow rate (from 250 sccm to 700 sccm) and did not depend on the distance from the leading edge. These results suggest that the rate of the chlorine reaction process was controlled by a chemical reaction at the interface between the product layer and the un-reacted silicon carbide. McNallan *et. al.,* studied the kinetics of the chlorine reaction with SiC in the product layer thickness range from 20 μm to 350 μm (at 900 ºC to 1100 ºC)[101]. They reported that the chlorine reaction with SiC followed a parabolic rate law in this range. From their conclusion and our current results, the kinetic mechanism of the chlorine reaction process appears to shift from an initial linear reaction-controlled process into a parabolic diffusion-controlled process when the product layer increased from <3 to >20 μm.

5.2 Synthesis and characterization of porous carbon diatom frustules replicas

A variety of materials have been examined as templates to fabricate hierarchical pore structures[93, 107]. Diatomaceous earth is an extremely abundant and inexpensive template materials. Researchers have used diatomaceous earth templates to synthesize macroporous/microporous and macroporous/mesoporous materials[108, 109]. In the current research, a chlorine reaction process has been used to introduce the micro-porosity into SiC-converted diatom frustules to yield carbon replicas hierarchical macro/meso/microporous structures. The silicon carbide frustules replicas were synthesized using the gas deposition process, described in the previous chapter. The silicon carbide frustule replicas were placed in a quartz tube. Pure chlorine gas was

passed through the tube at 950 ºC for 0.5-3.0 hours at 30 sccm. After cooling, the reacted sample was removed from the furnace for further examination. Shape preservation of the frustule products was examined with the secondary electron microscopy. Fig. 5.9a-c reveals images of the product frustules after the chlorine reaction process for 3.0 h. Fig. 5.9a and Fig. 5.9b reveal secondary electron images of carbon frustule replicas using *Aulacoseira* frustules as the starting templates. Fig. 5.9c reveals a secondary image of carbon frustules replicas generated from a *Cyclotella Costei* frustule. The frustule products retained the shapes and fine features of the parent diatom frustules. The energy dispersive X-ray pattern (Fig. 5.9d) indicated that the product frustule was comprised of carbon. A small chlorine peak, from adsorbed chlorine gas, was also detected. A transmission electron image (by Dr. Ye Cai) of a cross-section of an *Aulacoseira* carbon frustule replica is shown in Fig. 5.10a. A corresponding selected area electron diffraction (SAED) pattern is shown in Fig. 5.10b. The absence of diffraction spots in the SAED pattern was consistent with amorphous carbon.

N_2 adsorption/desorption curves of the carbon frustules replicas are shown in Fig. 5.11a. These curves exhibit typical type IV adsorption curve consistent with significant mesoporosity. As a comparison, the adsorption/desoprtion curves (Fig. 5.11b) of porous carbon powder generated from the solid silicon carbide powder (Alfa Aesar, MA, USA) exhibit type I behavior, which is consistent with only nanoscale porosity. Based on the curve in Fig. 5.11a, the BET specific surface area of the carbon frustule replicas was calculated to be 1368.6 m^2/g, while the unconverted diatom frustules have only a surface area of only 1.6 m^2/g. The surface area increased by a factor 830 through the entire conversion process. The pore size distribution (PSD) and pore volume were determined

using the non-local density functional theory (NLDFT) method provided in Quantachrome's data reduction software[110]. Fig. 5.11c reveals the pore size distribution of the carbon frustule replicas. The micropore (pore <2 nm) volume was 0.386 cm^3/g, whereas the mesopore volume (pore size< 36nm) was 1.354 cm^3/g.

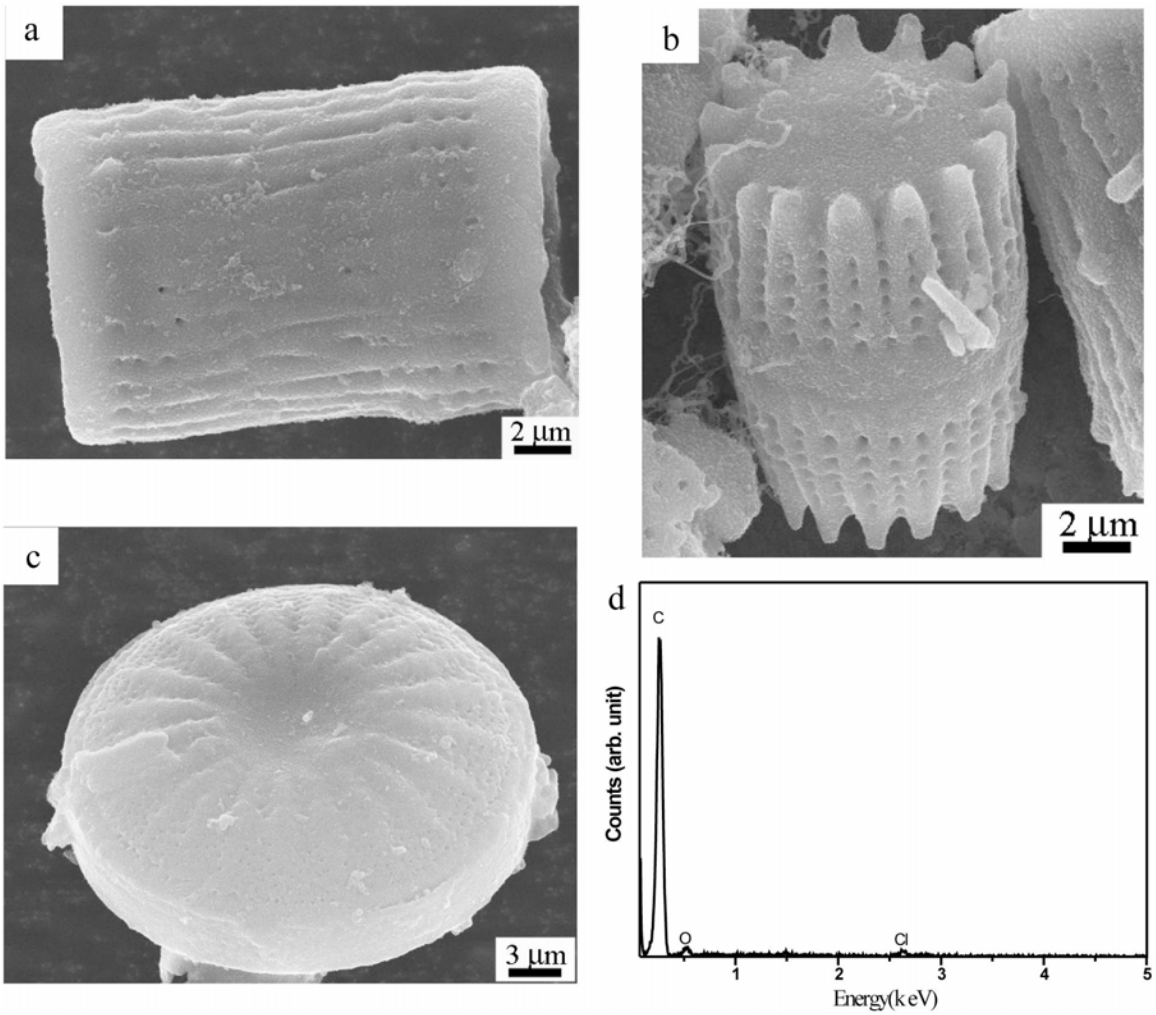

Figure 5.9: a and b, SEM images of carbon replicas of *Aulacoseira* frustules generated by the reaction of Cl_2 (g) with SiC replicas at 950 ºC for 3.0 h. c, SEM image of a carbon replica of a *Cyclotella Costei* frustule. d, Energy dispersive X-ray analysis obtained from carbon diatom frustules replicas of *Aulacoseira* frustules generated by the reaction of Cl_2(g) with SiC replicas at 950 ºC for 3.0 h.

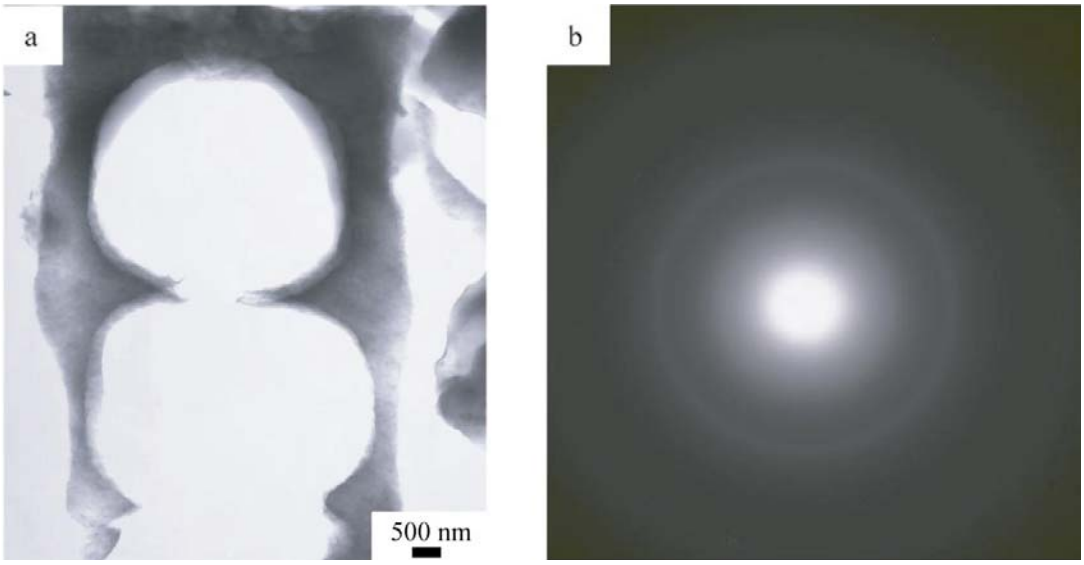

Figure 5.10: a, Low magnification bright field transmission image of an ion milled cross section of an *Aulacoseira* carbon frustule replica. b, Selected area electron pattern obtained from the carbon frustule replica generated by exposing a SiC replica to Cl_2(g) at 30 sccm at 950 ºC for 3.0 h, shown in a (Provided by Dr. Ye Cai).

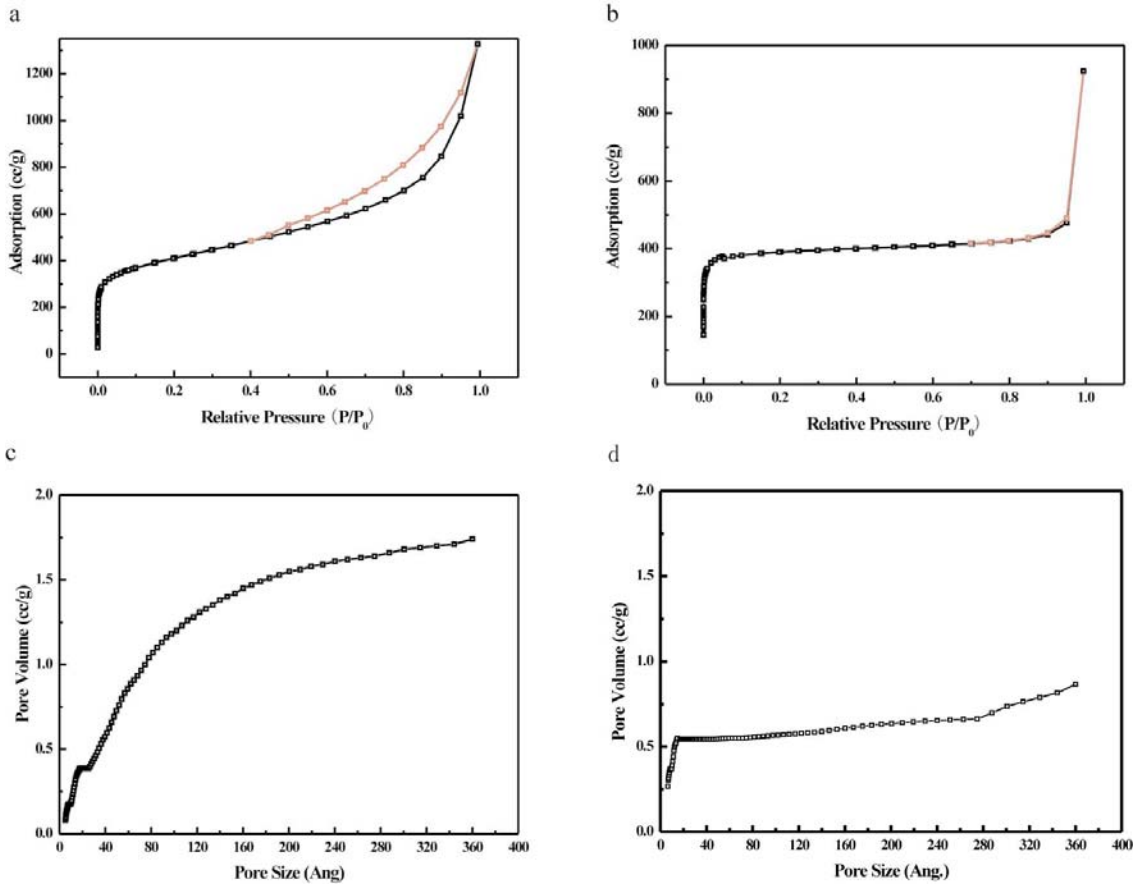

Figure 5.11: a, Nitrogen isothermal adsorption/desorption curves of the carbon frustule replicas (generated from SiC *Aulacoseira* frustule replicas by exposure to flowing Cl_2 (g) at 950 ºC for 3.0 h), revealing the presence of mesopores. b, Nitrogen isothermal adsorption/desorption curves of the nanoporous carbon generated from the conventional SiC powder. c, Pore size distribution of the carbon frustules replicas. d, Pore size distribution of the nanoporous carbon generated from the conventional SiC powder, revealing a predominance of micropores. (Patial work was conducted by Eric Ernst).

5.3 Applications of porous carbon frustule replicas

5.3.1 Porous carbon frustule replicas as hydrogen storage material

Previous studies have demonstrated that porous carbon structures with very fine pores (1 nm or below) were particularly efficient for hydrogen sorption[95, 111]. However, the chlorine reaction process for converting SiC powder into porous carbon used by other authors involved a high temperature (1100-1200 ºC) and treatment for a prolonged time (3 hours). According to the previous EDS analyses, 30 minutes was sufficient for completing the chlorine reaction process on SiC *Aulacoseira* replicas at a temperature ≥ 900 ºC. The hydrogen sorption of these nanoporous carbon frustule replicas synthesized at 950 ºC is revealed in. Fig. 5.12. The carbon replicas could store up to 2.3 wt% H_2 at 77 K. There was a little difference in the hydrogen sorption behavior between the porous carbon replicas formed at 950 ºC for 30 minutes and for 3 hours. This was due to small differences in (pore structures) of these two samples. The pore size distribution (PSD) analyses of these specimens are shown in Fig 5.13.

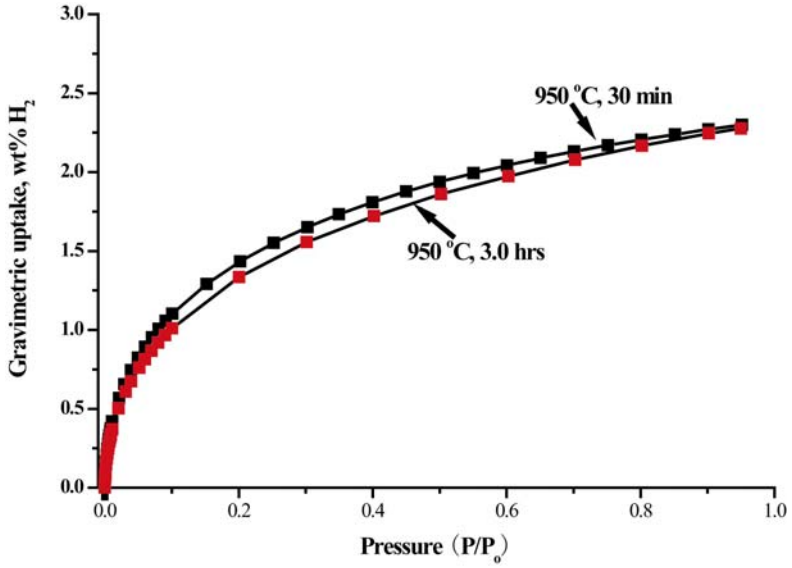

Figure 5.12: Hydrogen sorption isotherms of the carbon frustule replicas generated by the reaction of Cl_2 (g) with SiC *Aulacoseira* frustule replicas at 950 ºC (Provided by Eric Ernst).

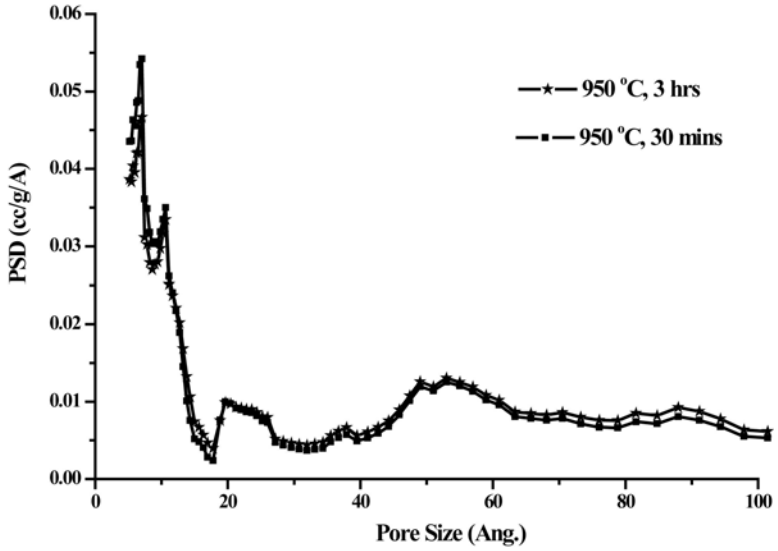

Figure 5.13: Pore size distribution of the carbon frustule replicas generated by the reaction of Cl_2(g) with SiC *Aulacoseira* frustule replicas at 950 ºC (Provided by Eric Ernst).

5.3.2 Porous carbon frustule replicas as catalyst support

It is worthwhile to incorporate metal nanoparticles into the nanopores of frustule replicas and to study their properties because (1) Nanopores limit the size of filled materials, and, thus highly dispersed and very fine metal nanoparticles may be formed within such pores for effective catalysis and (2) Coarsening is prevented by the carbon matrix, so the nanoparticles trapped in the nanopores should be thermally stable even at high temperatures[93, 112]. Because C/Pt composites can exhibit excellent electro-catalytic properties[93, 107], the incorporation of platinum particles into the nanopores of carbon frustule replicas was examined. A chemical vapor deposition method was used to introduce Pt element into the nanopores of the carbon frustule replicas, as described before[113, 114]. Carbon monoxide was passed at 120 sccm over the surface of platinum chloride powder at 220ºC for 30 min., which was separated from the carbon frustule replicas by alumina cloth. Furnace was then shut down (the cooling rate was around 2.5 °C/min in the range of 220-150°C). Platinum dicarbonyl chloride, *cis*-$Pt(CO)_2Cl_2$, formed and then deposited into the nanopores of carbon frustule replicas. The carbonylation of platinum halides occurs as follows[113, 114]

$$PtCl_2 + 2CO \rightarrow Pt(CO)_2Cl_2 \uparrow \qquad \text{(at 210 ºC)} \qquad (5.14)$$

$$2PtCl_2 + 4CO \rightarrow Pt_2(CO)_4Cl_4 \uparrow \qquad \text{(at 220 ºC)} \qquad (5.15)$$

After the deposition of platinum dicarbonyl chloride, the sample was washed with de-ionized water, dried at 110 ºC overnight and reduced in pure hydrogen flowing at 120 sccm for one hour at 300 ºC. Fig. 5.14a reveals a secondary electron image of a carbon frustule replica after such platinum deposition. The Pt deposition did not appear to alter

the overall morphology of the carbon frustule replica. EDX analysis (Fig. 5.14b) confirmed the successful deposition of Pt into or onto the carbon frustule replicas. To further confirm that Pt was successfully loaded within the fine pores of the carbon frustule replicas, TEM analyses (by Dr. Ye Cai) were conducted on an ion-milled section of a carbon frustule replica loaded with platinum. Fig. 5.15a-c reveals the bright field transmission electron images of an ion-milled section cross-section. The Pt particles were distributed throughout the entire cross-section. Higher magnification images such as Fig 5.15c, revealed Pt particles with a bimodal size distribution. One particle range was from 10 to 20 nm and the other range was from 1 to 3 nm. This distribution was consistent with the pore size distribution analysis, which showed the coexistence of mesopores and micropores in the carbon frustule replicas (Fig. 5.11a,c). These pores were now occupied by platinum nanoparticles incorporated by gas deposition. The inset in Fig. 5.15c reveals the lattice fringes of a very fine particle. The lattice fringe spacing was 0.226 nm, which was the reported spacing of (111) planes of for platinum[115]. The selected area electron diffraction pattern (Fig. 5.15d) from the ion-milled cross-section yielded diffraction spots was consistent with platinum (note: the carbon was amorphous).

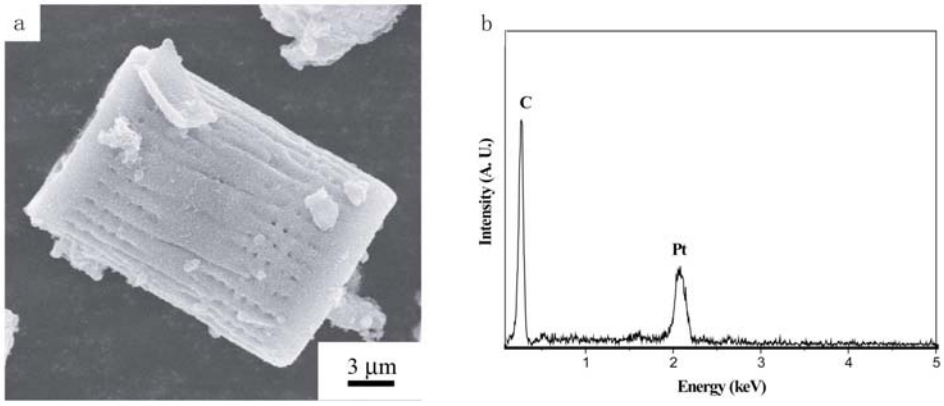

Figure 5.14: a, SEM image of a carbon frustule replica loaded with Pt nanoparticles. b, EDS analysis of the carbon frustule replica shown in a.

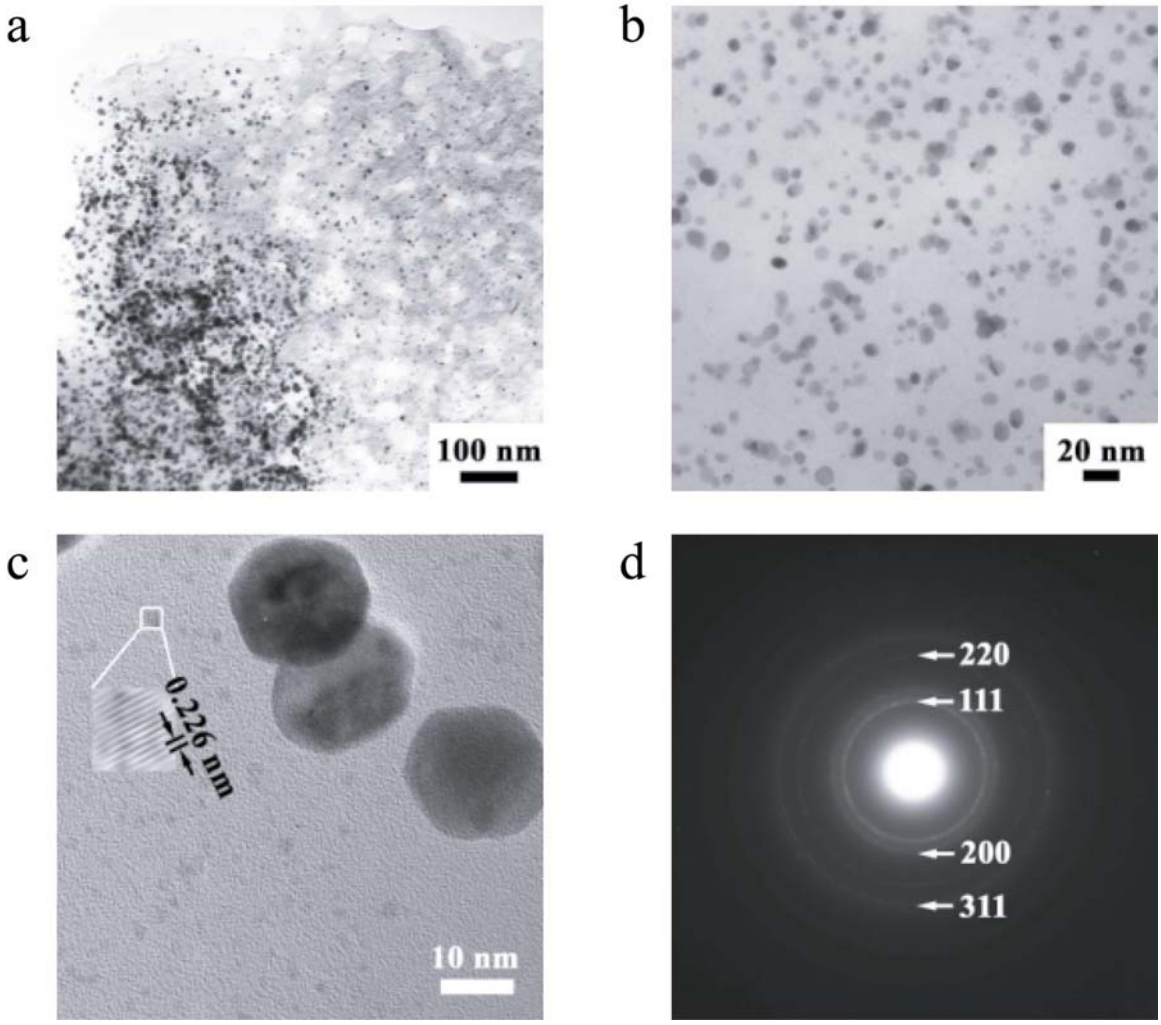

Figure 5.15: a, b and c, Low magnification, medium and high magnification bright field transmission electron images, respectively, of an ion-milled cross-section of a carbon frustule replica after platinum incorporation. The inset in c shows a high-resolution transmission electron image of a very fine platinum nanocrystal. d, Selected area electron pattern obtained from the carbon frustule replica loaded with platinum nanocrystals (Provided by Dr. Ye Cai).

The results described above indicated that platinum nanocrystallites had been successfully loaded into the carbon frustule replicas. To ensure that deposited platinum did not inhibit gas access into the fine pores in the carbon frustule replicas, BET analysis was conducted on the carbon frustule replicas loaded with Pt. The specific surface area of the Pt-loaded carbon frustule replicas was 1001 m^2/g, which was still is quite large. TG analysis (Fig. 5.16) was conducted to quantify the platinum loading. The analysis was conducted in air from room temperature to 1000 ºC at a heating rate of 5K/min. From Fig. 5.16, the Pt loading was found to be 44.7 wt%. Because various noble metal elements (*e. g.*, Au, Pt, Pd, Rh and Ir) are available in the form of carbonyl complexes[114], these metals may also be loaded into the porous carbon frustule replicas by the method described above.

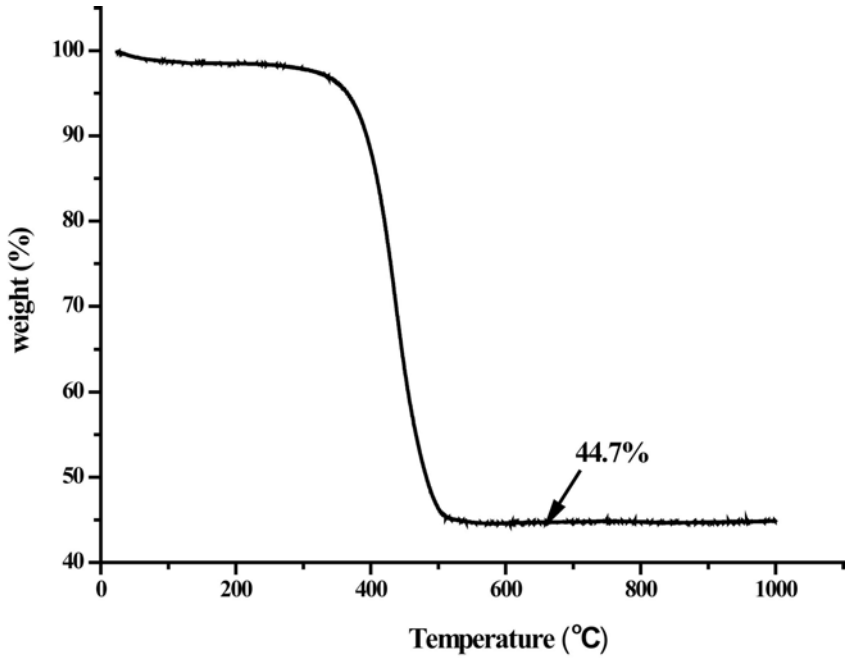

Figure 5.16: TG analysis of carbon frustules replica loaded with Pt. The analysis was conducted in air with a heating rate of 5K/min.

5.4 Summary

The kinetics of chlorine reaction with silicon carbide process was studied under conditions yielding porous carbon product layers less than 3 μm in thickness. The kinetic data was consistent with a chemical reaction between the product carbon layer and the unreacted silicon carbon as the rate-limiting step. The linear reaction rate constants in 97.5%Ar/2.5%Cl_2 were 0.056, 0.257 and 1.176 μm/h at 800˚C, 850˚C and 900˚C, respectively. The activation energy of the reaction process was 318 kJ/mole. Carbon frustule replicas with well-retained morphologies have been synthesized from the silicon carbide frustule replicas through this chlorine reaction process. The resulting carbon frustule replicas possessed a BET specific surface area as high as 1386.6 m^2/g and a pore size distribution spanning the macro, meso and micropore ranges. Such hierarchical pore size distributions may facilitate diffusion into the carbon frustule replicas. Using a chemical vapor deposition method, a high loading (44.7%) of platinum nanoparticles have been successfully deposited into the nanopores of carbon frustule replicas.

CHAPTER 6: CONCLUSIONS

Diatoms possess characteristics such as abundance, diversity, and high reproductivity, which make their nano-structured frustules (diatom frustules) attractive for a wide range of applications. To overcome the limitation of their silica based frustule composition, diatom frustules have been converted into a variety of materials including silicon, silicon carbide, silver, gold, palladium and carbon in the present study. The compositions and the extent of shape preservation of the replicas are examined and evaluated with different characterization methods such as X-ray diffraction, SEM, TEM and FTIR analyses. These replicas still retained the complex 3D structures and nano-scaled features of the starting diatom frustules. Some properties and possible applications of converted materials are explored and the kinetics and thermodynamics related to the successful replications (conversions) are also studied and discussed:

(1) A low temperature (650 ºC) magnesiothermic reaction was used to convert three dimensional 3-D nano-structured diatom frustules into microporous nanocrystalline silicon replicas. These silicon replicas possessed a very high surface area (>500 m^2/g) and a large population of micropores (≤2 nm). The oxidized silicon frustule replicas exhibited photoluminescence under UV light. A microsensor fabricated from such a silicon frustule replica exhibited rapid (≤25 s) and sensitive nitric oxide gas detection (1 p.p.m.) with very low applied biased voltage (100 mV). This suggested a possible application in microscale gas sensing. The magnesium vapor partial pressure was the key parameter in controlling the products from the magnesiothermic reaction. Magnesium silicide

is suggested as the source of magnesium gas to avoid the formation of a magnesium silicide product during the magnesiothermic reaction.

(2) Metallic frustule replicas (e.g., Ag, Au, Pd) were obtained by immersing the microporous nanocrystalline silicon replicas in electroless plating solutions. Silicon carbide frustule replicas were synthesized with two steps. In the first step, the silicon frustule replicas were coated with carbon, either by resin coating or by pyrolysis of methane at 950 ºC. The coated carbon reacted with the silicon at 1200 ºC to form the silicon carbide frustule replicas.

(3) A chlorine reaction process was used to convert the silicon carbide frustule replicas into carbon frustule replicas. This process also introduced micropores into the frustule replicas and, thus, the carbon frustules replicas possessed pores with sizes in various scales, which is important for catalysis. The carbon frustule replicas possessed high surface areas (*e.g.,* 1368 m^2/g) and micropore volumes (*e.g.,* 0.386 cm^3/g). Using a gas deposition method, Pt nanoparticles were successfully loaded into the nanopores of carbon frutule replicas, for possible catalytic application of carbon frustule replicas. The kinetics of the chlorine reaction process were also studied. Because the thickness of the formed carbon layer changed linearly with the reaction time but not the location, the rate-limiting step for the chlorine reaction process was found to be the reaction at the interface between the product carbon layer and the unreacted silicon carbide layer. The minimum time required for complete silicon removal from a silicon carbide frustule replica was also estimated, on the basis of the kinetic data from planar silicon carbide specimens.

Considering the frustule diversity of extant diatom species and ongoing research to develop genetically-modified diatom frustules, diatoms (frustules) with precisely-controlled structures may be fabricated or cultured in the not-too-distant future. These structures may be converted into desired non-oxide compositions for specific applications through the synthetic chemical methods demonstrated in this dissertation. The control over 3-D microscale shape, nanoscale features, and chemistry afforded by such a process combining biology and synthetic chemistry should open the door to a wide variety of low-cost, high-performance electronic, optical, and chemical devices.

APPENDIX A: SI REPLICAS OF *MELOSIRA NUMMULOIDES* DIATOM FRUSTULES

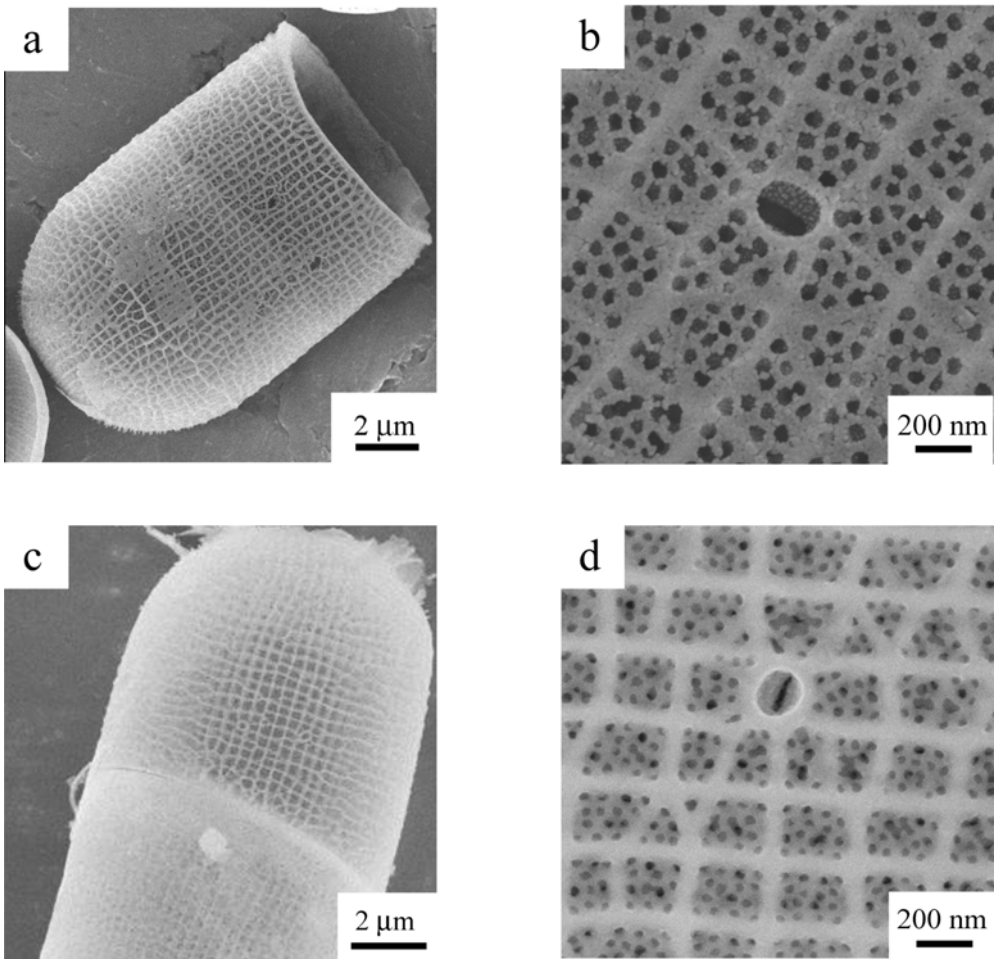

Figure A.1: Secondary electron images of a, b, *Melosira nummuloides* diatom frustules (SiO_2). c,d, Si replicas of *Melosira nummuloides* frustules produced by reaction with Mg(g) at 650 °C for 2.5 h (to yield MgO/Si composites) and then selective dissolution of the MgO. (Published in *Nature*, 446, 172- 174, 2007.)

APPENDIX B: POROUS SILICON MICROGEAR

Using a magnesiothermic reaction at 850 °C for 2.5 hrs, along with etching in a 1 M hydrochloric acid aqueous solution for 4 hrs, the porous silicon microgear (shown in Fig. B1) was synthesized from a silica microgear template provided by J. A. Lewis, *et al.,* University of Illinois.

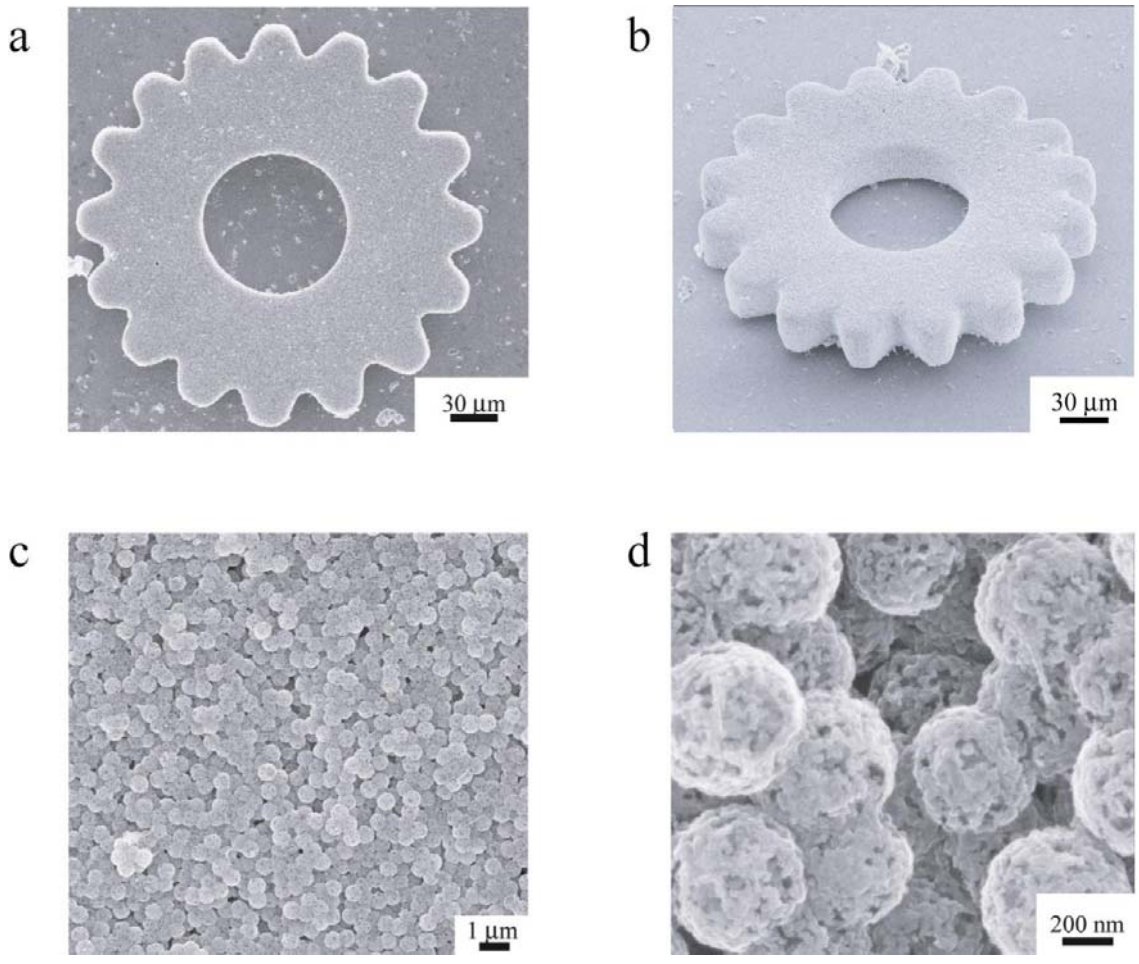

Figure B.1: Secondary electron image of a porous silicon microgear. b, Secondary electron image for the microgear shown in a, after 45° tilt. c and d, High magnification secondary electron images of the microgear shown in a.

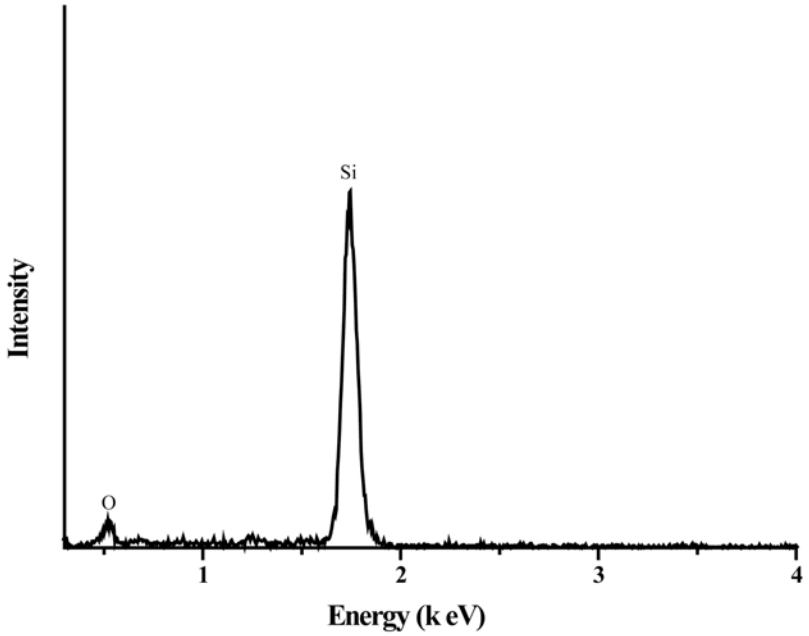

Figure B.2: Energy dispersive X-ray analysis obtained from the porous silicon microgear.

APPENDIX C: CALIBRATION STANDARD FOR SEM MEASUREMENTS

Polystyrene spheres (ASTM certified, Electron Microscopy Sciences Company, PA) prepared under a gravity-free condition with a mean size of 9.89 microns (±0.9% standard deviation) were used as SEM calibration standard. Fig. C.1 shows the SEM image of polystyrene spheres used as the calibration standard. The average size, measured from 20 randomly selected spheres with the secondary electrons microscopy in the present work, was 9.92±0.05 microns.

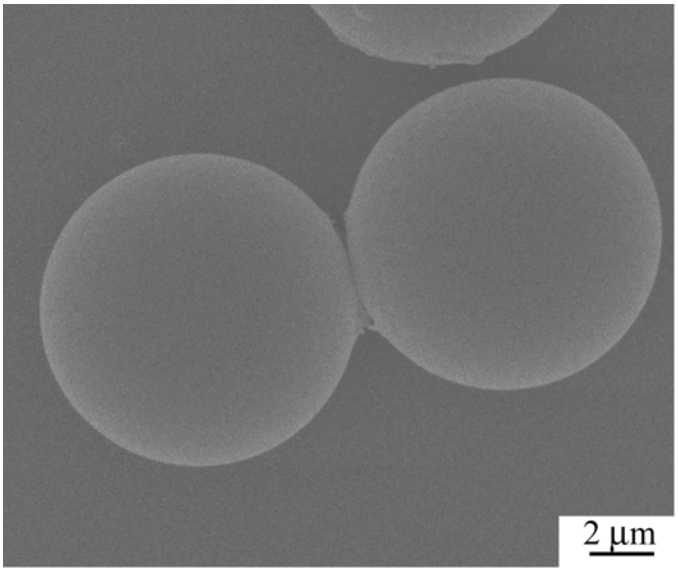

Figure C.1: Secondary electron image of polystyrene spheres used as the calibration standard.

APPENDIX D: CALCULATION OF REYNOLDS NUMBERS AND SIMULATION OF MOMENTUM FIELD

The Reynolds number is defined as[105]:

$$\mathrm{Re} = \frac{L\upsilon\rho}{\mu} \tag{D.1}$$

where υ is gas velocity, L is the distance from the leading edge or the diameter of the tube, ρ is gas density and μ is gas viscosity. The viscosity of a gas can be calculated by Equation (C.2)[116]:

$$\mu = 2.67\times10^{-5}\frac{\sqrt{MT}}{\sigma^2\Omega^{(2,2)*}} \tag{D.2}$$

where σ is the collision diameter, T is absolute temperature, $\Omega^{(2,2)*}$ is the collision integral for viscosity and thermal conductivity. σ values for Ar and Cl_2 are 3.418 Å and 4.115 Å, respectively. $\Omega^{(2,2)*}$ values are tabulated in the reference[117].

For a gas mixture, the viscosity can be described as[116]:

$$\mu_{mix} = \frac{\sum X_i\mu_i(M_i)^{1/2}}{\sum X_i(M_i)^{1/2}} \tag{D.3}$$

where X_i is mole fraction of component, μ_i is the viscosity of component i and M_i is molecular weight of component i. Based on the above equations together with the ideal gas equation, Reynolds numbers for a 500 sccm flow rate at different temperatures are calculated and summarized in Table D.1.

Table D.1: Reynolds numbers under different temperatures and related parameters for 97.5% Ar/2.5% Cl_2 mixture.

T (ºC)	$\Omega^{(2,2)*}_{Ar}$	$\Omega^{(2,2)*}_{Cl2}$	υ (cm/s)	ρ_{mix} (g/cm^3)	μ_{mix} (g/cm/sec)	Re_L	Re_D
800	0.8433	1.030	6.51	4.96E-4	5.56E-4	3.13	16.69
850	0.8371	1.026	6.78	4.74E-4	5.73E-4	2.72	14.18
900	0.8315	1.015	7.09	4.54E-4	5.90E-4	2.59	13.80

The software (Comsol 3.2a) was used to simulate the momentum field of the incompressible Newtonian flow inside the furnace tube by solving Navier-Stokes equation:

$$\rho(\frac{\partial \hat{\upsilon}}{\partial t} + \hat{\upsilon}\cdot\nabla\hat{\upsilon}) = \mu\nabla^2\hat{\upsilon} \qquad (D.4)$$

where ρ is the gas density, $\hat{\upsilon}$ is the velocity vector of gas and μ is the gas viscosity. The gas and flow parameters from our experiments used in the simulation are listed in Table D.2. Fig. D.1 and Fig. D.2 show the velocity field distribution from the simulation. Within 0.5 mm from the leading edge , the thickness of boundary layer still follows the parabolic law with the distance from the leading edge.

Table D.2: Parameters used for the simulation of the momentum field.

Temperature (K)	Viscosity (kg/m/s)	Density (kg/m^3)	Flow rate (sccm)
1173	5.56E-5	0.496	500

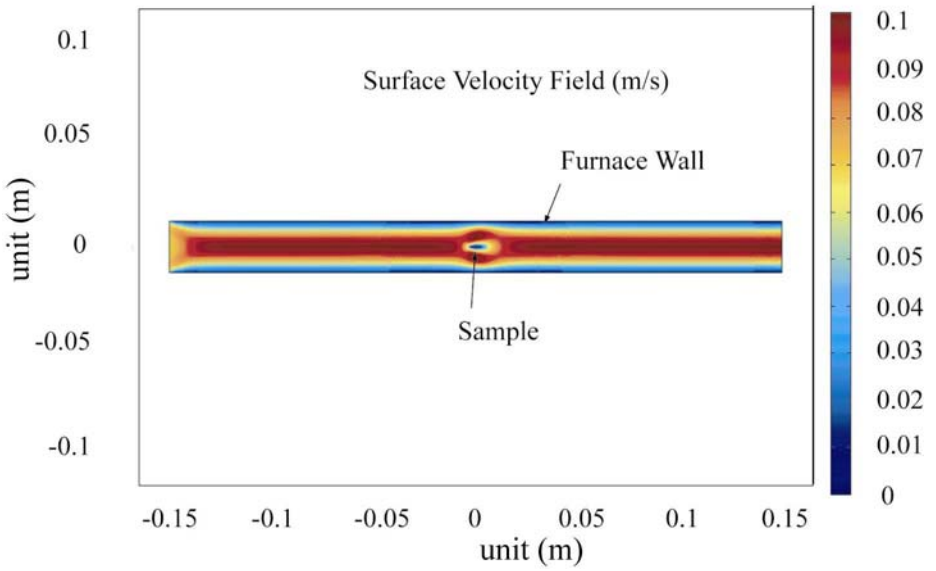

Figure D.1: Calculated velocity field distribution inside the furnace tube.

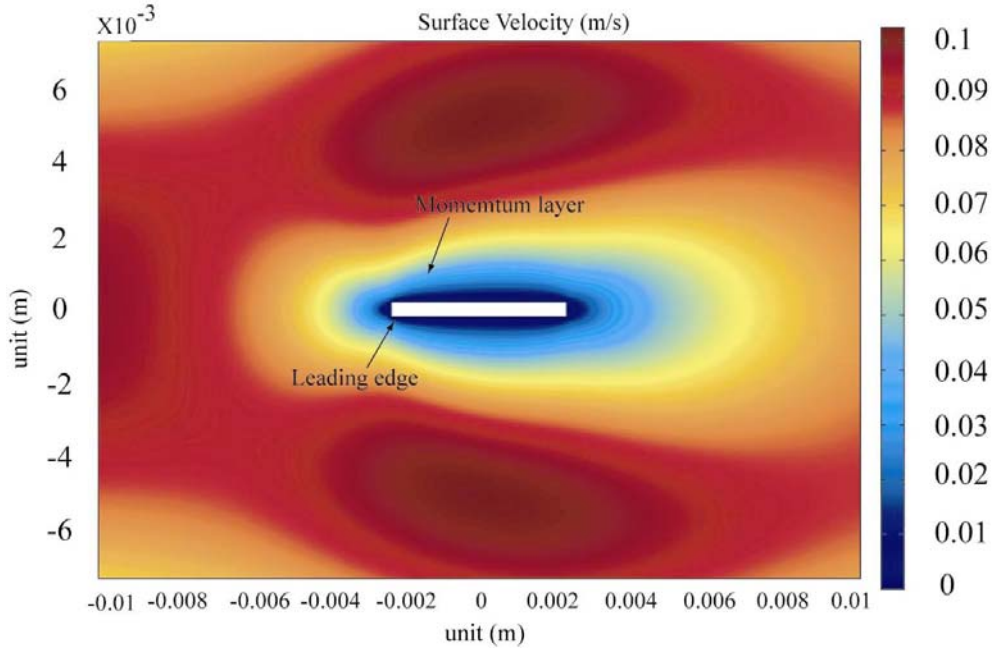

Figure D.2: Calculated velocity field distribution around the sample

REFERENCES

1. Aizenberg, J.; Tkachenko, A.; Weiner, S.; Addadi, L.; Hendler, G. *Nature* **2001,** 412, (6849), 819-822.

2. Ghiradella, H. *Applied Optics* **1991,** 30, (24), 3492-3500.

3. Aksay, I. A.; Trau, M.; Manne, S.; Honma, I.; Yao, N.; Zhou, L.; Fenter, P.; Eisenberger, P. M.; Gruner, S. M. *Science* **1996,** 273, (5277), 892-898.

4. Mann, D. G. *Phycologia* **1999,** 38, (6), 437-495.

5. Round, F. E.; Crawford, R. M.; Mann, D. G., *The Diatoms: biology & morphology of the genera*. Cambridge University Press: 1990.

6. Werner, D., *The Biology of Diatoms*. University of California Press: 1977.

7. Hildebrand, M.; York, E.; Kelz, J. I.; Davis, A. K.; Frigeri, L. G.; Allison, D. P.; Doktycz, M. J. *Journal of Materials Research* **2006,** 21, (10), 2689-2698.

8. Parkinson, J.; Gordon, R. *Trends in Biotechnology* **1999,** 17, (5), 190-196.

9. Lewin, J. C.; Guillard, R. R. *Annual Review of Microbiology* **1963,** 17, 373-414.

10. Miron, A. S.; Gomez, A. C.; Camacho, F. G.; Grima, E. M.; Chisti, Y. *Journal of Biotechnology* **1999,** 70, (1-3), 249-270.

11. Dolley, T. P.; Moyle, P. R., *History and Overview of the U.S. Diatomite Mining Industry, with Emphasis on the Western United States*. U.S. Department of the Interior and U.S. Geological Survey: 2003.

12. Losic, D.; Mitchell, J. G.; Voelcker, N. H. *New Journal of Chemistry* **2006,** 30, (6), 908-914.

13. Losic, D.; Mitchell, J. G.; Lal, R.; Voelcker, N. H. *Advanced Functional Materials* **2007,** 17, (14), 2439-2446.

14. De Stefano, L.; De Stefano, M.; Maddalena, P.; Moretti, L.; Rea, I.; Mocella, V.; Rendina, I. *Proceedings of SPIE-The International Society for Optical Engineering* **2007,** 6593, (Photonic Materials, Devices, and Applications II), 659313/1-659313/9.

15. Rorrer, G. L.; Chang, C.-h.; Liu, S.-h.; Jeffryes, C.; Jiao, J.; Hedberg, J. A. *Journal of Nanoscience and Nanotechnology* **2005,** 5, (1), 41-49.

16. Dickerson, M. B.; Sandhage, K. H.; Nalik, R.; Stone, M. O. Methods for fabricating micro-to-nanoscale devices via biologically-induced solid formation on biologically-derived templates, and micro-to-nanoscale structures and micro-to-nanoscale devices made thereby. 2006-358342
2007112548, 20060221., 2007.

17. Sandhage, K. H.; Dickerson, M. B.; Huseman, P. M.; Caranna, M. A.; Clifton, J. D.; Bull, T. A.; Heibel, T. J.; Overton, W. R.; Schoenwaelder, M. E. A. *Advanced Materials (Weinheim, Germany)* **2002,** 14, (6), 429-433.

18. Unocic, R. R.; Zalar, F. M.; Sarosi, P. M.; Cai, Y.; Sandhage, K. H. *Chemical Communications (Cambridge, United Kingdom)* **2004**, (7), 796-797.

19. Shian, S.; Cai, Y.; Weatherspoon, M. R.; Allan, S. M.; Sandhage, K. H. *Journal Of The American Ceramic Society* **2006,** 89, (2), 694-698.

20. Cai, Y.; Sandhage, K. H. *Physica Status Solidi A: Applications and Materials Science* **2005,** 202, (10), R105-R107.

21. Ernst, E. M.; Church, B. C.; Gaddis, C. S.; Snyder, R. L.; Sandhage, K. H. *Journal Of Materials Research* **2007,** 22, (5), 1121-1127.

22. Gaddis, C. S.; Sandhage, K. H. *Journal Of Materials Research* **2004,** 19, (9), 2541-2545.

23. Weatherspoon, M. R.; Allan, S. M.; Hunt, E.; Cai, Y.; Sandhage, K. H. *Chemical Communications* **2005**, (5), 651-653.

24. Zhao, J.; Gaddis, C. S.; Cai, Y.; Sandhage, K. H. *Journal of Materials Research* **2005,** 20, (2), 282-287.

25. Elwenspoek, M.; Jansen, H. V., *Silicon micromachining*. Cambridge University Press: Cambridge, [England]; New York, 1998; Vol. 7, p 405.

26. Blanford, C. F.; Schroden, R. C.; Al-Daous, M.; Stein, A. *Advanced Materials* **2001,** 13, (1), 26.

27. Zhao, D. Y.; Feng, J. L.; Huo, Q. S.; Melosh, N.; Fredrickson, G. H.; Chmelka, B. F.; Stucky, G. D. *Science* **1998,** 279, (5350), 548-552.

28. Gratson, G. M.; Xu, M. J.; Lewis, J. A. *Nature* **2004,** 428, (6981), 386-386.

29. Sailor, M. J.; Lee, E. J. *Advanced Materials* **1997,** 9, (10), 783.

30. Canham, L. T. *Advanced Materials* **1995,** 7, (12), 1033.

31. Seals, L.; Gole, J. L.; Tse, L. A.; Hesketh, P. J. *Journal of Applied Physics* **2002,** 91, (4), 2519-2523.

32. Phamhuu, C.; Delgallo, P.; Peschiera, E.; Ledoux, M. J. *Applied Catalysis A-General* **1995,** 132, (1), 77-96.

33. Nagamori, M.; Malinsky, I.; Claveau, A. *Metallurgical Transactions B-Process Metallurgy* **1986,** 17, (3), 503-514.

34. Yasuda, K.; Nohira, T.; Takahashi, K.; Hagiwara, R.; Ogata, Y. H. *Journal of the Electrochemical Society* **2005,** 152, (12), D232-D237.

35. Nohira, T.; Yasuda, K.; Ito, Y. *Nature Materials* **2003,** 2, (6), 397-401.

36. Yasuda, K.; Nohira, T.; Ogata, Y. H.; Ito, Y. *Journal of the Electrochemical Society* **2005,** 152, (11), D208-D212.

37. Banerjee, H. D.; Sen, S.; Acharya, H. N. *Materials Science and Engineering* **1982,** 52, (2), 173-179.

38. Canham, L. T. *Applied Physics Letters* **1990,** 57, (10), 1046-1048.

39. Ulhir, A. *Bell Syst. Tech. J.* **1956,** 35, 333.

40. Archer, R. J. *Journal of Physics and Chemistry of Solids* **1960,** 14, 104-110.

41. Baratto, C.; Faglia, G.; Sberveglieri, G.; Boarino, L.; Rossi, A. M.; Amato, G. *Thin Solid Films* **2001,** 391, (2), 261-264.

42. Shin, H. C.; Corno, J. A.; Gole, J. L.; Liu, M. L. *Journal of Power Sources* **2005,** 139, (1-2), 314-320.

43. Takahashi, M.; Koshida, N. *Journal of Applied Physics* **1999,** 86, (9), 5274-5278.

44. Lammel, G.; Renaud, P. *Sensors And Actuators A-Physical* **2000,** 85, (1-3), 356-360.

45. Weatherspoon, M. R.; Haluska, M. S.; Cai, Y.; King, J. S.; Summers, C. J.; Snyder, R. L.; Sandhage, K. H. *Journal of the Electrochemical Society* **2006,** 153, (2), H34-H37.

46. Munder, H.; Berger, M. G.; Frohnhoff, S.; Thonissen, M.; Luth, H.; Jeske, M.; Schultze, J. W. *Journal of Luminescence* **1993,** 57, (1-6), 223-226.

47. Guerrero-Lemus, R.; Moreno, J. D.; Martin-Palma, R. J.; Ben-Hander, F.; Martinez-Duart, J. M.; Fierro, J. L. G.; Gomez-Garrido, P. *Thin Solid Films* **1999,** 354, (1-2), 34-37.

48. Sing, K. S. W.; Everett, D. H.; Haul, R. A. W.; Moscou, L.; Pierotti, R. A.; Rouquerol, J.; Siemieniewska, T. *Pure and Applied Chemistry* **1985,** 57, (4), 603-19.

49. Gregg, S. J.; Sing, K. S. W., *Adsorption, Surface Area and Porosity*. Second Edition ed.; Academic Press: 1982.

50. Dumas, P.; Gu, M.; Syrykh, C.; Gimzewski, J. K.; Makarenko, I.; Halimaoui, A.; Salvan, F. *Europhysics Letters* **1993,** 23, (3), 197-202.

51. Zhang, Q.; Bayliss, S. C. *Journal of Applied Physics* **1996,** 79, (3), 1351-1356.

52. Martin, T.; Galarneau, A.; Di Renzo, F.; Fajula, F.; Plee, D. *Angewandte Chemie-International Edition* **2002,** 41, (14), 2590.

53. Fowler, C. E.; Hoog, Y.; Vidal, L.; Lebeau, B. *Chemical Physics Letters* **2004,** 398, (4-6), 414-417.

54. Winter, M.; Besenhard, J. O.; Spahr, M. E.; Novak, P. *Advanced Materials (Weinheim, Germany)* **1998,** 10, (10), 725-763.

55. Boukamp, B. A.; Lesh, G. C.; Huggins, R. A. *Journal of the Electrochemical Society* **1981,** 128, (4), 725-9.

56. Barin, I.; Platzki, G., *Thermochemical Data of Pure Substances*. Wiley-VCH Verlag GmbH: 1995.

57. Haluska, M. S.; Dragomir, I. C.; Sandhage, K. H.; Snyder, R. L. *Powder Diffraction* **2005,** 20, (4), 306-310.

58. Geffken, R.; Miller, E. *Transactions of the Metallurgical Society of AIME* **1968,** 242, (11), 2323-8.

59. Balagurov, L. A.; Leiferov, B. M.; Petrova, E. A.; Orlov, A. F.; Panasenko, E. M. *Journal of Applied Physics* **1996,** 79, (9), 7143-7147.

60. Gelloz, B.; Kojima, A.; Koshida, N. *Applied Physics Letters* **2005,** 87, (3).

61. Gorbach, T. Y.; Rudko, G. Y.; Smertenko, P. S.; Svechnikov, S. V.; Valakh, M. Y.; Bondarenko, V. P.; Dorofeev, A. M. *Semiconductor Science and Technology* **1996,** 11, (4), 601-606.

62. Weng, Y. M.; Fan, Z. N.; Zong, X. F. *Applied Physics Letters* **1993,** 63, (2), 168-170.

63. Mawhinney, D. B.; Glass, J. A.; Yates, J. T. *Journal of Physical Chemistry B* **1997,** 101, (7), 1202-1206.

64. Gole, J. L.; Dixon, D. A. *Journal of Physical Chemistry B* **1997,** 101, (41), 8098-8102.

65. Ookubo, N.; Matsuda, Y.; Ochiai, Y.; Kuroda, N. *Materials Science & Engineering, B: Solid-State Materials for Advanced Technology* **1993,** B20, (3), 324-7.

66. Theiss, W., *Structural and Optical Properties of Porous Silicon Nanostuctures*. Gordon & Breach: 1997.

67. Zielasek, V.; Juergens, B.; Schulz, C.; Biener, J.; Biener, M. M.; Hamza, A. V.; Baumer, M. *Angewandte Chemie, International Edition* **2006,** 45, (48), 8241-8244.

68. Iizuka, Y.; Kawamoto, A.; Akita, K.; Date, M.; Tsubota, S.; Okumura, M.; Haruta, M. *Catalysis Letters* **2004,** 97, (3-4), 203-208.

69. Van Noort, D.; Mandenius, C.-F. *Biosensors & Bioelectronics* **2000,** 15, (3-4), 203-209.

70. Padilla, A. P.; Rodriguez, J. A.; Saitua, H. A. *Desalination* **1997,** 114, (3), 203-208.

71. Hieda, M.; Garcia, R.; Dixon, M.; Daniel, T.; Allara, D.; Chan, M. H. W. *Applied Physics Letters* **2004,** 84, (4), 628-630.

72. Erlebacher, J.; Aziz, M. J.; Karma, A.; Dimitrov, N.; Sieradzki, K. *Nature* **2001,** 410, (6827), 450-453.

73. Walsh, D.; Arcelli, L.; Ikoma, T.; Tanaka, J.; Mann, S. *Nature Materials* **2003,** 2, (6), 386.

74. Zhang, H. F.; Hussain, I.; Brust, M.; Cooper, A. I. *Advanced Materials* **2004,** 16, (1), 27.

75. Meldrum, F. C.; Seshadri, R. *Chemical Communications* **2000**, (1), 29-30.

76. Payne, E. K.; Rosi, N. L.; Xue, C.; Mirkin, C. A. *Angewandte Chemie, International Edition* **2005,** 44, (32), 5064-5067.

77. Harraz, F. A.; Tsuboi, T.; Sasano, J.; Sakka, T.; Ogata, Y. H. *Journal of the Electrochemical Society* **2002,** 149, (9), C456-C463.

78. Morinaga, H.; Suyama, M.; Ohmi, T. *Journal of the Electrochemical Society* **1994,** 141, (10), 2834-2841.

79. Bao, Z.; Weatherspoon, M. R.; Shian, S.; Cai, Y.; Graham, P. D.; Allan, S. M.; Ahmad, G.; Dickerson, M. B.; Church, B. C.; Kang, Z.; Abernathy, H. W., III; Summers, C. J.; Liu, M.; Sandhage, K. H. *Nature (London, United Kingdom)* **2007,** 446, (7132), 172-175.

80. Schlesinger, M.; Paunovic, M., *Modern Electroplating*. 4th ed.; Wiley: Toronto, 2000.

81. Tsuboi, T.; Sakka, T.; Ogata, Y. H. *Journal of Applied Physics* **1998,** 83, (8), 4501-4506.

82. Weitzel, C. E.; Palmour, J. W.; Carter, C. H.; Moore, K.; Nordquist, K. J.; Allen, S.; Thero, C.; Bhatnagar, M. *Ieee Transactions on Electron Devices* **1996,** 43, (10), 1732-1741.

83. Sarro, P. M. *Sensors and Actuators a-Physical* **2000,** 82, (1-3), 210-218.

84. Mimura, H.; Matsumoto, T.; Kanemitsu, Y. *Applied Physics Letters* **1994,** 65, (26), 3350-3352.

85. Mynbaeva, M.; Saddow, S. E.; Melnychuk, G.; Nikitina, I.; Scheglov, M.; Sitnikova, A.; Kuznetsov, N.; Mynbaev, K.; Dmitriev, V. *Applied Physics Letters* **2001,** 78, (1), 117-119.

86. Filsinger, D. H.; Bourrie, D. B. *Journal Of The American Ceramic Society* **1990,** 73, (6), 1726-1732.

87. Klinger, N.; Strauss, E. L.; Komarek, K. L. *Journal Of The American Ceramic Society* **1966,** 49, (7), 369.

88. Legrand, J. C.; Diamy, A. M.; Hrach, R.; Hrachova, V. *Vacuum* **1999,** 52, (1-2), 27-32.

89. Lucas, P.; Marchand, A. *Carbon* **1990,** 28, (1), 207-219.

90. Barin, I.; Platzki, G., *Thermochemical Data of Pure Substances*. 3rd ed.; Wiley-VCH Verlag GmbH: 1995; p 1885.

91. Lee, J. J.; Han, S.; Kim, H.; Koh, J. H.; Hyeon, T.; Moon, S. H. *Catalysis Today* **2003,** 86, (1-4), 141-149.

92. Rodriguez, N. M.; Chambers, A.; Baker, R. T. K. *Langmuir* **1995,** 11, (10), 3862-3866.

93. Joo, S. H.; Choi, S. J.; Oh, I.; Kwak, J.; Liu, Z.; Terasaki, O.; Ryoo, R. *Nature* **2001,** 412, (6843), 169-172.

94. Chmiola, J.; Yushin, G.; Gogotsi, Y.; Portet, C.; Simon, P.; Taberna, P. L. *Science* **2006,** 313, (5794), 1760-1763.

95. Gogotsi, Y.; Dash, R. K.; Yushin, G.; Yildirim, T.; Laudisio, G.; Fischer, J. E. *Journal of the American Chemical Society* **2005,** 127, (46), 16006-16007.

96. Beguin, F.; Frackowiak, *Nanomaterials Handbook*. CRC press: Boca Raton FL, 2006.

97. Williams, P. T.; Reed, A. R. *Journal Of Analytical And Applied Pyrolysis* **2004,** 71, (2), 971-986.

98. Gogotsi, Y.; Welz, S.; Ersoy, D. A.; McNallan, M. J. *Nature* **2001,** 411, (6835), 283-287.

99. Chmiola, J.; Yushin, G.; Dash, R.; Gogotsi, Y. *Journal of Power Sources* **2006,** 158, (1), 765-772.

100. Gogotsi, Y. G.; Kailer, A.; Nickel, K. G. *Materials Research Innovations* **1997,** 1, (1), 3-9.

101. Lee, A.; Zhu, R. Y.; McNallan, M. *Journal of Physics-Condensed Matter* **2006,** 18, (32), S1763-S1770.

102. Leys, M. R.; Veenvliet, H. *Journal Of Crystal Growth* **1981,** 55, (1), 145-153.

103. Rott, N. *Annual Review Of Fluid Mechanics* **1990,** 22, 1-11.

104. Church, S. W., *Viscous Flow: The Practical Use of Theory (Fluid Flow)*. Butterworth-Heinemann: 1988.

105. Kou, S., *Transport phenomena and materials processing*. Wiley: New York, 1996.

106. Levenspiel, O., *Chemical reaction engineering*. Third ed.; Wiley: New York, 1999.

107. Tian, N.; Zhou, Z.-Y.; Sun, S.-G.; Ding, Y.; Wang, Z. L. *Science (Washington, DC, United States)* **2007,** 316, (5825), 732-735.

108. Anderson, M. W.; Holmes, S. M.; Hanif, N.; Cundy, C. S. *Angewandte Chemie, International Edition* **2000,** 39, (15), 2707-2710.

109. Cai, X.; Zhu, G.; Zhang, W.; Zhao, H.; Wang, C.; Qiu, S.; Wei, Y. *European Journal of Inorganic Chemistry* **2006**, (18), 3641-3645.

110. Ravikovitch, P. I.; Neimark, A. V. *Colloids And Surfaces A-Physicochemical And Engineering Aspects* **2001,** 187, 11-21.

111. Dash, R.; Chmiola, J.; Yushin, G.; Gogotsi, Y.; Laudisio, G.; Singer, J.; Fischer, J.; Kucheyev, S. *Carbon* **2006,** 44, (12), 2489-2497.

112. Fedosyuk, V. M.; Danishevskii, A. M.; Kurdyukov, D. A.; Shuman, V. B.; Gordeev, S. K. *Physics of the Solid State* **2003,** 45, (9), 1750-1753.

113. Woo, S. I.; Kim, D. K.; Park, Y. K.; Kim, M. R.; Decyk, P. *Catalysis Letters* **2003,** 85, (1-2), 69-72.

114. Browning, J.; Goggin, P. L.; Goodfellow, R. J.; Norton, M. G.; Rattray, A. J. M.; Taylor, B. F.; Mink, J. *Journal of the Chemical Society-Dalton Transactions* **1977**, (20), 2061-2067.

115. *Powder Diffraction File Card No. 01-087-0640*. International Center on Diffraction Data: Newtown Square, PA.

116. Szekely, J.; Themelis, J. N., *Rate phenomena in process metallurgy*. Wiley: New York, 1971.

117. Wagner, C., *et. al.*, *Physicochemical Measurements In Metals Research*. Interscience Publishers: 1970; Vol. IV.